Karlsruher Institut für Technologie

Schriftenreihe
Kontinuumsmechanik im Maschinenbau

28

Benedikt Sterr

Machine learning aided multiscale mechanics of fiber suspensions

KIT Scientific Publishing

Benedikt Sterr

Machine learning aided multiscale mechanics of fiber suspensions

Schriftenreihe
Kontinuumsmechanik im Maschinenbau
Band 28

Karlsruher Institut für Technologie (KIT)
Institut für Technische Mechanik
Bereich Kontinuumsmechanik

Hrsg. Prof. Dr.-Ing. habil. Thomas Böhlke

Eine Übersicht aller bisher in dieser Schriftenreihe erschienenen Bände finden Sie am Ende des Buchs.

Machine learning aided multiscale mechanics of fiber suspensions

by
Benedikt Sterr

KIT Scientific Publishing

Karlsruher Institut für Technologie
Institut für Technische Mechanik
Bereich Kontinuumsmechanik

Machine learning aided multiscale mechanics of fiber suspensions

Zur Erlangung des akademischen Grades eines Doktor der Ingenieurwissenschaften von der KIT-Fakultät für Maschinenbau des Karlsruher Instituts für Technologie (KIT) genehmigte Dissertation

von Benedikt Sterr, M.Sc.

Tag der mündlichen Prüfung: 22. November 2024
Hauptreferent: Prof. Dr.-Ing. Thomas Böhlke
Korreferent: Prof. Dr. rer. nat. Matti Schneider
Korreferent: Prof. Dr. Andrew N. Hrymak

Impressum

KIT Scientific Publishing

Karlsruher Institut für Technologie (KIT)
KIT Scientific Publishing
Straße am Forum 2
D-76131 Karlsruhe

KIT Scientific Publishing is a registered trademark
of Karlsruhe Institute of Technology.
Reprint using the book cover is not allowed.

www.bibliothek.kit.edu/ksp.php | E-Mail: info@ksp.kit.edu | Shop: www.ksp.kit.edu

Print on Demand 2025 – Gedruckt auf FSC-zertifiziertem Papier

ISSN 2192-693X
ISBN 978-3-7315-1421-3
DOI 10.5445/KSP/1000179536

Publications and citation

This publication based thesis contains contents from the following publications, which are available under the CC BY 4.0 license[1]:

- Sterr, B. and Wicht, D. and Hrymak, A. and Schneider, M. and Böhlke, T., 2023.
  Homogenizing the viscosity of shear-thinning fiber suspensions with an FFT-based computational method.
  Journal of Non-Newtonian Fluid Mechanics 321, 105101
  https://doi.org/10.1016/j.jnnfm.2023.105101
- Sterr, B. and Hrymak, A. and Schneider, M. and Böhlke, T., 2024.
  Machine learning assisted discovery of effective viscous material laws for shear-thinning fiber suspensions.
  Computational Mechanics
  https://doi.org/10.1007/s00466-024-02490-4
- Sterr, B. and Gajek, S. and Hrymak, A. and Schneider, M. and Böhlke, T., 2024.
  Deep material networks for fiber suspensions with infinite material contrast.
  arXiv:2406.11662
  https://doi.org/10.48550/arXiv.2406.11662
  Accepted in *International Journal for Numerical Methods in Engineering* in February 2025

Whenever content from these publications is used, this is indicated by a footnote in the corresponding chapter or section heading. To specify the

[1] https://creativecommons.org/licenses/by/4.0/

manner in which the publication content is utilized, we define and use the clause *based on* as follows.

- Chapters or sections *based on* one or multiple publications include, but are not restricted to, selected content from the referenced publications. The sections from which the publication content was taken are given in the footnotes.
- Notation, spelling, and citation style of the publication content were homogenized throughout the thesis, and references to other chapters in this thesis were introduced.
- Repeating content was omitted and replaced with references to other sections of this thesis where appropriate.
- The numbering of equations, figures, and tables was adapted.

Additionally, the captions of figures and tables taken from the above publications are furnished with the clause *adapted from*. The formatting of figures and tables *adapted from* publications may have been changed and homogenized. The respective reference publication and the respective figure or table number are provided in the captions.

Another published article, which was *not* used in this thesis, is listed here according to the doctoral regulations for Mechanical Engineering (2017) §12 (1):

- Sterr, B. and Mahravan, E. and Kim, D., 2021.
  Uncertainty quantification of heat transfer in a microchannel heat sink with random surface roughness.
  International Journal of Heat and Mass Transfer 174, 121307.
  `https://doi.org/10.1016/j.ijheatmasstransfer.2021.121307`

Zusammenfassung

In Formungsprozessen von faserverstärkten Kunststoffbauteilen beeinflusst die Fasersuspensionsviskosität verschiedene Prozessparameter und physikalische Felder, die sich wiederum auf die Eigenschaften des fertigen Bauteils auswirken. Beispielsweise beeinflusst die Fasersuspensionsviskosität die Schneckendrehzahl beim Spritzgießen, die Presskraft beim Formpressen und allgemein das Strömungsfeld. Deshalb ist ein genaues Verständnis der Fasersuspensionsviskosität von entscheidender Bedeutung für die Modellierung von Fertigungsprozessen und die Vorhersagegenauigkeit von digitalen Prozessketten. Allerdings ist die experimentelle und analytische Untersuchung der Fasersuspensionsviskosität mit erheblichen Schwierigkeiten verbunden. Insbesondere ist es während rheologischer Experimente eine Herausforderung, einen bestimmten Orientierungszustand der Fasern zu gewährleisten. Außerdem erschweren die stark nichtlinearen Eigenschaften von Polymerschmelzen und die komplexe Geometrie der Suspensionsmikrostruktur analytische Bemühungen.

In dieser Arbeit werden rechnergestützte Homogenisierungsansätze mit maschinellem Lernen kombiniert, um das anisotrope, viskose Verhalten von Fasersuspensionen zu untersuchen und zu modellieren. Genauer gesagt werden Fast-Fourier-Transformation (FFT) basierte Methoden verwendet, um die effektive Spannungsantwort von Fasersuspensionen für ein bestimmtes Strömungsszenario zu berechnen. Anschließend wird maschinelles Lernen genutzt, um rechnerisch effiziente Ersatzmodelle für das Effektivverhalten der Suspensionen zu entwickeln. Aufgrund der industriellen Relevanz von faserverstärkten Polyamid

6 (PA6) Materialsystemen, sind die Untersuchungen in dieser Arbeit auf Fasersuspensionen mit scherverdünnendem PA6 Matrixmaterial fokussiert.

Eine bestehende FFT-basierte Methode für Suspensionen mit Newtonschen Lösungsmitteln wird auf Suspensionen mit nicht-Newtonschen Lösungsmitteln erweitert. Insbesondere wird die Legendre-Fenchel-Transformation genutzt, um eine duale Formulierung des zugehörigen Variationsproblems zu erhalten, das effizient mit FFTs und einem Newton-CG-Ansatz gelöst wird.

Die FFT-basierte Methode wird mit überwachtem, maschinellem Lernen kombiniert, um Modelle für das Effektivverhalten von Fasersuspensionen mit einem scherverdünnenden PA6 Matrixmaterial zu entwickeln. Dazu wird das anisotrope Scherverdünnungsverhalten von Fasersuspensionen für 109 verschiedene Faserorientierungszustände untersucht. Basierend auf den Ergebnissen der Untersuchungen werden vier Modellkandidaten für die effektive Viskosität formuliert und die Modellparameter mit überwachtem, maschinellem Lernen identifiziert.

Darüber hinaus wird eine neuartige Deep Material Network (DMN)-Architektur für die Behandlung von Fasersuspensionen mit unendlichem Materialkontrast vorgeschlagen. Insbesondere werden zweiphasige, geschichtete Emulsionen als DMN-Bausteine verwendet und deren geschlossene Homogenisierungsfunktionen hergeleitet. Um unendlichen Materialkontrast zu behandeln, werden zweiphasige, geschichtete Emulsionen auf spezielle Art und Weise wiederholt geschichtet. Unter Verwendung der abgeleiteten geschichteten Materialien wird das direct DMN Framework auf die Flexible DMN (FDMN) Architektur erweitert. Anschließend werden FDMNs zur Vorhersage des effektiven viskosen Verhaltens von Fasersuspensionen mit einem scherverdünnendem PA6 Matrixmaterial verwendet.

Summary

During the molding of Fiber Reinforced Polymer (FRP) components, the fiber suspension viscosity influences various process parameters and physical fields, which in turn impact the final part properties. For example, the suspension viscosity influences the screw speed in injection molding, the press force in compression molding, and generally the flow field. Therefore, an accurate understanding of the fiber suspension viscosity is essential for the modeling of manufacturing processes and the prediction accuracy of digital process chains. However, the experimental and analytical study of the fiber suspension viscosity is associated with significant challenges. In particular, it is challenging to ensure a specific fiber orientation state during rheology experiments. Additionally, the highly non-linear nature of polymer melts and the complex geometry of the fiber suspension microstructure complicate analytical efforts.

In this thesis, computational homogenization approaches are combined with machine learning techniques to study and model the anisotropic viscous behavior of fiber suspensions. More precisely, Fast Fourier Transform (FFT) based computational techniques are employed to compute the effective stress response of fiber suspensions for a given flow scenario. Subsequently, machine learning is used to build computationally efficient surrogate models for the effective suspension response. Because of the industrial relevance of fiber reinforced polyamide 6 (PA6) material systems, the investigations in this thesis are focused on fiber suspensions with a shear-thinning PA6 matrix material.

An existing FFT-based method for the homogenization of suspensions with Newtonian solvents is extended to suspensions with non-

Newtonian solvents. In particular, the Legendre–Fenchel transform is leveraged to obtain a dual formulation of the associated variational cell problem, which is solved efficiently using FFTs and a Newton-CG approach.

The FFT-based method is combined with supervised machine learning to develop Models for the effective behavior of fiber suspensions with a shear-thinning PA6 matrix material. To do so, the anisotropic shear-thinning behavior of fiber suspensions is studied for 109 different fiber orientation states. Based on the results of the investigations, four model candidates for the effective viscosity are formulated and the model parameters are identified with a supervised machine learning strategy.

Furthermore, a novel Deep Material Network (DMN) architecture for the treatment of suspensions of rigid fibers in non-Newtonian media is proposed. In particular, two-phase layered emulsions are utilized as DMN building blocks and their closed form homogenization functions are derived. To treat infinite material contrast, two-phase layered emulsions are repeatedly layered in a specific manner. The derived layered materials are used to extend the direct DMN framework to the Flexible DMN (FDMN) architecture. Finally, FDMNs are used to predict the effective viscous response of fiber suspensions with a shear-thinning PA6 matrix material.

Acknowledgments

I would like to sincerely and wholeheartedly thank my supervisors Thomas Böhlke, Matti Schneider, and Andrew Hrymak for their academic and personal guidance and support, which made this thesis possible in the first place. In particular, I would like to thank Thomas Böhlke for sparking my interest in continuum mechanics, for guiding me on my scientific journey through the field, and for the invaluable discussions we had on a wide range of topics. I would like to thank Matti Schneider for opening my eyes to various aspects of mathematical and scientific thinking that have been crucial to my scientific work, and that have strongly influenced my approach to solving both scientific and non-scientific problems. I would also like to thank Andrew Hrymak for providing his insight and expertise regarding polymer processing, which contributed greatly to this thesis. Also, thank you very much for enabling an excellent research stay at Western University, Ontario.

Furthermore, I would like to thank the whole staff at the ITM Chair for Continuum Mechanics for the great time we had together. I highly cherish the memories of our activities together and the experiences we shared, and I will greatly miss our discussions about research and various other topics. It has been a real pleasure to be surrounded by bright minded people who bring diverse and well-thought-out points of view to every discussion. Thank you very much for all the support you have provided, whether it be personal, organizational, or research related. I am also grateful to all the members of the IRTG 2078 for the exciting scientific discussions and pleasant times during the various IRTG activities and workshops. It has been a rare and valuable opportunity to

gain insight into many challenging research problems, which helped me gain a broader perspective on the topics surrounding my own research.

I would like to thank all members of my family and all my friends for lending an ear when needed, and for providing invaluable distractions and outside perspectives. Every moment of our time together has played a crucial role in the process of completing this thesis. In particular, I would like to thank Lukas, Florian, Timo, Alex, Moritz, and Jihoo for the great times we shared over the years and for being such supportive friends. Also, I would like to thank Martina and Klaus for their insightful advice, my grandmother for being unconditionally understanding and supportive, and Marius for always being positive and solution-oriented, regardless of the circumstances. All of you motivate me to make the best of every situation and to always keep moving forward.

Furthermore, I am sincerely grateful to Franziska for always being there for me. Your empathy has been a constant source of strength during challenging periods, and your lighthearted smile made cheerful times even more cheerful. Truly, thank you for being by my side through the ups and downs of life.

Also, I would like to express my deepest and most heartfelt gratitude to my parents. Thank you very much for your unwavering support, your kind words, and your endless patience not only during the course of this thesis, but throughout my life. You have enabled and encouraged me to follow my dreams and to think about life from a broader perspective. I truly thank you for everything.

The research documented in this thesis has been funded by the German Research Foundation (DFG) within the International Research Training Group "Integrated engineering of continuous-discontinuous long fiber-reinforced polymer structures" (GRK 2078). The support by the German Research Foundation (DFG) is gratefully acknowledged.

Karlsruhe, March 2025 Benedikt Sterr

Contents

Chapter 1

Introduction[1]

1.1 Motivation and goals

Especially because of their high specific stiffness, fiber reinforced composites are widely used for lightweight design, particularly in the transport and energy sectors (Swolfs, 2017; Wazeer et al., 2023). During the design process of fiber reinforced composite components, combinations of molding simulations and structural simulations are central to facilitate use case appropriate and material oriented design through digital twins (Botín-Sanabria et al., 2022) and virtual process chains (Henning et al., 2019; Görthofer et al., 2019; Meyer et al., 2023). In molding simulations of fiber reinforced composite parts, accurate prediction of the local fiber suspension viscosity is vital to correctly estimate process parameters (Castro and Tomlinson, 1990; Goodship, 2017) and other engineering quantities. In particular, the fiber orientation and the fiber volume distributions (Tseng et al., 2018), the flow fields, (Karl et al., 2021), as well as the final part properties (Mortazavian and Fatemi, 2015; Böhlke et al., 2019; Karl et al., 2021) depend on the suspension viscosity. However, in component scale simulations, it is computationally

[1] This chapter is based on the respective section 1 of the publications "Homogenizing the viscosity of shear-thinning fiber suspensions with an FFT-based computational method" (Sterr et al., 2023), "Machine learning assisted discovery of effective viscous material laws for shear-thinning fiber suspensions" (Sterr et al., 2024b), and "Deep material networks for fiber suspensions with infinite material contrast" (Sterr et al., 2024a)

infeasible to fully resolve the microstructure of the whole domain of interest to compute the suspension viscosity. For this purpose, analytical and computational homogenization methods are valuable tools to provide viscosity estimates for molding simulations. However, significant challenges arise for the holistic analytical modelling of the suspension viscosity, because the suspension viscosity depends on the local microstructure (Karl and Böhlke, 2022), the fiber volume fraction (Sepehr et al., 2004), and the fiber orientation state (Dinh and Armstrong, 1984). Additionally, the flow field (Cross, 1965; Sterr et al., 2023) and the melt temperature (Williams et al., 1955) influence the suspension viscosity as well. Furthermore, typical matrix materials in fiber suspensions show non-Newtonian behavior, which adds additional complexity to the derivation of appropriate models for the suspension viscosity.

In addition to the challenging analytical treatment, the investigation of fiber suspensions via rheological experiments is also difficult. Because of the transient effects during fiber suspension molding, including fiber breakage and change of orientation state, it is difficult to determine the suspension viscosity for a particular microstructure and load case (Binding, 1991; Schelleis et al., 2023). Furthermore, interaction of fibers with measurement devices (Eschbach, 1993) can affect the measured quantities.

Overall, the experimental and analytical study of the viscous behavior of fiber suspensions is accompanied by considerable difficulties. Thus, computational approaches are frequently leveraged to investigate the viscous behavior of suspensions. In the literature, a variety of computational techniques are employed for the study of suspensions, e.g., boundary element methods (Marin et al., 2012), finite element methods (Domurath et al., 2015; 2020; Traxl et al., 2020), lattice Boltzmann methods (Švec et al., 2012), and Fast-Fourier-Transform (FFT) based methods (Bertóti et al., 2021). In particular, FFT-based methods are established as highly efficient (Kabel et al., 2014; Wicht et al., 2020a;

Wicht, 2022) and do not require interface conforming meshes, which makes them widely applicable to complex synthetic or real microstructures (Schneider, 2021). So far, the study of fiber suspensions with FFT-based methods was restricted to suspensions with Newtonian matrix materials. Consequently, FFT-based methods could only be employed in data based modeling approaches for suspensions with *Newtonian* matrix materials. However, molding simulations of engineering components frequently require models for the viscous behavior of fiber suspensions with *non-Newtonian* matrix materials (Wittemann et al., 2019). This serves as our motivation for the development of FFT-based techniques to treat suspensions with non-Newtonian matrix materials, as well as the development of computationally efficient surrogate models based on the FFT-based computational data. Our approach to achieving these objectives is structured as follows:

- We seek to extend FFT-based methods for the homogenization of suspensions of rigid particles in a Newtonian matrix material to suspensions with non-Newtonian matrix materials. In particular, we consider non-Newtonian matrix materials whose stress response arises as the derivative of a dissipation potential density with respect to the strain rate tensor. We leverage the Legendre–Fenchel transformation to obtain a dual formulation of the associated non-linear homogenization problem (Bhattacharya and Suquet, 2005).
- We employ the developed FFT-based methods to study the effective viscous behavior of fiber suspensions with a polyamide 6 (PA6) matrix material. In particular, we investigate three dimensional representations of the effective suspension viscosity, as well as the degree of the material anisotropy and its dependence on the shear rate. For this purpose, we introduce a direction-dependent elongational viscosity based on concepts by Böhlke and Brüggemann (2001).
- Based on the data and understanding obtained with the FFT-based method, we derive models of the effective suspension viscosity for

use in component scale molding simulations. We present four closed form models with differing degrees of modeling complexity, and identify the model parameters using machine learning techniques. Moreover, we compare the accuracy of the models against the FFT-based simulation data for a variety of fiber orientation states.

- To leverage developments in the field of deep learning, we extend the Deep Material Network (DMN) architecture for the treatment of fibers suspensions with non-Newtonian matrix materials. To do so, we derive homogenization blocks that are capable of treating two-phase layered materials with incompressible fluid phases and infinite material contrast. Using the derived homogenization blocks, we present the novel Flexible DMN (FDMN) architecture and train FDMNs to predict the effective stress response of fiber suspensions with a shear-thinning PA6 matrix material. Finally, we compare the FDMN surrogate models with the closed form models presented in this thesis.

1.2 State of the art

1.2.1 Analytical modeling of the effective viscosity of fiber suspensions

Since work by Sutherland (1905) and Einstein (1905) on the effective scalar viscosity of dilute suspensions of spherical particles in Newtonian fluids, a variety of analytical approaches to model the complete tensorial viscosity of suspensions were suggested. For dilute and semidilute suspensions of slender rods in Newtonian fluids, models were proposed among others by Batchelor (1970; 1971), Dinh and Armstrong (1984), as well as Shaqfeh and Fredrickson (1990). For an overview of anisotropic mean-field homogenization models of particle suspensions in Newtonian fluids we refer the reader to Karl and Böhlke (2022). Various other

models are detailed by Petrie (1999).
Overall, finding analytical models for the effective viscosity of fiber suspensions is a challenging task, partly because of the locally inhomogeneous flow field inside the suspension, as well as the hydrodynamic interactions (Rahnama et al., 1995) and mechanical contacts (Sundararajakumar and Koch, 1997) between the fibers. Furthermore, the suspension viscosity also depends strongly on the local microstructure, i.e., the fiber geometry (Karl and Böhlke, 2022), the fiber volume fraction (Sepehr et al., 2004), and the fiber orientation state (Dinh and Armstrong, 1984). As far as external influences are concerned, the loading direction, the shear rate (Cross, 1965; Sterr et al., 2023), and the melt temperature (Williams et al., 1955) also affect the suspension viscosity. Especially for suspensions with non-Newtonian solvents and fiber concentrations beyond the semi-dilute regime, capturing the large variety of effects in a single analytical model is a difficult task. Depending on the fiber concentration of the suspension and the behavior of the matrix material, different homogenization approaches have been proposed. According to Pipes et al. (1994, §1) the fiber concentration regimes may be defined using the fiber volume fraction c_F and the fiber aspect ratio r_a as follows. The dilute regime is defined through $c_\mathsf{F} < (1/r_\mathsf{a})^2$, the semi-dilute regime through $(1/r_\mathsf{a})^2 < c_\mathsf{F} < 1/r_\mathsf{a}$, and the concentrated regime through $1/r_\mathsf{a} < c_\mathsf{F}$. Pipes et al. (1994, §1) define the hyperconcentrated regime for arrangements of fibers with aspect ratios $r_\mathsf{a} > 100$ through $\pi/16 < c_\mathsf{F} < \pi/4$ for square fiber arrays, and through $\pi/(8\sqrt{3}) < c_\mathsf{F} < \pi/(2\sqrt{3})$ for hexagonal fiber arrays. Based on the work by Batchelor (1970; 1971) on fiber suspensions with Newtonian matrix behavior, Goddard (1976a;b) proposed self-consistent analytical models of dilute and semi-dilute fiber suspensions with power-law shear-thinning matrix behavior. While the model predictions agree well with experimental results qualitatively, as found by Goddard (1978) and Mobuchon et al. (2005), quantitative accuracy can still be improved. Later, Souloumiac and Vincent (1998) incorporated fiber orientation

distributions into a self-consistent modeling approach for dilute, semi-dilute and concentrated fiber suspensions. However, in a comparison with experimental results in a convergent channel flow, the prediction accuracy of the model varies strongly with the shear rate and the fiber volume fraction. More recently, Férec et al. (2016) proposed semi-analytical and numerical self-consistent models for fiber suspensions with Ellis and Carreau-type matrix behavior. Even though the semi-analytical model was able to accurately replicate steady state solutions of a simple shear flow simulation, the models have yet to be successfully applied in other flow scenarios. Focusing on the concentrated and the hyperconcentrated regime, Pipes et al. (Pipes et al., 1991; Pipes, 1992; Coffin and Pipes, 1991; Pipes et al., 1994) developed models of collimated fiber suspensions, including uniformly distributed fiber misalignments with an orientation averaging (Ericksen, 1960; Tucker III, 1991) approach. The model predictions agree well with experimental results by Binding (1991), but the applicability of the model is restricted to collimated fiber arrays. To improve existing molding simulation solvers through small modifications, Favaloro et al. (2018) combined orientation averaging with a deformation mode and microstructure dependent informed isotropic viscosity, and successfully predicted the shell-core effect common in fiber suspension molding. However, the error of the model depends strongly on the applied deformation mode and approximated anisotropic viscosity. Thus, including recent developments (Tseng, 2021; Khan et al., 2023) it proves difficult to achieve high model prediction accuracy over the wide variety of application requirements in engineering systems.

1.2.2 Computational study of the viscous behavior of fiber suspensions

As discussed in the previous sections 1.1 and 1.2.1, the analytical and experimental study of the effective fiber suspension viscosity is associated

with various difficulties. Consequently, computational techniques can provide valuable insight into the viscous behavior of fiber suspensions that is difficult to obtain otherwise. As fiber suspension problems often involve Stokes flow, computational techniques focused on problems in the Stokes flow regime are of particular interest. Marin et al. (2012) introduced a highly accurate Boundary Element Method (BEM) to treat confined Stokes flow and succesfully applied it to a problem with a single sphere suspended in a Newtonian fluid. Subsequently, the BEM based approach used by Marin et al. (2012) could also be extended to different geometries and multiple suspended bodies. To treat complex particle geometries suspended in Newtonian fluids, Balboa Usabiaga et al. (2017) employed a method where particles are modeled via a rigid collection of connected spheres called "multiblob". Balboa Usabiaga et al. (2017) successfully applied their multiblob approach to Stokes flow problems near walls and in channels, involving multiblobs of different geometries such as spheres and cylinders. Furthermore, Fast Fourier Transform (FFT) based computational techniques, that were first popularized in solid mechanics (Moulinec and Suquet, 1994; 1998), were also successfully applied to Stokes flow problems involving Newtonian fluids. In combination with the RVE method (Kanit et al., 2003), the FFT-based computational approach was used to solve problems in porous media (Willot, 2015; Mezhoud et al., 2020; Tu et al., 2022), and to compute the effective viscosity of fiber suspensions with Newtonian matrix behavior (Bertóti et al., 2021). More details regarding FFT-based techniques can be found in recent review articles (Segurado et al., 2018; Schneider, 2021; Lucarini et al., 2021).

Computational methods were also employed to treat suspensions with non-Newtonian matrix fluids. Combining a mass tracking algorithm for the free surface representation, a lattice Boltzmann method for fluid flow, and an immersed boundary procedure for the interaction between fluid and rigid particles, Švec et al. (2012) studied slump tests of rigid fibers and rigid spherical particles suspended in a Bingham-type

fluid. They compared slump tests of the suspension with a slump test of the pure matrix material, and observed a smaller spread and an increased height in the test of the suspension material, which implies an increased effective yield stress in the suspension. Domurath et al. (2020) employed a Finite Element Method (FEM) based approach to study the transversely isotropic fluid equation by Ericksen (1960). They investigated the rheological coefficients and found that the model by Souloumiac and Vincent (1998) overpredicts the orientation dependence of a rheological coefficient. Extending work by Bertóti et al. (2021) on suspensions with Newtonian solvents, Sterr et al. (2023) used Fast Fourier Transform (FFT) based computational techniques (Schneider, 2021) and the RVE method (Kanit et al., 2003) to study the effective viscosity of fiber suspensions with non-Newtonian solvents. They investigated the effects of anisotropic shear-thinning on the effective suspension viscosity for varying fiber volume fractions, shear rates, and flow scenarios.

1.2.3 Data based surrogate models for the behvaior of particle suspensions

Accurate computational predictions of the microscopic behavior of a composite often require significant computational effort (Renard and Marmonier, 1987; Feyel, 2003; Spahn et al., 2014; Kochmann et al., 2016; Sorić et al., 2018), which motivates the use of fast data based surrogate models for component scale simulations (Gajek et al., 2021). Ashwin et al. (2022; 2024) trained a Multi-Layer-Perceptron, a Convolutional Neural Network, and a U-Net (Ronneberger et al., 2015) on particle resolved simulation data to predict fluid forces in dense ellipsoidal particle suspensions. They restricted to Newtonian matrix behavior and trained the networks on data for various Reynolds numbers and fiber volume fractions. Depending on the considered combination of Reynolds number and particle volume fraction, the prediction accuracy of the surrogate

models varies. Boodaghidizaji et al. (2022) use a multi-fidelity approach with neural networks and Gaussian processes to predict the steady state viscosity of fiber suspensions with a Newtonian solvent. To form the training data set, they combine low-fidelity estimates from constitutive equations with high-fidelity data obtained from numerically solving the involved partial differential equation system. The prediction accuracy of the multi-fidelity neural network and the multi-fidelity Gaussian process for simple shear flow depends strongly on the investigated parameters, especially the fiber volume fraction. Sterr et al. (2024b) derived four models for fiber suspensions with a Cross-type matrix fluid by combining FFT-based computational homogenization techniques with supervised machine learning. They investigated the anisotropic shear-thinning characteristics of the suspension viscosity for a variety of fiber orientation states via computational experiments, and formulated model candidates based on the observed phenomena. Using supervised machine learning techniques, they identified the model parameters from computational data, so that three of the four models were able to predict the fiber suspension viscosities to engineering accuracy for a wide range of engineering load cases. Generally, in addition to accurate estimation, extrapolation beyond the training data, as well as ensuring thermodynamical consistency prove challenging in the construction of surrogate models.

1.2.4 Deep material networks

In the context of solid materials without kinematic constraints, Liu et al. (Liu et al., 2019b; Liu and Wu, 2019) proposed Deep Material Networks (DMNs) as surrogate models for the full-field computational homogenization of microstructured materials. Their approach is based on nesting rotated laminates in an N-ary tree structure of N-phase laminates, and thus constructing a micromechanically motivated deep learning architecture. The volume fractions and rotations of the DMN

are then identified via supervised machine learning on linear elastic data. Remarkably, even if a DMN is trained on data obtained by solving linear homogenization problems, the predictions of the DMN for non-linear homogenization problems are impressively accurate. Gajek et al. (2020) further developed the DMN architecture into the rotation free direct DMN architecture. Direct DMNs feature a faster and more robust training process, as well as an efficient evaluation scheme for non-linear problems. Gajek et al. (2020) also showed that the thermodynamic consistency of the laminates is preserved in (direct) DMNs, such that the resulting DMN is thermodynamically consistent as well. Furthermore, Gajek et al. (2020) proved that non-linear homogenization is determined by linear homogenization to first order for two-phase materials. In a later article, Gajek et al. (2021) used direct DMNs to accelerate two-scale FE simulations of fiber reinforced composites by augmenting direct DMNs with the fiber orientation interpolation concept introduced by Köbler et al. (2018). Alternatively, DMN parameters may be interpolated with regard to microstructural parameters by a posteriori interpolation as proposed by Liu et al. (2019c) and Huang et al. (2022), or by augmenting DMNs with neural networks as proposed Li (2024). To leverage the capabilities of direct DMNs in concurrent thermomechanical two-scale simulations of composite components, Gajek et al. (2022) further extended the direct DMN architecture to incorporate thermomechanical coupling. Also in a thermomechanical setting, Shin et al. (2024) trained DMNs on linear thermoelastic data instead of linear elastic data, which improved the quality of fit for the effective thermal expansion properties, but only slightly affected the non-linear prediction quality of the DMNs. Additionally, they employed DMNs for uncertainty quantification, and for the inverse problem of optimizing a thermal boundary condition to achieve a desired thermo-elasto-viscoplastic response. By developing an inelastically-informed training strategy for DMNs, Dey et al. (2022) successfully predicted the creep behavior of fiber reinforced thermoplastics, which involves multiple scales in both

space and time. This enabled the inverse calibration of parameters for creep and plasticity constitutive equations by using DMNs as surrogates for otherwise costly FFT-based computations (Dey et al., 2023). Furthermore, Dey et al. (2024) leveraged DMNs in combination with fiber orientation interpolation (Köbler et al., 2018) to characterize the behavior of fiber reinforced thermoplastics including damage, plasticity, and creep. Overall, DMNs were extended and applied to treat a wide variety of problems, such as interface damage (Liu, 2020), the modeling of multiscale strain localization (Liu, 2021), problems involving woven materials (Wu et al., 2021) and porous materials (Nguyen and Noels, 2022a), as well as the architecture independent treatment of multi-phase composites (Nguyen and Noels, 2022b).

1.3 Outline and contributions of this thesis

- In **chapter 2**, we summarize the fundamentals of continuum mechanics which underpin the investigations presented in this thesis. Namely, we discuss kinematics and balance equations with a focus on incompressible flow. Additionally, we briefly discuss the description of fiber orientation states using fiber orientation tensors.
- In **chapter 3**, we present an FFT-based method for the computational homogenization of fiber suspensions with non-Newtonian matrix materials. Employing the presented FFT-based method, we investigate the anisotropic shear-thinning behavior of suspensions of rigid fibers in a shear-thinning PA6 matrix. More specifically, we study the non-linear effective behavior for a particular transversely isotropic fiber orientation state and multiple fiber volume fractions. We find that the anisotropic shear-thinning is more pronounced for higher fiber volume fractions, and that the degree of anisotropy decreases up to certain shear rates.

- In **chapter 4**, we extend the investigations of chapter 3 into the anisotropic shear-thinning of fiber suspensions with a PA6 matrix material to 109 different fiber orientation states. We introduce a non-linear anisotropy measure and find that the anisotropy of the effective viscosity and its shear rate dependence vary strongly with the fiber orientation state. Combining our results with insight from the literature, we formulate four model candidates for the effective viscous behavior of shear-thinning fiber suspensions. We employ a supervised machine learning strategy to learn the model parameters from the data obtained with the FFT-based computational approach presented in chapter 3. Finally, we assess the prediction accuracy of the models for all considered fiber orientation states and a broad range of engineering flow scenarios. Overall, three of the four presented models predict the effective suspension behavior to engineering accuracy, while one model does not compare favorably.
- In **chapter 5**, we present a novel DMN architecture for the treatment of rigid fibers suspended in incompressible non-Newtonian media. For this purpose, we derive closed form expressions for the linear homogenization functions of layered emulsions with finite material contrast. For the treatment of infinite material contrast, we rely on a particular type of layered material, the coated layered material. We derive necessary and sufficient conditions for which the effective behavior of a coated layered material with incompressible phases is non-singular, even if its core phase is rigid. Using the considered layered materials as homogenization blocks, we present the FDMN architecture as a nested tree of layered materials. We train FDMNs on linear homogenization data for fiber suspensions with a shear-thinning PA6 matrix material to predict the non-linear viscous behavior of the suspensions. Finally, we compare the prediction accuracy and applicability of the FDMNs with the closed form models presented in chapter 4.

- In **chapter 6** we present a summary of our most significant findings and conclude with some closing remarks.

1.4 Notation and frequently used operations

All abbreviations are defined when they first appear in each chapter. Likewise, for each quantity defined in this thesis, we provide a definition when the quantity first appears in each chapter. The definition might include properties such as the domain and codomain of a function, the superset of a set, the vector space a quantity lives in, or the tensorial order of a quantity. Additionally, we encode the tensor order of a quantity through the notation. We denote scalar quantities *and* quantities of variable order $r \in \mathbb{N}_{\geq 0}$ with non-bold letters or greek symbols, such as a, b or α, β, and provide the required information to completely define the quantity when it first occurs. Also, we denote the set of natural numbers including zero as $\mathbb{N}_{\geq 0}$, and the set of natural numbers not including zero as $\mathbb{N}_{>0}$. For first order tensors and tensor fields, we use bold lower-case letters, such as $\boldsymbol{a}$ or $\boldsymbol{b}$. For second order tensors and tensor fields we use bold upper-case letters, such as $\boldsymbol{A}$ or $\boldsymbol{B}$, and for fourth order tensors and tensor fields, we use blackboard bold upper-case letters, such as $\mathbb{A}$ or $\mathbb{B}$. For quantities of fixed order $r \notin \{0, 1, 2, 4\}$, we also use blackboard bold upper-case letters and additionally indicate the order by an index, e.g., $\mathbb{T}_8$ for an eighth order tensor. We denote the standard basis of d-dimensional euclidean space $\mathbb{R}^d$ with $\boldsymbol{e}_i$ for all dimensions $d \in \mathbb{N}_{>0}$, and follow the Einstein summation convention of summing over identical indices. Furthermore, we define the following frequently employed operations using tensor components given in the standard basis $\boldsymbol{e}_i$:

- The dot product of first order tensors and the Frobenius inner product denoted by $\cdot$, e.g., $\boldsymbol{a} \cdot \boldsymbol{b} = a_i b_i$ and $\boldsymbol{D} \cdot \boldsymbol{D} = D_{ij} D_{ij}$.

- The mapping of a first order tensor by a second order tensor $\boldsymbol{B}\boldsymbol{a} = B_{ij}a_j\,\boldsymbol{e}_i$.
- The mapping of a second order tensor by a fourth order tensor $\mathbb{C}[\boldsymbol{B}] = C_{ijkl}B_{kl}\,\boldsymbol{e}_i \otimes \boldsymbol{e}_j$.
- The composition of two second order tensors $\boldsymbol{A}\boldsymbol{B} = A_{ij}B_{jk}\,\boldsymbol{e}_i \otimes \boldsymbol{e}_k$
- The composition of two fourth tensors $\mathbb{A}\mathbb{C} = A_{ijkl}C_{klmn}\,\boldsymbol{e}_i \otimes \boldsymbol{e}_j \otimes \boldsymbol{e}_m \otimes \boldsymbol{e}_n$.

Furthermore, we denote the transposition of a quantity with $(\cdot)^\mathsf{T}$, the tensor product with $\otimes$, and the direct product with $\times$. The operator $(\cdot)^{\otimes a}$ constructs a tensor space of a-th order, e.g., $\mathbb{R}^{(\otimes 5)}$, and we define $(\mathbb{R}^d)^{\otimes 0} \equiv \mathbb{R}$ for all dimensions $d \in \mathbb{N}_{>0}$. Additionally, we define the tensor product of a scalar a with a first order tensor $\boldsymbol{v}$, such that $a \otimes \boldsymbol{v} \equiv av_i\boldsymbol{e}_i$. Finally, we denote vectors and matrices via underscores, e.g., $\underline{a}$ and $\underline{\underline{A}}$, respectively.

Chapter 2

Fundamentals

2.1 Introduction

This chapter serves as a brief summary of fundamental concepts in continuum mechanics that lay the basis for the investigations presented in this thesis. More specifically, we discuss kinematics and balance equations governing the behavior of continua with a focus on incompressible and isothermoal flow. Additionally, we discuss the mathematical description of fiber orientation states in fiber reinforced media, which serves as a central quantity for the study and generation of fibrous microstructures. For an extensive discussion of a wide range of aspects in continuum mechanics, we refer the reader to Šilhavý (1997), Haupt (2002), Liu (2002), Steinmann (2015), and Morro and Giorgi (2023).

2.2 Kinematics

For a d-dimensional material body occupying the volume $Y_0 \subset \mathbb{R}^d$, let $\boldsymbol{X} \in Y_0$ denote the reference placement of the material points of the body for $d \in \{2, 3\}$ (Steinmann, 2015). Then, the continuously differentiable and invertible function

$$\boldsymbol{\chi} : Y_0 \times [0, T] \to \mathbb{R}^d, \quad (\boldsymbol{X}, t) \mapsto \boldsymbol{\chi}(\boldsymbol{X}, t) \tag{2.1}$$

describes the motion of the body using the reference placement $\boldsymbol{X}$ and the time $t \in [0, T]$ (Steinmann, 2015). Here, the time t and the furthest considered point in time $T \in (0, \infty]$ live on the affinely extended real number line. The current placement $\boldsymbol{x}$ is then defined as

$$\boldsymbol{x} = \boldsymbol{\chi}(\boldsymbol{X}, t), \tag{2.2}$$

from which the current placement Y_t of the body follows as (Steinmann, 2015)

$$Y_\mathsf{t} = \{\boldsymbol{x} = \boldsymbol{\chi}(\boldsymbol{X}, t) \quad | \quad \boldsymbol{X} \in Y_0 \quad \text{and} \quad t \in [0, T]\}\,. \tag{2.3}$$

Consequently, a tensor field Λ of order $n \in \mathbb{N}_{\geq 0}$ on the material body can be described in terms of the reference placement Y_0 (Haupt, 2002), such that

$$\Lambda_\mathsf{L} : Y_0 \times [0, T] \to (\mathbb{R}^d)^{\otimes n}, \tag{2.4}$$

as well as in terms of the current placement Y_t, such that

$$\Lambda_\mathsf{E} : Y_\mathsf{t} \times [0, T] \to (\mathbb{R}^d)^{\otimes n}. \tag{2.5}$$

Here, the parameterizations Λ_L and Λ_E represent the Lagrangian and the Eulerian description of the tensor field Λ, respectively. Also, using the relations (Steinmann, 2015)

$$\Lambda_\mathsf{E}(\boldsymbol{x}, t) = \Lambda_\mathsf{L}(\boldsymbol{\chi}^{-1}(\boldsymbol{x}, t), t) \quad \text{and} \quad \Lambda_\mathsf{L}(\boldsymbol{X}, t) = \Lambda_\mathsf{E}(\boldsymbol{\chi}(\boldsymbol{X}, t), t), \tag{2.6}$$

one parameterization may be converted into the other. The temporal change of a tensor $\Lambda_\mathsf{L}(\boldsymbol{X}, t)$ parameterized by the reference placement $\boldsymbol{X}$ is defined through the material time derivative (Haupt, 2002)

$$\dot{\Lambda}_\mathsf{L}(\boldsymbol{X}, t) = \frac{\partial \Lambda_\mathsf{L}}{\partial t}(\boldsymbol{X}, t). \tag{2.7}$$

In terms of the current placement $\boldsymbol{x}$, the material time derivative of a tensor $\Lambda_{\mathsf{E}}(\boldsymbol{x}, t)$ is given by (Haupt, 2002)

$$\dot{\Lambda}_{\mathsf{E}}(\boldsymbol{x}, t) = \frac{\partial \Lambda_{\mathsf{E}}}{\partial t}(\boldsymbol{x}, t) + \frac{\partial \Lambda_{\mathsf{E}}}{\partial \boldsymbol{x}}(\boldsymbol{x}, t) \cdot \boldsymbol{v}_{\mathsf{E}}(\boldsymbol{x}, t), \tag{2.8}$$

where the Eulerian velocity $\boldsymbol{v}_{\mathsf{E}}(\boldsymbol{x}, t)$ is related to the Lagrangian velocity

$$\boldsymbol{v}_{\mathsf{L}}(\boldsymbol{X}, t) = \frac{\partial \boldsymbol{\chi}}{\partial t}(\boldsymbol{X}, t) \tag{2.9}$$

through equations (2.6). In the following, we omit the explicit declaration of Eulerian and Lagrangian quantities, and instead define the parameterization through the arguments of the discussed quantities. Eulerian quantities are defined through the argument $\boldsymbol{x}$ and Lagrangian quantities are defined through the argument $\boldsymbol{X}$. To capture local changes in the motion of the material body's points, we use the first spatial derivative of the motion $\boldsymbol{\chi}$, defined as the deformation gradient field $\boldsymbol{F}$ (Steinmann, 2015)

$$\boldsymbol{F} : Y_0 \times [0, T] \to (\mathbb{R}^d)^{\otimes 2}, \quad (\boldsymbol{X}, t) \mapsto \frac{\partial \boldsymbol{\chi}}{\partial \boldsymbol{X}}(\boldsymbol{X}, t). \tag{2.10}$$

Abusing notation and setting $\boldsymbol{F} = \boldsymbol{F}(\boldsymbol{X}, t)$, the relations (Steinmann, 2015)

$$\mathrm{d}\boldsymbol{x} = \boldsymbol{F}\,\mathrm{d}\boldsymbol{X}, \quad \mathrm{d}\boldsymbol{a} = \det(\boldsymbol{F})\boldsymbol{F}^{-\mathsf{T}}\,\mathrm{d}\boldsymbol{A}, \quad \text{and} \quad \mathrm{d}v = \det(\boldsymbol{F})\,\mathrm{d}V, \tag{2.11}$$

describe the mapping of the infinitesimal line $\mathrm{d}\boldsymbol{X}$, the infinitesimal area $\mathrm{d}\boldsymbol{A}$, and the infinitesimal volume $\mathrm{d}V$ from the reference placement Y_0 to the current placement Y_t. We may split a deformation gradient $\boldsymbol{F}(\boldsymbol{X}, t)$ into the symmetric positive definite tensors $\boldsymbol{U}(\boldsymbol{X}, t) \in \mathsf{Sym}^+(d)$ and $\boldsymbol{V}(\boldsymbol{X}, t) \in \mathsf{Sym}^+(d)$, as well as a proper orthogonal tensor $\boldsymbol{R}(\boldsymbol{X}, t) \in SO(d)$, such that (Steinmann, 2015)

$$\boldsymbol{F}(\boldsymbol{X}, t) = \boldsymbol{U}(\boldsymbol{X}, t)\boldsymbol{R}(\boldsymbol{X}, t) = \boldsymbol{R}(\boldsymbol{X}, t)\boldsymbol{V}(\boldsymbol{X}, t). \tag{2.12}$$

Here $\mathsf{Sym}^+(d)$ denotes the space of symmetric and positive definite second order tensors of dimension d, and $SO(d)$ stands for the special orthogonal group of dimension d (Steinmann, 2015). The left and right stretch tensors $\boldsymbol{U}(\boldsymbol{X},t)$ and $\boldsymbol{V}(\boldsymbol{X},t)$ encode the local stretch, and the tensor $\boldsymbol{R}(\boldsymbol{X},t)$ encodes the local rotation. For improved readability, we omit the dependence of the tensors $\boldsymbol{F},\boldsymbol{U},\boldsymbol{V}$, and $\boldsymbol{R}$ on space and time in the following. The deformation gradient $\boldsymbol{F}$ may be used to express the velocity gradient $\boldsymbol{L} \in (\mathbb{R}^d)^{\otimes 2}$ as (Haupt, 2002)

$$\boldsymbol{L} = \frac{\partial \boldsymbol{v}(\boldsymbol{x},t)}{\partial \boldsymbol{x}} = \dot{\boldsymbol{F}}\boldsymbol{F}^{-1}, \tag{2.13}$$

which may be decomposed into the symmetric part $\boldsymbol{D} = (\boldsymbol{L} + \boldsymbol{L}^{\mathsf{T}})/2$ and the skew-symmetric part $\boldsymbol{W} = (\boldsymbol{L} - \boldsymbol{L}^{\mathsf{T}})/2$, such that

$$\boldsymbol{L} = \boldsymbol{D} + \boldsymbol{W}, \quad \text{and} \quad \boldsymbol{D} \cdot \boldsymbol{W} = 0. \tag{2.14}$$

The strain rate tensor $\boldsymbol{D}$ encodes the rate of shearing and stretching, and the spin tensor $\boldsymbol{W}$ encodes the rate of rotation.

2.3 Balance equations

2.3.1 General balance equation

Balance equations encode physical laws that govern processes of interest in engineering and science. In this thesis, we treat purely mechanical systems, i.e., thermal effects are not considered. For a discussion of the balance equations of energy and entropy, as well as a comprehensive description of the thermodynamics of continuous media, we refer to Krawietz (2013). In the following, we consider an arbitrary bounded volume Ω_t with boundary $\partial\Omega$ and discuss general forms of a balance equation, as well as the special cases of the balance of mass and the

balance of linear momentum over the considered volume Ω_t. The general balance equation of an n-th order tensor field $\psi : Y_t \times [0,T] \to (\mathbb{R}^d)^{\otimes n}$ over the volume Ω_t reads (Liu, 2002)

$$\frac{\mathrm{d}}{\mathrm{d}t}\int_{\Omega_t} \psi \,\mathrm{d}\Omega_t(\boldsymbol{x}) = \int_{\Omega_t} p_\psi + s_\psi \,\mathrm{d}\Omega_t(\boldsymbol{x}) + \int_{\partial\Omega_t} \boldsymbol{q}_\psi \odot \boldsymbol{n} \,\mathrm{d}A_t(\boldsymbol{x}), \quad (2.15)$$

where $\odot$ denotes a single order tensor contraction. The three tensor fields $p_\psi : \Omega_t \times [0,T] \to (\mathbb{R}^d)^{\otimes n}$, $s_\psi : \Omega_t \times [0,T] \to (\mathbb{R}^d)^{\otimes n}$, and $\boldsymbol{q} : \Omega_t \times [0,T] \to (\mathbb{R}^d)^{\otimes (n+1)}$ represent the internal production field, the external supply field, and the non-convective flux field of the quantity ψ, respectively. Using the Reynolds transport theorem and the divergence theorem (Bertram, 2012), the local formulation of the general balance equation (2.15) in regular points (Liu, 2002)

$$\frac{\partial \psi}{\partial t} + \operatorname{div}(\psi \otimes \boldsymbol{v}) = p_\psi + s_\psi + \operatorname{div}\left(\boldsymbol{q}_\psi\right), \quad (2.16)$$

follows from equation (2.15). Here, $\boldsymbol{v} : \Omega_t \times [0,T] \to \mathbb{R}^d$ denotes the velocity field. If the volume Ω_t contains a material singular surface $\mathcal{S}_t$, the jump condition for points $\boldsymbol{x} \in \mathcal{S}_t$ on the material singular surface $\mathcal{S}_t$ (Morro and Giorgi, 2023)

$$[\![\boldsymbol{q}_\psi]\!] \cdot \boldsymbol{n} = \boldsymbol{0} \quad (2.17)$$

holds. Here, the jump $[\![q]\!]$ of a quantity q across a material singular surface $\mathcal{S}_t$ with normal vector $\boldsymbol{n}$ is

$$[\![q]\!] = q^+ - q^-, \quad (2.18)$$

where we denote the left- and right hand side limits of the quantity q with q^+ and q^-, respectively.

2.3.2 Balance of mass

We consider the mass density $\rho : \Omega_t \times [0, T] \to \mathbb{R}$ as the subject ψ of the balance equation (2.16). Because the internal production p_ρ, the external supply s_ρ, and the non-convective flux $\boldsymbol{q}_\rho$ vanish (Morro and Giorgi, 2023), the local form of the balance of mass for regular points reads

$$\dot{\rho} + \rho \operatorname{div}(\boldsymbol{v}) = 0. \tag{2.19}$$

Because we require the jump condition (2.17) to be satisfied, the balance of mass is satisfied for singular points $\boldsymbol{x} \in \mathcal{S}_t$. For incompressible flow, the material derivative $\dot{\rho}$ of the mass density ρ vanishes and the balance of mass simplifies to (Landau and Lifshitz, 2013)

$$\operatorname{div}(\boldsymbol{v}) = 0. \tag{2.20}$$

In particular, incompressible flow may arise from the movement of an incompressible material with spatially and temporally *homogeneous* mass density ρ. However, compressible materials with spatially and temporally *inhomogeneous* mass density ρ may also undergo incompressible flow, because the material time derivative

$$\dot{\rho} = \frac{\partial \rho}{\partial t} + \frac{\partial \rho}{\partial \boldsymbol{x}} \cdot \boldsymbol{v} \tag{2.21}$$

should vanish, not only the individual summands $\partial\rho/\partial t$ and $(\partial\rho/\partial\boldsymbol{x}) \cdot \boldsymbol{v}$ (Spurk and Aksel, 2007).

2.3.3 Balance of linear and angular momentum

Considering the linear momentum density $\rho\boldsymbol{v}$ as the subject ψ of the balance equation (2.16), the local balance of the linear momentum den-

sity $\rho \boldsymbol{v}$ for regular points reads (Morro and Giorgi, 2023)

$$\rho \dot{\boldsymbol{v}} = \operatorname{div}(\boldsymbol{\sigma}) + \boldsymbol{b}, \tag{2.22}$$

where $\boldsymbol{\sigma} : \Omega_t \times [0,T] \to \mathsf{Sym}(d)$ denotes the Cauchy stress tensor field, $\mathsf{Sym}(d)$ stands for the space of symmetric second order tensors of dimension d, and $\boldsymbol{b} : \Omega_t \times [0,T] \to \mathbb{R}^d$ is the volume force density field. The traction field

$$\boldsymbol{t} = \boldsymbol{\sigma} \boldsymbol{n} \tag{2.23}$$

is continuous on the material singular surface $\mathcal{S}_t$ by virtue of the jump condition (2.17), because it holds that

$$[\![\boldsymbol{\sigma}]\!] \boldsymbol{n} = 0 \quad \iff \quad \boldsymbol{\sigma}^+ \boldsymbol{n} = \boldsymbol{\sigma}^- \boldsymbol{n}. \tag{2.24}$$

In this thesis we consider stationary processes without volume force densities, hence the supply term $\boldsymbol{b}$ and the material derivative $\dot{\boldsymbol{v}}$ of the velocity vanish, and the balance of linear momentum simplifies to

$$\operatorname{div}(\boldsymbol{\sigma}) = 0. \tag{2.25}$$

To separate spherical and deviatoric contributions to the stress field $\boldsymbol{\sigma}$, we introduce the additive split

$$\boldsymbol{\sigma} = \boldsymbol{\tau} - p\boldsymbol{I}, \tag{2.26}$$

into the viscous stress field $\boldsymbol{\tau} : \Omega_t \times [0,T] \to \mathsf{Sym}_0(d)$ and the pressure field $p : \Omega_t \times [0,T] \to \mathbb{R}$. Here, $\boldsymbol{I}$ denotes the second order unit tensor and $\mathsf{Sym}_0(d)$ denotes the space of traceless symmetric second order tensors of dimension d. Thus, inserting the additive split (2.26) into the balance of linear momentum (2.25) yields

$$\operatorname{div}(\boldsymbol{\tau}) = \nabla p. \tag{2.27}$$

Furthermore, for a reference point $\boldsymbol{x}_0 \in \Omega_t$, we consider the angular momentum density $(\boldsymbol{x} - \boldsymbol{x}_0) \times \rho \boldsymbol{v}$ as the subject ψ of the balance equation (2.16). Then, the balance of angular momentum reduces to (Liu, 2002)

$$\boldsymbol{\sigma} = \boldsymbol{\sigma}^{\mathsf{T}}, \tag{2.28}$$

if the balance of linear momentum (2.22) is satisfied. Thus, the symmetry of the Cauchy stress tensor guarantees the conservation of angular momentum for non-polar materials, i.e., for the case that no momentum densities act on the volume Ω_t.

2.4 Description of fiber orientation states[1]

Since the effective behavior of a fiber suspension depends on the fiber orientation statistics in the suspension, a mathematical description of the orientation state is essential to the study of fiber suspensions. In the following, we use a fiber orientation distribution function (Kanatani, 1984)

$$\rho : S^2 \to \mathbb{R}, \quad \boldsymbol{n} \mapsto \rho(\boldsymbol{n}), \tag{2.29}$$

to encode the probability that fibers are oriented in direction $\boldsymbol{n}$ on the 2-sphere S^2, and thus describe the orientation state of a fiber suspension. The temporal and spatial evolution of the orientation distribution function ρ is governed by a partial differential equation, the Fokker–Planck equation (Fokker, 1914). However, in component scale molding simulations, computing the evolution of the orientation distribution function ρ using the Fokker-Planck equation requires huge computational effort. Instead, it is common (Kennedy and Zheng, 2013) to use the second order fiber orientation tensor (Kanatani, 1984; Advani and Tucker III,

[1] This section is based on the section 2.1 of the publication "Machine learning assisted discovery of effective viscous material laws for shear-thinning fiber suspensions" Sterr et al. (2024b).

1987)

$$\boldsymbol{N} = \int_{S^2} \boldsymbol{n} \otimes \boldsymbol{n}\, \rho(\boldsymbol{n})\, \mathrm{d}S(\boldsymbol{n}), \tag{2.30}$$

as a measure for the fiber orientation state. The tensor $\boldsymbol{N}$ is symmetric, positive semi-definite, and has unit trace, such that

$$N_{ii} = \lambda_1 + \lambda_2 + \lambda_3 = 1, \tag{2.31}$$

where λ_1, λ_2, and λ_3 denote the eigenvalues of the tensor $\boldsymbol{N}$. By sorting the eigenvalues

$$\lambda_1 \geq \lambda_2 \geq \lambda_3, \tag{2.32}$$

and considering equation (2.31), the bounds for the largest eigenvalue λ_1 are found as

$$1 \geq \lambda_1 \geq \frac{1}{3}. \tag{2.33}$$

Additionally, an upper bound for the eigenvalue λ_2 follows from positive semi-definiteness of the tensor $\boldsymbol{N}$, and a lower bound may be derived by eliminating λ_3 from equation (2.32) using equation (2.31), such that

$$\min\left(\lambda_1, 1-\lambda_1\right) \geq \lambda_2 \geq \frac{1-\lambda_1}{2}. \tag{2.34}$$

Thus, we may parametrize the tensor $\boldsymbol{N}$ by its two eigenvalues λ_1 and λ_2, and the rotation $\boldsymbol{Q}$ in terms of an eigendecomposition

$$\boldsymbol{N} = \boldsymbol{Q}\, \mathbf{diag}(\lambda_1, \lambda_2, \lambda_3)\, \boldsymbol{Q}^{\mathsf{T}}, \tag{2.35}$$

where the **diag** operator constructs a second order tensor in the standard basis of $\mathbb{R}^3$. By objectivity, the results of this thesis generalize to all rotations $\boldsymbol{Q}$, and for simplicity we choose

$$\boldsymbol{Q} = \boldsymbol{I}. \tag{2.36}$$

Consequently, any second order fiber orientation tensor $\boldsymbol{N}$ may be encoded by a vector $\underline{\lambda} = (\lambda_1, \lambda_2)^{\mathsf{T}}$, and represents a point in the fiber orientation triangle S_{T} defined through equations (2.33) and (2.34), such that

$$S_{\mathsf{T}} = \left\{ \underline{\lambda} = (\lambda_1, \lambda_2)^{\mathsf{T}} \;\middle|\; 1 \geq \lambda_1 \geq \frac{1}{3} \quad \text{and} \right. \\ \left. \min\left(\lambda_1, 1 - \lambda_1\right) \geq \lambda_2 \geq \frac{1 - \lambda_1}{2} \right\}. \tag{2.37}$$

For an in-depth discussion on the description of fiber orientation states, we refer the reader to Kanatani (1984), Bauer and Böhlke (2022), and Bauer et al. (2023).

Chapter 3

Homogenizing the viscosity of shear-thinning fiber suspensions with an FFT-based computational method[1]

3.1 Introduction

Even though the suspension viscosity is a quantity of direct engineering interest, it is difficult to determine the full viscosity tensor by experimental methods. This is partly because it is challenging to ensure a specific fiber orientation state during rheology experiments (Binding, 1991), and the suspension viscosity depends strongly on the fiber orientation(Poslinski et al., 1988). Furthermore, fibers break during rheometer studies, which also affects the suspension viscosity (Binding, 1991). Last but not least, the dependence of the suspension viscosity on shear rate and temperature (Krishnan et al., 2010) further complicates matters. As a result, tensorial and scalar analytical homogenization methods are commonly used in conjunction with scalar experiments to understand and predict the local suspension viscosity.

[1] This chapter is based on the sections 1 to 5 of the publication "Homogenizing the viscosity of shear-thinning fiber suspensions with an FFT-based computational method" (Sterr et al., 2023).

In the case of suspensions with non-Newtonian matrix behavior, multiple models (Leal, 1975; Kaloni and Stastna, 1983; Brunn, 1977; 1980) were developed based on second order fluid theory. However, these models are restricted to a single suspended particle. Brunn (1980) also applied his single particle model to dilute suspensions and found that the model could not capture hydrodynamic particle-particle interactions. In a shear-thinning power law setting, Goddard (1976b;a) developed a model for dilute suspensions, which was found to be qualitatively promising but quantitatively inaccurate by himself (Goddard, 1978) and Mobuchon et al. (2005). Later, Pipes et al. (1991; 1994) proposed a model for the concentrated and hyperconcentrated regime in a power law setting. Even though the results agree well with experimental data by Binding (1991), the model is limited by its assumption of unidirectional and fixed fiber arrays. The prediction accuracy of another power-law model by Souloumiac and Vincent (1998) varies strongly with the shear rate and fiber volume fraction, making it difficult to apply appropriately. Also, more recent models (Férec et al., 2016; Tseng, 2021; Férec et al., 2017; Favaloro et al., 2018) have yet to be established as valid over a wide range of temperatures, shear rates, fiber-orientation states and fiber aspect ratios. Overall, holistic theoretical treatment of all physical effects in fiber suspensions proves to be a difficult task.

Consequently, computational methods were also employed to treat suspensions with non-Newtonian matrix fluids. Domurath et al. (2015) used the Finite Element Method (FEM) to study the effective viscosity of a dilute suspension with a single spherical particle suspended in a Bird-Carreau fluid. For non-dilute suspensions, Traxl et al. (2020) used a FEM-based approach to investigate the effective viscosity of suspensions with noncolloidal angular, as well as spherical pores and particles in generalized-Newtonian fluids. The investigations of Traxl et al. (2020) consider suspensions with spherical, hexahedral, and tetrahedral particles, as well as matrix fluids with Newtonian, Power-law,

Cross-type, and von Mises-type behavior. Švec et al. (2012) studied rheological properties of suspensions with rigid spherical particles and fibers suspended in Newtonian and non-Newtonian matrix fluids. To do so, Švec et al. (2012) used a computational framework combining the lattice Boltzmann method for fluid flow, a mass tracking algorithm for free surface representation, and an immersed boundary approach to consider interactions between the fluid and the particles.

In this chapter, with regard to the difficult experimental and theoretical treatment of fiber suspensions with non-Newtonian matrix behavior, we apply FFT-based computational methods to study the viscosity of such suspensions. Using FFT-based computational methods allows us to leverage highly efficient implementations of the FFT, powerful non-linear equation solvers, and discretizations with regular grids. This enables the study of fiber suspensions with microstructures that are otherwise difficult to discretize and investigate using interface-conforming mesh based approaches. Thus, we extend the approach for suspensions with Newtonian matrix behavior detailed by Bertóti et al. (2021) to suspensions with non-Newtonian, Cross-type (Cross, 1965; 1970) shear-thinning fluids. In section 3.2, we approach the effective suspension viscosity from a theoretical and a computational perspective, and make use of an interpolation based matrix equation to estimate the anisotropic, non-Newtonian suspension viscosity from a limited number of computational experiments. As the physical basis for our investigations, we use a Cross-type material law to model the viscosity behavior of a commercially available PA6, and study suspension microstructures with fibers of aspect ratio ten. In preliminary investigations to identify the resolution of the discretized suspension microstructure, we find that the resolution error of the effective stresses can depend favorably on the shear rate, see section 3.3.2. Through a volume element size study, we find that the necessary volume element size for engineering considerations are highly similar in a specific Newtonian case and the investigated non-Newtonian

case, see section 3.3.3. As our main contribution, we visualize and discuss in section 3.4 how the shear rate and fiber volume fraction influence the magnitude and degree of anisotropy of the suspension viscosity. We observe that the viscosity magnitude decreases with the shear rate until a Cross-type model intrinsic, minimum viscosity is reached. In contrast, the degree of anisotropy depends on the degree to which the matrix behaves nonlinearly. Additionally, we find that the dependence of both the magnitude and the degree of anisotropy on the shear rate is increased for higher fiber volume fractions. In a comparison between an analytical mean-field model and our computational results, we observe large discrepancies in the predicted viscosities.

3.2 Computing the effective viscosity of particles suspended in a non-linear viscous medium

3.2.1 The non-linear viscosity tensor

For an incompressible Newtonian fluid, the strain rate tensor $\boldsymbol{D} \in \mathsf{Sym}_0(3)$ and the non-equilibrium viscous stress tensor $\boldsymbol{\tau} \in \mathsf{Sym}_0(3)$ are related by the constitutive law

$$\boldsymbol{\tau} = 2\eta \boldsymbol{D}, \tag{3.1}$$

involving a shear viscosity η. Here, $\mathsf{Sym}_0(3)$ denotes the vector space of symmetric and traceless second-order tensors. More generally, non-Newtonian models (Krishnan et al., 2010) may be considered where the viscosity depends on the scalar shear rate $\dot{\gamma} = \sqrt{2}\,\|\boldsymbol{D}\|$ with the norm $\|\boldsymbol{D}\| = \sqrt{\boldsymbol{D} \cdot \boldsymbol{D}}$.
Cross-type (Cross, 1965; 1970) material models are able to predict the shear-thinning rheology of polymers accurately (Krishnan et al., 2010).

Their viscosity is governed by an expression of the form

$$\eta(\dot{\gamma}) = \eta_\infty + \frac{\eta_0 - \eta_\infty}{1 + (k\dot{\gamma})^m}, \tag{3.2}$$

with positive material parameters $\eta_0 \geq \eta_\infty$, k, and m.
For the shear rate limits $\dot{\gamma} \to 0$ and $\dot{\gamma} \to \infty$, the scalar viscosity $\eta(\dot{\gamma})$ approaches the initial viscosity η_0 and the asymptotic viscosity η_∞, respectively. The two material parameters k and m control the transition region between the viscosities η_0 and η_∞.
To describe suspensions of non-spherical particles, it is convenient to consider more general, anisotropic viscosity tensors $\mathbb{V} \in L(\mathsf{Sym}_0(3))$ and constitutive relations of the form (Ericksen, 1959; 1960)

$$\boldsymbol{\tau} = \mathbb{V}[\boldsymbol{D}], \tag{3.3}$$

where L refers to the linear transformations on a given vector space, and the viscosity tensor $\mathbb{V}$ depends on the fiber arrangement and the fiber orientation distribution. If the suspending fluid is itself non-Newtonian, the suspension will, in general, be governed by a constitutive relation of the form

$$\boldsymbol{\tau} = \mathbb{V}(\boldsymbol{D})[\boldsymbol{D}] \tag{3.4}$$

with a viscosity tensor $\mathbb{V}$ that additionally depends on the shear-rate tensor $\boldsymbol{D}$. By the dissipation inequality, the viscosity tensor $\mathbb{V}(\boldsymbol{D})$ must be positive semi-definite for all shear rates $\boldsymbol{D}$, while the major symmetry of the viscosity tensor $\mathbb{V}(\boldsymbol{D})$ is required in the linear case for Onsager's relations to be satisfied (Šilhavý, 1997). Existence of a dissipation potential is sufficient for the major symmetry of the viscosity tensor $\mathbb{V}(\boldsymbol{D})$ in the non-linear case, see Šilhavý (1997, Sec. 12.3.1). For the general formulation of a dissipation potential with temperature and mass density dependence, also see Šilhavý (1997, Sec. 12.3.1).
For the subsequent derivations, we will look at a special case that is

sufficient for our purposes. Assume that for constant temperature and density a twice continuously differentiable dissipation potential density $\Psi : \mathsf{Sym}_0(3) \to \mathbb{R}$ is given, which furthermore satisfies the condition

$$\frac{\partial \Psi}{\partial \boldsymbol{D}}(\mathbf{0}) = \mathbf{0}. \tag{3.5}$$

Then, the non-equilibrium viscous stress $\boldsymbol{\tau}$ is governed by the relationship

$$\boldsymbol{\tau} = \frac{\partial \Psi}{\partial \boldsymbol{D}}(\boldsymbol{D}), \tag{3.6}$$

and by the fundamental theorem of calculus, we may write

$$\frac{\partial \Psi}{\partial \boldsymbol{D}}(\boldsymbol{D}) = \int_0^1 \frac{\mathrm{d}}{\mathrm{d}s}\left[\frac{\partial \Psi}{\partial \boldsymbol{D}}(s\boldsymbol{D})\right] \mathrm{d}s = \int_0^1 \frac{\partial^2 \Psi}{\partial \boldsymbol{D}^2}(s\boldsymbol{D})\,\mathrm{d}s\,[\boldsymbol{D}] \equiv \mathbb{V}(\boldsymbol{D})[\boldsymbol{D}]. \tag{3.7}$$

Thus, the viscosity tensor

$$\mathbb{V}(\boldsymbol{D}) \equiv \int_0^1 \frac{\partial^2 \Psi}{\partial \boldsymbol{D}^2}(s\boldsymbol{D})\,\mathrm{d}s \tag{3.8}$$

has major symmetries, as a consequence of Schwarz' theorem on the commutativity of the second partial derivatives of a twice continuously differentiable function. Thus, for any given dissipation potential density, the associated viscosity tensor (3.8) automatically has the major symmetry. For compactness, we will refer to *dissipation potential densities* as *dissipation potentials* throughout this thesis. It is not difficult to construct dissipation potentials both for the Newtonian (3.1) and the Cross model (3.2), i.e.,

$$\Psi(\boldsymbol{D}) = \left(\eta_\infty + (\eta_0 - \eta_\infty)\,{}_2F_1\left(1, \frac{2}{m}, \frac{2+m}{m}, -(k\dot{\gamma})^m\right)\right)\frac{\dot{\gamma}^2}{2} \tag{3.9}$$

involving the hypergeometric function ${}_2F_1$. In the Newtonian case, it holds that $\eta = \eta_0 = \eta_\infty$, and thus

$$\Psi(\boldsymbol{D}) = \eta\, \boldsymbol{D} \cdot \boldsymbol{D} \tag{3.10}$$

The advantage of using the representation by a dissipation potential is that this potential form is preserved under a change of scales, i.e., by homogenization (Suquet, 1985; 1987). Subsequently, the viscosity tensor is accessible via a postprocessing step, see equation (3.8).
Actually, due to the presence of infinitely viscous inclusions, it is more convenient to work with the complementary potential Φ which arises as the Legendre-Fenchel dual

$$\Phi(\boldsymbol{\tau}) := \sup \left\{ \boldsymbol{\tau} \cdot \boldsymbol{D} - \Psi(\boldsymbol{D}) \,|\, \boldsymbol{D} \in \mathsf{Sym}_0(3) \right\} \tag{3.11}$$

of the dissipation potential Ψ. The potential Ψ must grow superlinearly and be non-negative for Φ to be a proper function, i.e., not infinite everywhere. Then, as a consequence of the Fenchel-Moreau identity (Chambolle and Pock, 2016, Eq. (3.8)), the constitutive law (3.6) may be written in dual form

$$\boldsymbol{D} = \frac{\partial \Phi}{\partial \boldsymbol{\tau}}(\boldsymbol{\tau}). \tag{3.12}$$

From this, similar to the viscosity $\mathbb{V}$, the fluidity tensor $\mathbb{F}$ follows as

$$\mathbb{F}(\boldsymbol{\tau}) \equiv \int_0^1 \frac{\partial^2 \Phi}{\partial \boldsymbol{\tau}^2}(s\boldsymbol{\tau})\, \mathrm{d}s. \tag{3.13}$$

In the Newtonian case, the viscosity $\mathbb{V}$ and the fluidity $\mathbb{F}$ constitute the kinetic coefficients (Šilhavý, 1997). In addition to the presented context, the aforementioned potential framework can also be applied in the context of the rigid-viscoplastic modeling of polycrystals. See, e.g., Böhlke and Bertram (2003) and Böhlke (2004), where the viscoplastic behavior of single crystals and polycrystals is modeled via a non-linear viscous approach.

3.2.2 Scale transition in non-linear viscosity

Locally, the balance of linear momentum

$$\operatorname{div}(\boldsymbol{\tau}) - \nabla p = \mathbf{0} \tag{3.14}$$

results from a split of the stress $\boldsymbol{\sigma}$ inside the material into an unknown, periodic pressure field $p : Y \to \mathbb{R}$ and the local viscous stress field

$$\boldsymbol{\tau} = \mathcal{T}(\cdot, \bar{\boldsymbol{D}} + \nabla^{\mathsf{s}}\boldsymbol{v}), \tag{3.15}$$

and needs to be satisfied. Here, the pressure p acts as a reaction stress due to incompressibility. We consider a rectangular volume $Y \subseteq \mathbb{R}^3$, and suppose that a heterogeneous dissipation potential $\Psi : Y \times \mathsf{Sym}_0(3) \to \mathbb{R}$ is given which satisfies the conditions discussed in the previous section pointwise. The associated stress operator reads

$$\mathcal{T} : Y \times \mathsf{Sym}_0(3) \to \mathsf{Sym}_0(3), \tag{3.16}$$

$$(\boldsymbol{x}, \boldsymbol{D}) \mapsto \frac{\partial \Psi}{\partial \boldsymbol{D}}(\boldsymbol{x}, \boldsymbol{D}). \tag{3.17}$$

The *effective* dissipation potential is defined as

$$\bar{\Psi}(\bar{\boldsymbol{D}}) = \inf \left\langle \Psi(\cdot, \bar{\boldsymbol{D}} + \nabla^{\mathsf{s}}\boldsymbol{v}) \right\rangle_Y \quad \text{for} \quad \bar{\boldsymbol{D}} \in \mathsf{Sym}_0(3), \tag{3.18}$$

where the infimum is taken over all periodic velocity fields $\boldsymbol{v} : Y \to \mathbb{R}^3$ with vanishing divergence and the operator $\langle\cdot\rangle_Y$ denotes the spatial average

$$\langle\cdot\rangle_Y \equiv \frac{1}{|Y|} \int_Y (\cdot)\, \mathrm{d}Y(\boldsymbol{x}) \quad \text{with} \quad |Y| \equiv \int_Y \mathrm{d}Y(\boldsymbol{x}). \tag{3.19}$$

The effective shear stress $\bar{\boldsymbol{\tau}} \in \mathsf{Sym}_0(3)$ then arises from the relationship

$$\bar{\boldsymbol{\tau}}(\bar{\boldsymbol{D}}) = \frac{\partial \bar{\Psi}}{\partial \bar{\boldsymbol{D}}}(\bar{\boldsymbol{D}}), \tag{3.20}$$

which is similar to equation (3.6). Equivalently, the effective stress may be computed by averaging the local shear stress

$$\bar{\boldsymbol{\tau}}(\bar{\boldsymbol{D}}) = \left\langle \mathcal{T}(\cdot, \bar{\boldsymbol{D}} + \nabla^{\mathsf{s}} \boldsymbol{v}) \right\rangle_Y, \tag{3.21}$$

where the periodic velocity field $\boldsymbol{v}$ solves the Euler-Lagrange equation of the variational problem (3.18)

$$\operatorname{div}(\boldsymbol{\tau}) - \nabla p = \mathbf{0}, \tag{3.22}$$

which equals the balance of linear momentum (3.14). The described procedure permits to compute the effective viscosity of a mixture of viscous materials. However, we are interested in the effective viscosity of a suspension, i.e., of a mixture involving rigid inclusions. Because the viscosity inside these inclusions is infinite, the differential equation (3.14) is not, constitutively, well-defined. To handle this issue, we transfer to a dual formulation. Inside the infinitely viscous inclusions, the fluidity, i.e., the inverse of the viscosity, vanishes identically. Consequently, the associated equations are, constitutively, well-defined.
Instead of the effective dissipation potential (3.18) one may consider the effective complementary potential $\bar{\Phi}$, a function of the effective shear stress $\bar{\boldsymbol{\tau}}$, from which the constitutive law

$$\bar{\boldsymbol{D}}(\bar{\boldsymbol{\tau}}) = \frac{\partial \bar{\Phi}}{\partial \bar{\boldsymbol{\tau}}}(\bar{\boldsymbol{\tau}}), \tag{3.23}$$

arises dual to the primal relationship (3.20). To obtain the effective viscosity, a strategy based on the effective complementary potential requires to invert the effective law (3.23). To avoid this difficulty, we use

mixed "boundary conditions" (Kabel et al., 2016a), i.e., we consider the dual variational principle, but prescribe the effective shear rate tensor $\bar{\boldsymbol{D}}$. The convex dual of the variational problem (3.18) reads

$$\left\langle \Phi(\cdot, \boldsymbol{\tau}) - \boldsymbol{\tau} \cdot \bar{\boldsymbol{D}} \right\rangle_Y \longrightarrow \inf, \tag{3.24}$$

where the infimum is taken over all stress fields $\boldsymbol{\tau} : Y \to \mathsf{Sym}_0(3)$ which satisfy the equilibrium equation (3.14) for a suitable pressure field, see Wicht et al. (2020b, §4 and Appendix B).

3.2.3 Computational aspects and setup

After discussing theoretical aspects in the previous section, this section is dedicated to selected computational aspects concerning the fiber suspension microstructure and FFT-based procedure, starting with a solution scheme for the convex dual variatonal problem (3.24). The Euler-Lagrange equation of the convex dual variational problem (3.24) reads

$$\mathbb{P}_{\mathcal{E}} \left[\frac{\partial \Phi}{\partial \boldsymbol{\tau}}(\boldsymbol{\tau}_k) - \bar{\boldsymbol{D}} \right] = \boldsymbol{0}, \tag{3.25}$$

where $\mathbb{P}_{\mathcal{E}}$ denotes the L^2-projector onto the shear stresses satisfying the equilibrium equation (3.14). In terms of an arbitrary stepsize α, minimizers of the Euler-Lagrange equation (3.25) are fixed points of the gradient descent scheme

$$\boldsymbol{\tau}_{k+1} = \boldsymbol{\tau}_k - \alpha\, \mathbb{P}_{\mathcal{E}} \left[\frac{\partial \Phi}{\partial \boldsymbol{\tau}}(\boldsymbol{\tau}_k) - \bar{\boldsymbol{D}} \right], \tag{3.26}$$

which has a unique fixed point, provided the optimization problem (3.24) is strictly convex. For a closed form expression of the action of $\mathbb{P}_{\mathcal{E}}$ in Fourier space, and an analogous derivation of a fixed point scheme in the linear case, we refer to Bertóti et al. (2021). Numerical schemes based on the gradient descent iteration (3.26) require computing a strain rate

$\boldsymbol{D}$ resulting from a shear stress $\boldsymbol{\tau}$ at every continuum point $\boldsymbol{x}$ and for every iteration. Treating fibers is particularly simple: the strain rate $\boldsymbol{D}$ vanishes since the inclusions are rigid.
To solve the equation

$$\boldsymbol{\tau} = 2\eta(\dot{\gamma})\,\boldsymbol{D} \tag{3.27}$$

for the strain rate $\boldsymbol{D}$, compare equation (3.1), we first take norms on both sides to arrive at the equation

$$\|\boldsymbol{\tau}\| = 2\eta(\dot{\gamma})\,\|\boldsymbol{D}\| \equiv \sqrt{2}\eta(\dot{\gamma})\dot{\gamma}. \tag{3.28}$$

We use Newton's method to find a root of the function

$$g(\dot{\gamma}) = \|\boldsymbol{\tau}\| - \sqrt{2}\eta(\dot{\gamma})\dot{\gamma}, \tag{3.29}$$

and thus compute iteratively

$$\dot{\gamma}_{n+1} = \dot{\gamma}_n - s_n \frac{g(\dot{\gamma}_n)}{g'(\dot{\gamma}_n)}. \tag{3.30}$$

Using backtracking for the step size s_n to ensure that the Armijo-Goldstein inequality(Armijo, 1966; Goldstein, 1965) holds. For the Cross fluid (3.2), the derivative of the function g computes as

$$g'(\dot{\gamma}) = -\sqrt{2}\left(\eta(\dot{\gamma}) - \frac{m(\eta_0 - \eta_\infty)(k\dot{\gamma})^m}{(1+(k\dot{\gamma})^m)^2}\right). \tag{3.31}$$

Once the scalar shear rate $\dot{\gamma}$ is identified, we compute the strain rate tensor $\boldsymbol{D}$ via

$$\boldsymbol{D} = \frac{\boldsymbol{\tau}}{2\eta(\dot{\gamma})}. \tag{3.32}$$

The fiber suspension microstructures were generated with the sequential addition and migration method (Schneider, 2017), and discretized on a staggered grid (Harlow and Welch, 1965) to ensure stability for incompressible material models. The resulting equation system was

solved with the Barzilai-Borwein method (Barzilai and Borwein, 1988; Bertóti et al., 2021) in the Newtonian case, while a non-linear Newton-CG approach (Dembo et al., 1982; Schneider, 2020a) was used in the Cross-type case. For validation purposes, we compared computational results of the presented FFT-based approach with computational results from literature (Traxl et al., 2020), see section 3.3.1. For a detailed overview on solvers for the non-linear Lippmann-Schwinger equation in the closely related case of solid mechanics (3.26), see Schneider (2020b). For proofs on the existence and uniqueness of solutions to the considered non-linear homogenization problem (3.24), we refer to Schneider (2016). Further details on the employed FFT-based homogenization approach including solvers and discretization, we refer to Bertóti et al. (2021) and Schneider (2020a).

To numerically obtain an effective viscosity or fluidity with the integral equations (3.8) and (3.13), the respective integral, and the derivatives occurring in the integrand need to be discretized. In combination with the costly computation of the effective stresses or strains this renders the required computational effort to obtain an effective viscosity prohibitively large. Instead, we employ equation (3.7) to estimate an effective, viscosity-like quantity solely from computationally obtained effective stresses $\bar{\boldsymbol{\tau}}$, by using the following equation in Mandel's notation (Bertóti et al., 2021)

$$\underline{\bar{\tau}} = \underline{\underline{\bar{V}}}\,\underline{\bar{D}}, \quad \text{i.e.,} \quad \underline{\bar{V}} = \underline{\bar{\tau}}\,\underline{\underline{\bar{D}}}^{\dagger}. \tag{3.33}$$

Here, $(\cdot)^\dagger$ denotes the Moore-Penrose pseudoinverse which is equal to an inversion on $\mathsf{Sym}_0(3)$, $\bar{\underline{\underline{\tau}}}$ collects the computed effective stresses

$$\bar{\underline{\underline{\tau}}} = \begin{bmatrix} \bar{\tau}_{11}^{(1)} & \bar{\tau}_{11}^{(2)} & \bar{\tau}_{11}^{(3)} & \bar{\tau}_{11}^{(4)} & \bar{\tau}_{11}^{(5)} & \bar{\tau}_{11}^{(6)} \\ \bar{\tau}_{22}^{(1)} & \bar{\tau}_{22}^{(2)} & \bar{\tau}_{22}^{(3)} & \bar{\tau}_{22}^{(4)} & \bar{\tau}_{22}^{(5)} & \bar{\tau}_{22}^{(6)} \\ \bar{\tau}_{33}^{(1)} & \bar{\tau}_{33}^{(2)} & \bar{\tau}_{33}^{(3)} & \bar{\tau}_{33}^{(4)} & \bar{\tau}_{33}^{(5)} & \bar{\tau}_{33}^{(6)} \\ \sqrt{2}\bar{\tau}_{23}^{(1)} & \sqrt{2}\bar{\tau}_{23}^{(2)} & \sqrt{2}\bar{\tau}_{23}^{(3)} & \sqrt{2}\bar{\tau}_{23}^{(4)} & \sqrt{2}\bar{\tau}_{23}^{(5)} & \sqrt{2}\bar{\tau}_{23}^{(6)} \\ \sqrt{2}\bar{\tau}_{13}^{(1)} & \sqrt{2}\bar{\tau}_{13}^{(2)} & \sqrt{2}\bar{\tau}_{13}^{(3)} & \sqrt{2}\bar{\tau}_{13}^{(4)} & \sqrt{2}\bar{\tau}_{13}^{(5)} & \sqrt{2}\bar{\tau}_{13}^{(6)} \\ \sqrt{2}\bar{\tau}_{12}^{(1)} & \sqrt{2}\bar{\tau}_{12}^{(2)} & \sqrt{2}\bar{\tau}_{12}^{(3)} & \sqrt{2}\bar{\tau}_{12}^{(4)} & \sqrt{2}\bar{\tau}_{12}^{(5)} & \sqrt{2}\bar{\tau}_{12}^{(6)} \end{bmatrix} \tag{3.34}$$

and $\bar{\underline{\underline{D}}}$ collects the investigated load cases

$$\bar{\underline{\underline{D}}} = \dot{\gamma}\sqrt{\frac{2}{3}} \begin{bmatrix} 1 & -\frac{1}{2} & -\frac{1}{2} & 0 & 0 & 0 \\ -\frac{1}{2} & 1 & -\frac{1}{2} & 0 & 0 & 0 \\ -\frac{1}{2} & -\frac{1}{2} & 1 & 0 & 0 & 0 \\ 0 & 0 & 0 & \sqrt{\frac{3}{2}} & 0 & 0 \\ 0 & 0 & 0 & 0 & \sqrt{\frac{3}{2}} & 0 \\ 0 & 0 & 0 & 0 & 0 & \sqrt{\frac{3}{2}} \end{bmatrix}. \tag{3.35}$$

The i-th column in the matrix $\bar{\underline{\underline{\tau}}}$ contains the effective shear stress corresponding to the particular applied shear rate that is listed in the i-th column of the matrix $\bar{\underline{\underline{D}}}$. In the Newtonian case, the matrix $\bar{\underline{\underline{V}}}$ encodes the components of the viscosity tensor because of superposition. Since superposition is not generally valid in the non-Newtonian case, the matrix $\bar{\underline{\underline{V}}}$ acts as an interpolation between the six calculated effective stresses $\bar{\underline{\underline{\tau}}}$. Additionally, the load cases $\bar{\underline{\underline{D}}}$ are not uniquely defined and interpolation between the effective stresses $\bar{\underline{\underline{\tau}}}$ is qualitative in nature. However, the matrix $\bar{\underline{\underline{V}}}$ provides quantitatively robust information in the load cases collected in $\bar{\underline{\underline{D}}}$, and its interpolating property allows us to draw intuition for the results in between. Thus, even in the non-Newtonian case, the matrix $\bar{\underline{\underline{V}}}$ may be used to investigate the viscous suspension

behavior. We will refer to $\bar{\underline{\underline{V}}}$ as the suspension viscosity throughout the article.

3.2.4 A model for the fiber suspension viscosity

Typically, it is not feasible to take the large amount of information contained in the fiber orientation distribution function (2.29) into account at every spatial element of component-scale simulations. To reduce the necessary computational effort in treating fiber orientation states, it is common to use the fiber orientation tensors of second and fourth order (Advani and Tucker III, 1987; Kanatani, 1984)

$$\bar{\boldsymbol{N}} = \int_{S^2} \boldsymbol{n} \otimes \boldsymbol{n}\, \rho(\boldsymbol{n})\, \mathrm{d}S(\boldsymbol{n}), \tag{3.36}$$

$$\bar{\mathbb{N}} = \int_{S^2} \boldsymbol{n} \otimes \boldsymbol{n} \otimes \boldsymbol{n} \otimes \boldsymbol{n}\, \rho(\boldsymbol{n})\, \mathrm{d}S(\boldsymbol{n}). \tag{3.37}$$

Both tensors $\boldsymbol{N}$ and $\mathbb{N}$ are completely symmetric, positive semi-definite, and contract with the second-order unity tensor $\mathbf{1}$ such that

$$\bar{\boldsymbol{N}} \cdot \mathbf{1} = 1, \tag{3.38}$$

$$\bar{\mathbb{N}}[\mathbf{1}] = \boldsymbol{N}. \tag{3.39}$$

With these two descriptors at hand, a large variety of anisotropic mean-field models has been built to model material behavior (Karl and Böhlke, 2022). In the case of a transversely isotropic fluid with constant viscosity, a convenient approximation of the popular Mori-Tanaka model is

available with (Bertóti, 2021)

$$\begin{aligned}\mathbb{V}_{\mathsf{MT}} &= 2\eta_{\mathsf{MF}}\left(\mathbb{P}_2 + N_{\mathsf{p}}^{\mathsf{MF}}\,\mathbb{P}_2\,\mathbb{N}\,\mathbb{P}_2\right),\\ \eta_{\mathsf{MF}} &= \frac{1+c_{\mathsf{F}}}{1-c_{\mathsf{F}}}\eta,\\ N_{\mathsf{p}}^{\mathsf{MF}} &= \frac{c_{\mathsf{F}}}{1+c_{\mathsf{F}}}\frac{r_{\mathsf{a}}^2}{2(\ln(2r_{\mathsf{a}})-3/2)}.\end{aligned} \tag{3.40}$$

Here, η_{MF} is the effective scalar viscosity, and $N_{\mathsf{p}}^{\mathsf{MF}}$ is the particle number. This model is derived by decomposing the microstructure into m transversely isotropic pseudo domains containing a single fiber and the matrix material. In a first step, the unidirectional effective viscosities $\mathbb{V}_{\mathsf{UD}}^m$ of these m pseudodomains are approximated with the Mori-Tanaka method by

$$\mathbb{V}_{\mathsf{UD}}^m = 2\eta\,\mathbb{P}_2 + \frac{c_{\mathsf{F}}}{1-c_{\mathsf{F}}}\mathbb{P}_m^{-1}, \tag{3.41}$$

where $\mathbb{P}_m$ is the polarization tensor depending on the matrix material properties and the fiber geometry. The expression (3.41) equals the lower Hashin-Shtrikman bound (Willis, 1977). In a second step, the effective viscosity of the volume element is calculated by orientation averaging the unidirectional effective viscosities $\mathbb{V}_{\mathsf{UD}}^m$ via

$$\mathbb{V}_{\mathsf{MT}} = \frac{1}{M}\sum_{m=1}^{M}\boldsymbol{V}_{\mathsf{UD}}^m. \tag{3.42}$$

The Voigt-type average (3.42) yields an upper bound on the dissipation (Bertóti and Böhlke, 2017). However, this model is only applicable for fluids with constant viscosity, since it does not depend on the shear rate $\dot{\gamma}$. One possible extension to incorporate shear rate dependency in the case of rigid fibers is (Karl and Böhlke, 2022)

$$\eta_{\mathsf{MF}} = \frac{1+c_{\mathsf{F}}}{1-c_{\mathsf{F}}}\eta\left(\frac{\dot{\gamma}}{1-c_{\mathsf{F}}}\right), \tag{3.43}$$

which recovers the Newtonian case for the shear rate limits $\dot{\gamma} \to 0$ and $\dot{\gamma} \to \infty$ in the considered Cross-type case. In section 3.4.3, results obtained with both the Newtonian (3.40) and Cross-type (3.43) Mori-Tanaka model are compared to results of the FFT-based computational approach presented in section 3.2.3.

3.2.5 Material parameters

In the previous sections 3.2.2 and 3.2.4, we discussed some aspects of FFT-based homogenization and analytical modeling of fiber suspensions. In this section, we describe the material and microstructure properties considered in this chapter. In the following, we are concerned with microstructures of fiber polymer suspensions, and we consider a commercially available polyamide 6 (PA6) (BASF, 2020) as matrix material in all computational studies. A Cross-type material law (3.2) was fitted to PA6 material data available for shear rates $\dot{\gamma}$ in the interval $[1.7, 16300]\,\mathrm{s}^{-1}$ for a temperature of $250°\mathrm{C}$. The available material data as well as the fit are visualized in Figure 3.1, and the resulting model parameters are $\eta_0 = 288.9\ \mathrm{Pa\,s}$, $\eta_\infty = 15.0\ \mathrm{Pa\,s}$, $k = 10.9 \cdot 10^{-4}$, and $m = 1.1$. For all studied cases with Newtonian matrix behavior, the shear rate dependent matrix viscosity η was chosen as $\eta = \eta_0$.

Typical shear rates $\dot{\gamma}$ in compression molding processes are below $5 \cdot 10^1\ \mathrm{s}^{-1}$, while the shear rates in injection molding processes are typically kept below $1 \cdot 10^5\ \mathrm{s}^{-1}$ for most materials (Valero, 2020, Sec. 21.6.8), but can go above $1 \cdot 10^6\ \mathrm{s}^{-1}$ in thin-wall and micro molding (Friesenbichler et al., 2011). To cover some of the process-relevant shear rate intervals for both compression and injection molding processes, computational investigations were conducted for the macroscopic scalar shear rates

$$\dot{\gamma} \in S_{\dot{\gamma}} = \{a \cdot 10^b\ \mathrm{s}^{-1} |\ a = 1, 2, 5;\ b = 1, 2, 3, 4\} \cup \{10^5\}. \tag{3.44}$$

Because the Cross-type matrix viscosity changes only slightly for shear rates $\dot{\gamma}$ larger than $1 \cdot 10^5\ \mathrm{s}^{-1}$, shear rates above $1 \cdot 10^5\ \mathrm{s}^{-1}$ were not investigated.

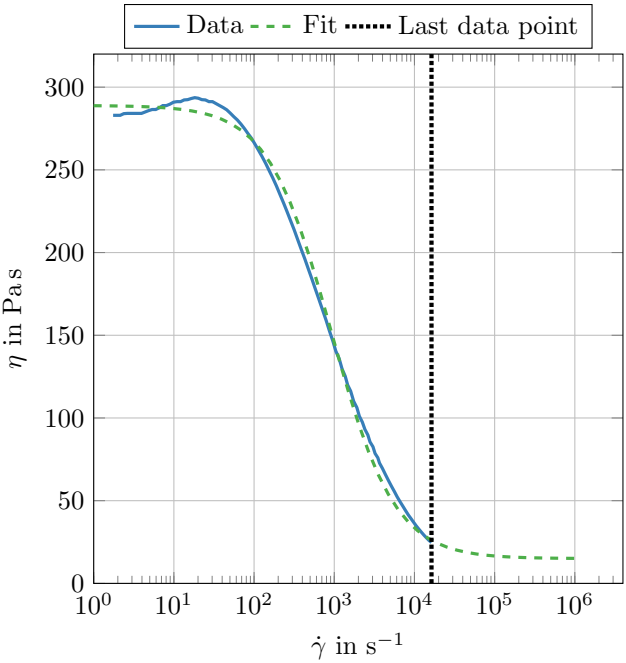

Figure 3.1: Material data and Cross-type fit for Ultramid®B3K. Figure adapted from Sterr et al. (2023, Figure 1).

Overall, a thorough orientation state dependent investigation of the suspension viscosity takes a large amount of computational resources. Since the focus of this chapter lies in identifying the underlying effects of shear-thinning rheology on the fiber suspension viscosity, one particular orientation state was considered for our investigations. Because strongly oriented fiber orientation states are very common in injection and com-

pression molding (Vincent et al., 2005; Park et al., 2001), the second order fiber orientation tensor $\mathbf{N}$ of the considered microstructure was chosen to be transversely isotropic such that

$$\mathbf{N} = \begin{bmatrix} 0.8 & 0 & 0 \\ 0 & 0.1 & 0 \\ 0 & 0 & 0.1 \end{bmatrix}_{\{\boldsymbol{e}_i \otimes \boldsymbol{e}_j\}} . \tag{3.45}$$

While this particular choice of fiber orientation state is strongly oriented, other fiber orientation states are of research and engineering interest as well. However, to focus on the particularities and influence of the Cross-type matrix material on the non-Newtonian fiber suspension viscosity, we restrict the scope of this chapter to the given orientation state. The symmetry of the underlying microstructure is also reflected in the suspension viscosity $\underline{\underline{\bar{V}}}$. Hence, if the computational volume element was chosen sufficiently large, we expect the computed suspension viscosity $\underline{\underline{\bar{V}}}$ to be transversely isotropic as well. We use this fact in section 3.4 to complement the volume element study detailed in section 3.3.3.

3.3 Preliminary studies

3.3.1 Validation against computational results from literature

Traxl et al. (2020) investigated the suspension viscosity of rigid spheres suspended in a non-Newtonian matrix fluid using the finite element method. For validation purposes, we compare results obtained with the presented FFT-based homogenization approach to results from Traxl et al. (2020). The microstructures of interest include twenty spheres, contain a sphere volume fraction of $c_\mathrm{S} = 10\%$, and were generated based on the mechanical contraction method of Williams-Philipse (Williams and

Philipse, 2003). The spheres are suspended in a Cross-type (3.2) matrix fluid with the same parameters as in Traxl et al. (2020): $\eta_0 = 1.5\,\mathrm{Pa\,s}$, $\eta_\infty = 0.5\,\mathrm{Pa\,s}$, $k = 2$, $n = 0.8$. To replicate the procedure detailed in Traxl et al. (2020), five different realizations of the microstructure were generated and resolved with 256^3 voxels, see Figure 3.2. As effective loads,

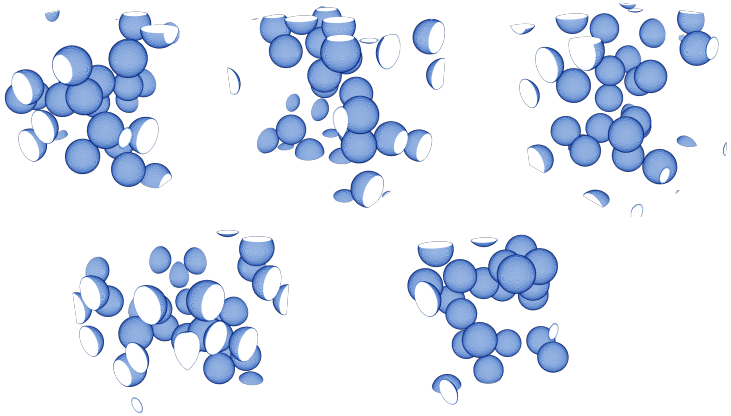

Figure 3.2: Five microstructures with a sphere volume fraction of $c_\mathsf{F} = 10\%$. Figure adapted from Sterr et al. (2023, Figure 2).

twenty-one effective stresses $\bar{\underline{\underline{\boldsymbol{\tau}}}}$ of the form $\bar{\underline{\underline{\boldsymbol{\tau}}}} = [0,\ 0,\ 0,\ 0,\ 0,\ \bar{\tau}_{12}]$ were applied to each microstructure, with the effective stress components $\bar{\tau}_{12}$ being linearly spaced on the interval $[0.089, 0.914]\mathrm{Pa}$. Here, the interval bounds of the effective stress components $\bar{\tau}_{12}$ were extracted from the results of Traxl et al. (2020). For each microstructure m, the resulting effective shear rate $\dot{\gamma}_m^{\mathsf{FFT}}(\bar{\tau}_{12})$ in response to the loads $\bar{\underline{\underline{\boldsymbol{\tau}}}}$ was measured, and then used to calculate an average effective shear rate $\dot{\gamma}_\mathsf{A}^{\mathsf{FFT}}(\bar{\tau}_{12})$ via

$$\dot{\gamma}_\mathsf{A}^{\mathsf{FFT}}(\bar{\tau}_{12}) = \frac{1}{5}\sum_{i=1}^{5}\dot{\gamma}_i^{\mathsf{FFT}}(\bar{\tau}_{12}). \tag{3.46}$$

Subsequently, the average effective shear rate $\dot{\gamma}_{\mathsf{A}}^{\mathsf{FFT}}(\bar{\tau}_{12})$ was compared to the average effective shear rate $\dot{\gamma}_{\mathsf{A}}^{\mathsf{lit}}(\bar{\tau}_{12})$ given in Traxl et al. (2020) via the deviation d_{num}, which we define as

$$d_{\mathsf{num}} = \frac{|\dot{\gamma}_{\mathsf{A}}^{\mathsf{lit}}(\bar{\tau}_{12}) - \dot{\gamma}_{\mathsf{A}}^{\mathsf{FFT}}(\bar{\tau}_{12})|}{\dot{\gamma}_{\mathsf{A}}^{\mathsf{lit}}(\bar{\tau}_{12})}. \tag{3.47}$$

The resulting effective shear rate-stress curves for the FFT-based method is in very good agreement with the results from Traxl et al. (2020), see Figure 3.3a. This is emphasized by the deviation d_{num}, which lies below 2.3% for all investigated effective loads $\underline{\bar{\boldsymbol{\tau}}}$, see Figure 3.3b.

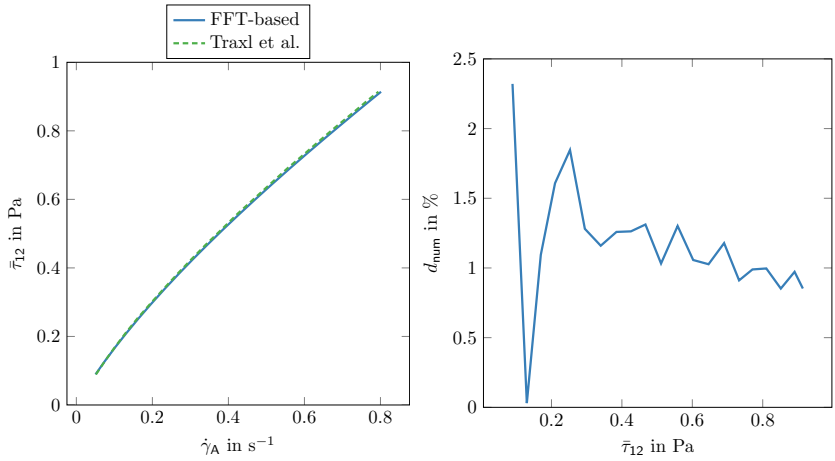

(a) Effective shear rate-stress curves

(b) Deviation d_{num}

Figure 3.3: Comparison of the effective shear rate-stress curves given in Traxl et al. (2020) and the effective shear rate-stress curves obtained from FFT-based simulations, as well as their deviation d_{num} for effective stress components $\bar{\tau}_{12} \in [0.089, 0.914]\mathrm{Pa}$. Figure adapted from Sterr et al. (2023, Figure 3).

3.3.2 Resolution Study

The resolution of the microstructure discretization is limited by computational resources, namely memory and runtime. To determine a suitable resolution that accommodates limited resources, and allows for an appropriately small error, we conducted a resolution study for the cases of Newtonian and Cross-type (3.2) matrix behavior. We conducted the study for a fixed fiber aspect ratio $r_a = 10$ and for fiber volume fractions $c_F \in \{5\%, 10\%, 15\%, 20\%, 25\%\}$. Since the inter fiber distance decreases with increasing volume fraction c_F, the effective stress $\bar{\boldsymbol{\tau}}$ of the suspension is expected to be more sensitive to resolution effects for higher fiber volume fractions c_F. Consequently, we chose the maximum considered volume fraction $c_F = 25\%$ for all volume elements in the resolution study. To reduce the amount of necessary voxels, we investigated two types of voxel discretizations, namely binary and composite voxels (Kabel et al., 2017). For the composite voxels, we used the general dual mixing rule

$$\bar{\boldsymbol{\tau}}_V = c_M \boldsymbol{\tau}_M + (1 - c_M)\boldsymbol{\tau}_F \tag{3.48}$$

where $\bar{\boldsymbol{\tau}}_V$, c_M, $\boldsymbol{\tau}_M$, and $\boldsymbol{\tau}_F$ are the effective stress, the matrix volume fraction, the matrix stress, and the fiber stress inside the composite voxel, respectively. In the special case of rigid fibers, the fiber stress $\boldsymbol{\tau}_F$ is zero. Hence, the general composite voxel mixing rule (3.48) simplifies to

$$\bar{\boldsymbol{\tau}}_V = c_M \boldsymbol{\tau}_M. \tag{3.49}$$

Like in Bertóti et al. (2021), we increased the number of voxels per fiber diameter v/d in dyadic steps for the binary voxels, such that $v/d \in \{5, 10, 20, 40\}$, see Figure 3.4.

Hence, a single microstructure was discretized with the resolutions $v/d \in \{5, 10, 20, 40\}$ for binary voxels and $v/d \in \{5, 10, 20\}$ for composite

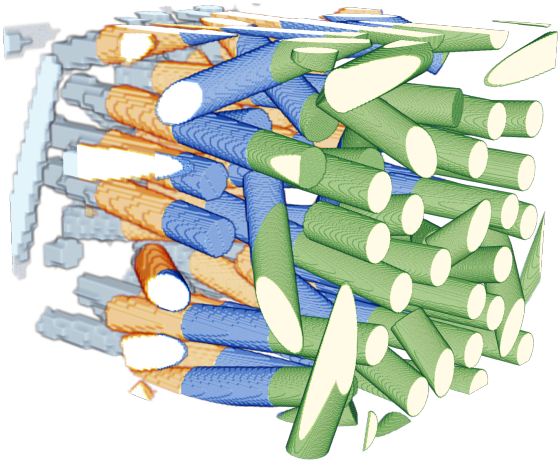

Figure 3.4: Microstructure where four differently colored segments are shown with varying voxels per fiber diameter v/d. Segments from left to right: gray ($v/d = 5$), orange ($v/d = 10$), blue ($v/d = 20$), green ($v/d = 40$). Figure adapted from Sterr et al. (2023, Figure 4).

voxels, and the effective stress $\bar{\boldsymbol{\tau}}$ was calculated for all considered shear rates and loading directions.

We define the relative error caused by the resolution as

$$e_{\mathsf{res}} = \frac{\|\bar{\boldsymbol{\tau}} - \bar{\boldsymbol{\tau}}_{\mathsf{fine}}\|_2}{\|\bar{\boldsymbol{\tau}}_{\mathsf{fine}}\|_2}, \tag{3.50}$$

where $\bar{\boldsymbol{\tau}}$ is the effective stress for an arbitrary resolution $v/d < 40$ and $\bar{\boldsymbol{\tau}}_{\mathsf{fine}}$ is the binary voxel result for a resolution of $v/d = 40$. Therefore, the effective stress $\bar{\boldsymbol{\tau}}$ for each resolution, voxel type, and load case is compared to the load specific reference stress $\bar{\boldsymbol{\tau}}_{\mathsf{fine}}$. For a particular voxel type and a given resolution v/d, we define the set S_{e} that collects the resolution errors e_{res} for all investigated load cases as

$$S_{\mathsf{e}} = \left\{ e_{\mathsf{res}} \left(\bar{\boldsymbol{\tau}}^{(i)}(\dot{\gamma}), \bar{\boldsymbol{\tau}}^{(i)}_{\mathsf{fine}}(\dot{\gamma}) \right) \mid i = 1,2,3,4,5,6,\ \dot{\gamma} \in S_{\dot{\gamma}} \right\}, \tag{3.51}$$

where $\bar{\boldsymbol{\tau}}^{(i)}(\dot{\gamma})$ is the material response to the load case collected in the i-th column of $\bar{\underline{\underline{D}}}(\dot{\gamma})$, see equation (3.35), and $\bar{\boldsymbol{\tau}}^{(i)}_{\mathsf{fine}}(\dot{\gamma})$ is the corresponding reference stress. Additionally, we define the minimum, maximum, and mean error for a particular voxel type and a particular resolution as

$$e_{\mathsf{min}} = \min S_{\mathsf{e}}, \quad e_{\mathsf{max}} = \max S_{\mathsf{e}}, \quad e_{\mathsf{mean}} = \sum_{e_{\mathsf{res}} \in S_{\mathsf{e}}} e_{\mathsf{res}} / |S_{\mathsf{e}}|, \tag{3.52}$$

where $|S_{\mathsf{e}}|$ denotes the cardinality of the set S_{e}. The quantitative values for the error measures e_{min}, e_{max}, and e_{mean} are visualized in Figure 3.5 for binary and composite voxels and for the resolutions $v/d \in \{5, 10, 20, 40\}$. For all resolutions, the minimum, maximum and mean errors e_{min}, e_{max},

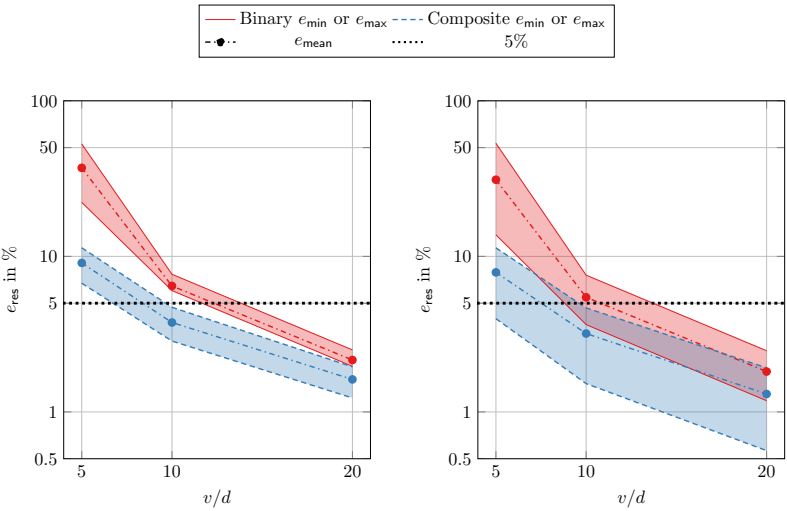

(a) Newtonian case **(b)** Cross-type case

Figure 3.5: Convergence of the relative resolution error (3.50) for the Newtonian case (a) and the Cross-type case (b). Figure adapted from Sterr et al. (2023, Figure 5).

and e_{mean} decrease with the resolution v/d. In both the Newtonian

and Cross-type case, and for all resolutions v/d, the values of the three errors (3.52) are lower for the composite voxels than for the binary voxels. Most notably, the maximum error e_{max} falls below 5% at a resolution $v/d = 20$ for the binary voxel model, but already does so at a resolution $v/d = 10$ when using composite voxels.
Intriguingly, the minimum errors e_{min} are consistently lower in the Cross-type case than in the Newtonian case, while the maximum errors e_{max} remain on a similar level. We note that the lowest errors e_{min} occur, independent of the resolution v/d, for the pure shear load case $\underline{\bar{D}} = \dot{\gamma}[0\,0\,0\,0\,1\,0]$ at a shear rate $\dot{\gamma} = 2 \cdot 10^3\,\mathrm{s}^{-1}$. The maximum errors e_{max} occur at the lowest investigated shear rate of $\dot{\gamma} = 10\,\mathrm{s}^{-1}$ for the elongational load cases which are collected in the 1st, 2nd, and 3rd column of $\underline{\bar{D}}$, see equation (3.35). Thus, some of the investigated load cases lead to a reduced resolution requirement or the reference solution is less accurate, which is an effect also observed in elastoplastic material models in solid mechanics (Schneider and Wicht, 2023). To ensure a resolution error e_{res} below 5% for all load cases, a resolution of $v/d = 15$ was chosen for all following computations.

3.3.3 Volume element size

Like the resolution of the microstructure discretization, the size of the volume element under investigation is limited by computational resources. Appropriate volume element sizes for fiber suspensions with Newtonian matrix behavior with aspect ratios $r_{\mathsf{a}} = 10$ and fiber volume fractions c_{F} up to 25% were investigated by Bertóti et al. (2021). Depending on the fiber orientation, different representative volume element sizes were identified by Bertóti et al. (2021), and in the case of aligned fibers, a volume element of the form $2.2\ell \times 20d \times 20d$ was identified as sufficiently representative. Adding to these insights, we conducted a study to determine a suitable size of the volume element for the considered transversely isotropic orientation state in

the Cross-type case, with a fiber aspect ratio $r_a = 10$, and fiber volume fractions $c_F \in \{5\%, 10\%, 15\%, 20\%, 25\%\}$. Because the necessary volume element size grows with the fiber volume fraction c_F, we chose $c_F = 25\%$ for the volume element study. We investigated volume elements of the form $L \times W \times W$, where $L \in \{1.1\ell, 2.2\ell, 3.2\ell\}$ and $W \in \{5d, 10d, 20d\}$ with fiber length ℓ and the fiber diameter d, see Figure 3.6. To discretize the microstructures, we employed composite voxels and used a resolution of $v/d = 15$, as identified in the previous section.

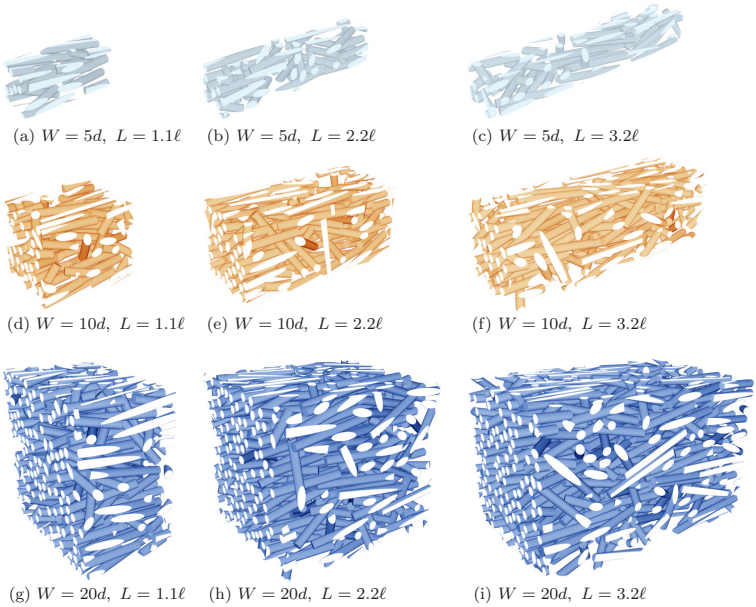

Figure 3.6: Comparison of microstructures with dimensions $L \times W \times W$, lengths $L \in \{1.1\ell, 2.2\ell, 3.2\ell\}$, and widths $W \in \{5d, 10d, 20d\}$. Figure adapted from Sterr et al. (2023, Figure 6).

For every combination of length L and width W, ten different microstructures were generated, and their effective stresses $\bar{\boldsymbol{\tau}}$ were calculated for

all considered shear rates (3.44) and loading directions (3.35). We define the relative error caused by the volume element size as

$$e_{\mathsf{VE}} = \frac{\|\bar{\boldsymbol{\tau}} - \bar{\boldsymbol{\tau}}_{\mathsf{ref}}\|_2}{\|\bar{\boldsymbol{\tau}}_{\mathsf{ref}}\|_2}. \tag{3.53}$$

For each individual load case, the effective stress $\bar{\boldsymbol{\tau}}$ of the ten largest microstructures with length $L = 3.2\ell$ and width $W = 20d$ was averaged and chosen as the reference stress $\bar{\boldsymbol{\tau}}_{\mathsf{ref}}$. Thus, for each volume element size, the effective stress $\bar{\boldsymbol{\tau}}$ of each of the ten realizations is compared to the average reference stress $\bar{\boldsymbol{\tau}}_{\mathsf{ref}}$. This allows us to calculate the means and standard deviations of the relative error e_{VE} for each combination of length L and width W, which are collected in Table 3.1.

First, we note that the mean and standard deviation of the relative error e_{VE} decrease faster with the width W than with the length L. The largest decrease in the mean and standard deviation of e_{VE} occurred when the width W was increased from $W = 5$ to $W = 10$. Thus, an appropriate choice of the volume width is essential to obtain robust results. Overall, we observe that the maximum value of the error e_{VE} falls below the engineering bound of 5% for the sizes $L = 2.2\ell$, $W = 20d$ and $L = 3.2\ell$, $W = 20d$, where the maximum of the error e_{VE} is 4.06% and 3.05%, respectively.

With mean errors of 1.75% and 1.14%, and error standard deviations of 0.82% and 0.51%, both sizes $L = 2.2\ell$, $W = 20d$ and $L = 3.2\ell$, $W = 20d$ show similar error characteristics. Consequently, we consider the size of the volume element $L = 2.2\ell$, $W = 20d$ as sufficient, which aligns with the results for aligned fibers in the Newtonian case of Bertóti et al. (2021). Accordingly, we choose $L = 2.2\ell$, $W = 20d$ for all further investigations.

L	W	Mean $\pm$ std	Max	L	W	Mean $\pm$ std	Max
1.2ℓ	5d	37.48 ± 19.0	106.21	2.2ℓ	5d	29.76 ± 15.68	78.97
	10d	5.06 ± 4.03	23.89		10d	3.75 ± 2.5	11.11
	20d	3.62 ± 2.28	10.96		20d	1.75 ± 0.82	4.06

L	W	Mean $\pm$ std	Max
3.2ℓ	5d	9.71 ± 5.52	27.73
	10d	3.28 ± 1.68	8.55
	20d	1.14 ± 0.51	3.05

Table 3.1: Mean, standard deviation, and maximum value of the relative error e_{VE} (3.53) in %, computed with ten realizations per combination of length factor l and width factor w. Table adapted from Sterr et al. (2023, Table 1).

3.4 Computational investigations

3.4.1 Spatial representation of the suspension viscosity through a scalar elongational viscosity

Böhlke and Brüggemann (2001) introduced a simple method to visualize an anisotropic stiffness tensor. We modify this approach to calculate the fiber polymer suspension's resistance to elongational flow in a particular direction via an elongational viscosity η_{app}. In the general non-Newtonian case, we define a direction-dependent, elongational viscosity η_{app}

$$\eta_{\mathsf{app}}(\dot{\gamma}, c_{\mathsf{F}}, \boldsymbol{d}) = \underline{a}(\boldsymbol{d})^{\mathsf{T}} \underline{\underline{\bar{V}}}(\dot{\gamma}, c_{\mathsf{F}})\, \underline{a}(\boldsymbol{d}) \;\approx\; \mathbb{V}(\dot{\gamma}, c_{\mathsf{F}}) \cdot (\boldsymbol{d} \otimes \boldsymbol{d} \otimes \boldsymbol{d} \otimes \boldsymbol{d}), \quad (3.54)$$

where $\underline{a}(\boldsymbol{d})$ denotes the components of $\boldsymbol{d} \otimes \boldsymbol{d}$ in Mandel notation, $\boldsymbol{d}$ is the elongation direction, and the suspension viscosity $\underline{\underline{\bar{V}}}(\dot{\gamma}, c_{\mathsf{F}})$ is calculated via equation (3.33) as an approximation of the true suspension viscosity tensor $\mathbb{V}(\dot{\gamma}, c_{\mathsf{F}})$. Since the true suspension viscosity tensor $\mathbb{V}$ has the minor and major symmetries, it is defined by 21 components. As a consequence, the suspension viscosity $\underline{\underline{\bar{V}}}(\dot{\gamma}, c_{\mathsf{F}})$ can be completely described by a scalar elongational viscosity and a scalar dilatational

viscosity, see He and Curnier (1995, Sec. 4.3). The elongational and dilatational viscosity then contain the information of 15 and 6 components of the suspension viscosity $\underline{\underline{\bar{V}}}(\dot{\gamma}, c_\mathsf{F})$, respectively. However, due to incompressibility, all information contained in the suspension viscosity $\underline{\underline{\bar{V}}}(\dot{\gamma}, c_\mathsf{F})$ is completely and uniquely encoded via the elongational viscosity $\eta_{\mathsf{app}}(\dot{\gamma}, c_\mathsf{F}, \boldsymbol{d})$ (He and Curnier, 1995, Sec. 4.3). This holds in both the Newtonian and Cross-type case. Thus, in the following, we use the elongational viscosity $\eta_{\mathsf{app}}(\dot{\gamma}, c_\mathsf{F})$ as a tool to completely visualize and qualitatively understand the suspension viscosity $\underline{\underline{\bar{V}}}(\dot{\gamma}, c_\mathsf{F})$.

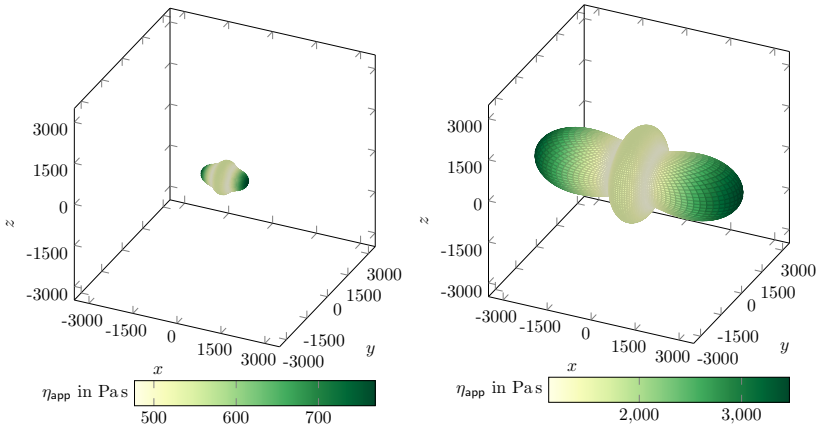

(a) $c_\mathsf{F} = 5\%$ **(b)** $c_\mathsf{F} = 25\%$

Figure 3.7: Apparent viscosity η_{app} in the Newtonian case for fiber volume fractions $c_\mathsf{F} = 5\%$ (a) and $c_\mathsf{F} = 25\%$ (b). Figure adapted from Sterr et al. (2023, Figure 7).

For the special case of an isotropic suspension viscosity, and a uniaxial elongation direction $\boldsymbol{d}$, the elongational viscosity $\eta_{\mathsf{app}}(\dot{\gamma}, \boldsymbol{d})$ is related to the shear viscosity $\eta(\dot{\gamma})$ (3.2) such that $\eta_{\mathsf{app}}(\dot{\gamma}, \boldsymbol{d}) = 4\eta(\dot{\gamma})/3$. In the Newtonian case, the viscosity tensor components $\underline{\underline{\bar{V}}}(\dot{\gamma}, c_\mathsf{F})$ are independent of the shear rate $\dot{\gamma}$.

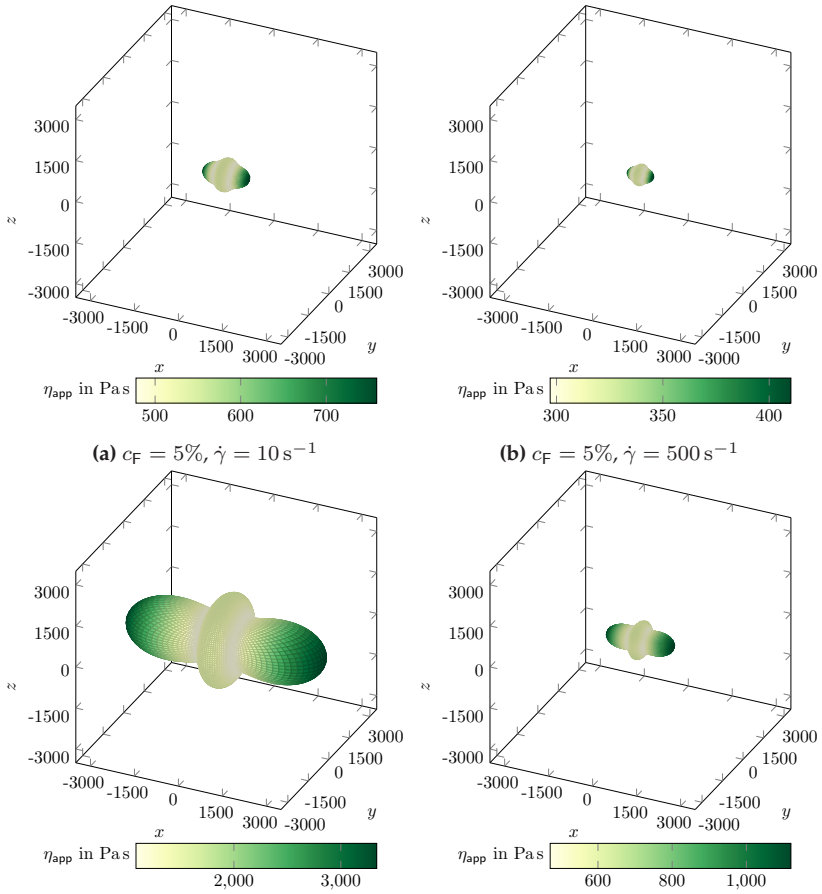

(a) $c_\mathsf{F} = 5\%, \dot{\gamma} = 10\,\mathrm{s}^{-1}$ **(b)** $c_\mathsf{F} = 5\%, \dot{\gamma} = 500\,\mathrm{s}^{-1}$

(c) $c_\mathsf{F} = 25\%, \dot{\gamma} = 10\,\mathrm{s}^{-1}$ **(d)** $c_\mathsf{F} = 25\%, \dot{\gamma} = 500\,\mathrm{s}^{-1}$

Figure 3.8: Apparent viscosity η_app in the Cross-type case for combinations of fiber volume fractions c_F and shear rate $\dot{\gamma}$: $c_\mathsf{F} = 5\%, \dot{\gamma} = 10\,\mathrm{s}^{-1}$ (a), $c_\mathsf{F} = 5\%, \dot{\gamma} = 500\,\mathrm{s}^{-1}$ (b), $c_\mathsf{F} = 25\%, \dot{\gamma} = 10\,\mathrm{s}^{-1}$ (c), and $c_\mathsf{F} = 25\%, \dot{\gamma} = 500\,\mathrm{s}^{-1}$ (d). Figure adapted from Sterr et al. (2023, Figure 8).

The dependence of the elongational viscosity $\eta_\mathsf{app}(\dot{\gamma}, c_\mathsf{F}, \boldsymbol{d})$ and the suspension viscosity $\underline{\underline{\bar{V}}}(\dot{\gamma}, c_\mathsf{F})$ on the shear rate $\dot{\gamma}$, fiber volume fraction c_F,

and elongation direction $\boldsymbol{d}$ will be omitted for notational clarity. Note that the colormap limits in Figures 3.7 and 3.8 are chosen to highlight the respective extrema of the elongational viscosity η_{app}, and that differences in magnitude are visualized by the size of the viscosity bodies. In Figures 3.7 and 3.8, we observe that for both the Newtonian and Cross-type case, the elongational viscosity η_{app} is large when the direction $\boldsymbol{d}$ is aligned with the principal fiber orientation axis. This is expected, since flow resistance along the cylindrical fibers is higher than in other flow directions. Furthermore, the elongational viscosity η_{app} for both cases increases with growing fiber volume fraction c_{F} in all directions $\boldsymbol{d}$. However, in the Cross-type case, the elongational viscosity η_{app} decreases with the shear rate $\dot{\gamma}$ in all directions $\boldsymbol{d}$. Depending on the value of the shear rate $\dot{\gamma}$, one effect outweighs the other. Note that the minimum value of the elongational viscosity η_{app} does not occur perpendicular to the principal fiber orientation axis x in both cases, because of incompressibility.

3.4.2 Polar representation and material anisotropy

While spatial representations of the elongational viscosity η_{app} provide intuition and qualitative understanding of the underlying viscosity matrix $\underline{\underline{\bar{V}}}$, cuts through the viscosity bodies shown in the previous section allow for a more focused discussion of the occurring effects. As noted in the previous section, the fiber volume fraction c_{F} has a strong influence on the suspension viscosity $\underline{\underline{\bar{V}}}$. Because the matrix $\underline{\underline{\bar{V}}}$ should be transversely isotropic, see section 3.2.5, we will discuss the effect of the fiber volume fraction c_{F} and the shear rate $\dot{\gamma}$ on the suspension viscosity $\underline{\underline{\bar{V}}}$ by focusing on the elongational viscosities η^x_{app} and η^y_{app} in x and y direction. In section 3.4.1 we noted that the elongational viscosity η_{app} increases with the fiber volume fraction c_{F} in all directions $\boldsymbol{d}$. Additionally, as shown in Figures 3.9 and 3.10, the changes of the elongational viscosities η^y_{app} and η^x_{app} with the fiber volume fraction c_{F}

increase with the fiber volume fraction c_F itself. In the Newtonian case, the viscosity η^y_app increases from $530\ \mathrm{Pa\,s}$ to $1581\ \mathrm{Pa\,s}$ as the fiber volume fraction c_F changes from 5% to 25%. In contrast, the elongational viscosity η^x_app increases from $769\ \mathrm{Pa\,s}$ to $3468\ \mathrm{Pa\,s}$ as the fiber volume fraction c_F increases from 5% to 25%. Thus, the elongational viscosities η^y_app and η^x_app increase by 198% and 351%, respectively.

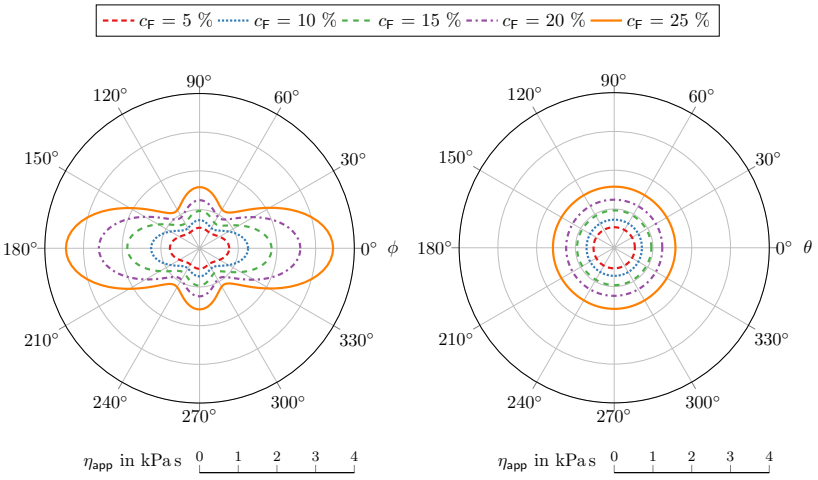

(a) η_app in the x-y plane

(b) η_app y-z plane

Figure 3.9: Apparent viscosity η_app in the x-y and y-z plane, for fiber volume fractions $c_\mathsf{F} \in \{5, 10, 15, 20, 25\}\%$ in the Newtonian case. Figure adapted from Sterr et al. (2023, Figure 9).

c_F in %	5	10	15	20	25
η^y_app in Pa s	530	726	964	1243	1581
η^x_app in Pa s	769	1258	1872	2615	3468

Table 3.2: Apparent viscosities η^y_app and η^x_app in the Newtonian case for fiber volume fractions $c_\mathsf{F} \in \{5, 10, 15, 20, 25\}\%$. Table adapted from Sterr et al. (2023, Table 2).

In the Cross-type case, the elongational viscosity η_{app} depends on the shear rate $\dot{\gamma}$, as highlighted by Figure 3.10 and Table 3.3. At a fiber volume fraction $c_{\mathsf{F}} = 5\%$, the elongational viscosity η^{y}_{app} decreases from 529 Pa s to 30 Pa s as the shear rate $\dot{\gamma}$ changes from $10\,\mathrm{s}^{-1}$ to $10^{5}\,\mathrm{s}^{-1}$.

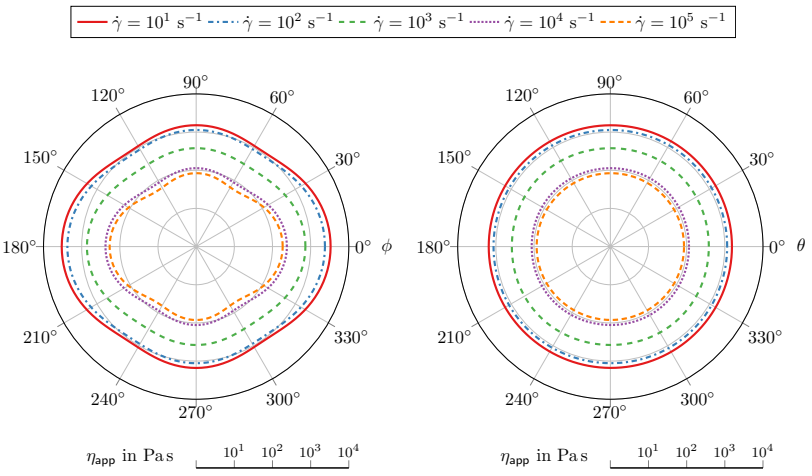

(a) η_{app} in the x-y plane

(b) η_{app} in the y-z plane

Figure 3.10: x-y and y-z plane cuts of the Cross-type, elongational viscosity bodies for fiber volume fractions $c_{\mathsf{F}} = 25\%$ and shear rates $\dot{\gamma} \in \{10^1, 10^2, 10^3, 10^4, 10^5\}\,\mathrm{s}^{-1}$. Figure adapted from Sterr et al. (2023, Figure 10).

c_{F} in %	5			15			25		
$\dot{\gamma}$ in s^{-1}	10^1	10^3	10^5	10^1	10^3	10^5	10^1	10^3	10^5
η^{y}_{app} in Pa s	529	226	30	939	295	52	1515	379	84
η^{x}_{app} in Pa s	759	287	43	1818	494	101	3336	729	185

Table 3.3: Apparent viscosities η^{y}_{app} and η^{x}_{app} in the Cross-type case for fiber volume fractions $c_{\mathsf{F}} \in \{5, 10, 15, 20, 25\}\%$ and shear rates $\dot{\gamma} \in \{10, 10^3, 10^5\}\,\mathrm{s}^{-1}$. Table adapted from Sterr et al. (2023, Table 3).

In contrast, the elongational viscosity η^x_{app} decreases from $759\,\mathrm{Pa\,s}$ to $43\,\mathrm{Pa\,s}$ as the shear rate $\dot\gamma$ changes from $10\,\mathrm{s}^{-1}$ to $10^5\,\mathrm{s}^{-1}$. Hence, both elongational viscosities η^y_{app} and η^x_{app} decrease by the same factor of around 94%. However, for a lower shear rate $\dot\gamma = 10^3\,\mathrm{Pa\,s}$, the elongational viscosities η^y_{app} and η^x_{app} decrease differently by the factors 57% and 62%, respectively. We observe a similar change for the higher fiber volume fraction $c_{\mathsf{F}} = 25\%$. In this case, the elongational viscosities η^y_{app} and η^x_{app} also decrease by around 94% as the shear rate $\dot\gamma$ changes from $10\,\mathrm{s}^{-1}$ to $10^5\,\mathrm{s}^{-1}$. Again, for a lower shear rate $\dot\gamma = 10^3\,\mathrm{Pa\,s}$, the elongational viscosities η^y_{app} and η^x_{app} decrease differently by the factors 75% and 78%, respectively. As a result, we conclude that for shear rates $\dot\gamma$ where the matrix behavior is non-Newtonian the elongational viscosities η^x_{app} and η^y_{app} vary stronger with the shear rate for higher fiber volume fraction c_{F}. Also, since the elongational viscosities η^y_{app} and η^x_{app} change by different factors in both the Newtonian and Cross-type case for a shear rate $\dot\gamma = 10^3\,\mathrm{s}^{-1}$, the material anisotropy changes with varying fiber volume fraction c_{F} and shear rate $\dot\gamma$, see Figure 3.11. We discuss these changes in the following.

For the transversely isotropic symmetry of the suspension viscosity $\underline{\underline{\bar{V}}}$, its anisotropy is characterized by the elongational viscosities η^x_{app} and η^y_{app}. For further investigation we also use a third elongational viscosity η^z_{app} in z direction. Each parameter represents the value of the elongational viscosity η_{app} for an elongation direction $\boldsymbol{d}$ in x-, y-, and z-direction, respectively. Thus, the fractions

$$f_1 = \frac{\eta^x_{\mathsf{app}}}{\eta^y_{\mathsf{app}}}, \quad \text{and} \quad f_2 = \frac{\eta^x_{\mathsf{app}}}{\eta^z_{\mathsf{app}}} \tag{3.55}$$

serve as a measure of directional anisotropy. For a theoretical, perfectly transversely isotropic suspension viscosity, both fractions f_1 and f_2 assume the same value. As described in section 3.2.5, we prescribed a transversely isotropic, second order orientation tensor (3.45) for all con-

sidered microstructures. Hence, we also expect a transversely isotropic suspension viscosity $\underline{\underline{\bar{V}}}$ if the volume element size for the computational investigations was chosen sufficiently large.

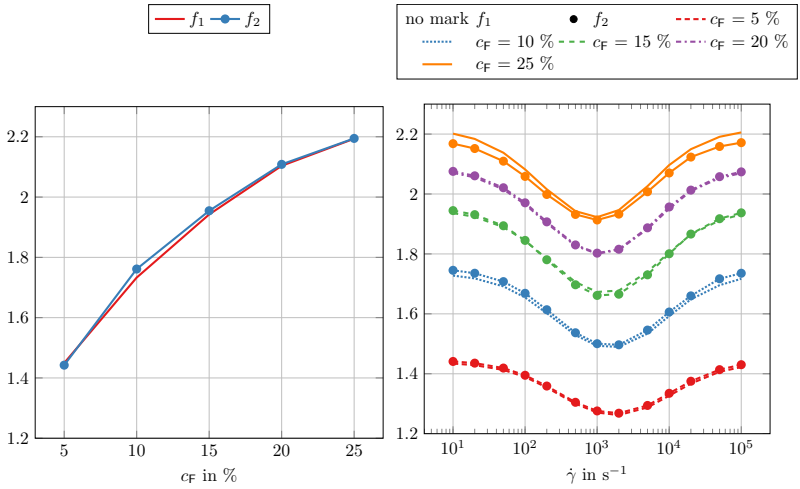

(a) f_1 and f_2 for the Newtonian case **(b)** f_1 and f_2 for the Cross-type case

Figure 3.11: Anisotropy fractions f_1 and f_2 (3.55) for the Newtonian and the Cross-type case, $c_F \in \{5, 10, 15, 20, 25\}\%$, $\dot{\gamma} \in [10, 10^5]\,\mathrm{s}^{-1}$. Figure adapted from Sterr et al. (2023, Figure 11).

To test if the volume element size was chosen appropriately, we define the relative deviation

$$e_{\mathrm{dev}} = \frac{|f_1 - f_2|}{|f_1|}, \tag{3.56}$$

and evaluate the relative deviation e_{dev} for both the Newtonian and Cross-type case. For all considered shear rates $\dot{\gamma}$ and volume fractions c_F, the deviation e_{dev} is smaller than 2% in both the Newtonian and the Cross-type case. Therefore, the values of the fractions f_1 and f_2 differ only slightly from each other, and the expected symmetry of the material is captured with an error that is sufficiently small for engineering

purposes. The elongational viscosity η_{app} in the y-z plane, as shown in Figures 3.9b and 3.10b, illustrate the material symmetry further, since the polar plots of the elongational viscosity η_{app} are circular for all fiber volume fractions c_{F} and shear rates $\dot{\gamma}$. Since we consider the volume elements as representative, we will discuss the dependence of both fractions f_1 and f_2 on the fiber volume fraction c_{F} and the shear rate $\dot{\gamma}$ as shown in Figure 3.11.

In the Newtonian case, both fractions f_1 and f_2 grow significantly from 1.45 at a volume fraction $c_{\mathsf{F}} = 5\%$ to 2.19 at a volume fraction $c_{\mathsf{F}} = 25\%$. Because the matrix behavior in the Cross-type case is approximately Newtonian for low shear rates $\dot{\gamma}$, the values of the fractions f_1 and f_2 in the Cross-type case for a shear rate $\dot{\gamma} = 10\,\mathrm{s}^{-1}$ are similar to those in the Newtonian case. As the shear rate $\dot{\gamma}$ grows, the values of the fractions f_1 and f_2 decrease up to a shear rate $\dot{\gamma}_{\mathsf{min}} \approx 10^3\,\mathrm{s}^{-1}$, where they reach their respective minima. Because more fibers are likely to be packed close to each other for higher volume fractions c_{F}, higher velocity gradients occur at lower macroscopic shear rates $\dot{\gamma}$. This, in turn, decreases the local matrix viscosity. Consequently, the minimum of the fractions f_1 and f_2 occurs at lower shear rates as the fiber volume fraction grows. For a fiber volume fraction $c_{\mathsf{F}} = 25\%$, the minimum of the fractions f_1 and f_2 is attained at a shear rate $\dot{\gamma} = 10^3\,\mathrm{s}^{-1}$, whereas, for a fiber volume fraction $c_{\mathsf{F}} = 5\%$, the minimum is attained at a shear rate $\dot{\gamma} = 2 \cdot 10^3\,\mathrm{s}^{-1}$. Also, the maximum absolute changes

$$\Delta f(c_{\mathsf{F}}) = f(c_{\mathsf{F}}, 10\,\mathrm{s}^{-1}) - f(c_{\mathsf{F}}, \dot{\gamma}_{\mathsf{min}}) \tag{3.57}$$

increase with the fiber volume fraction c_{F}, e.g., $\Delta f(c_{\mathsf{F}}) = 17\%$ and $\Delta f(c_{\mathsf{F}}) = 28\%$ for fiber volume fractions c_{F} of 5% and 25%, respectively. In contrast, the maximum relative changes

$$\Delta f(c_{\mathsf{F}}) = \frac{f(c_{\mathsf{F}}, 10\,\mathrm{s}^{-1}) - f(c_{\mathsf{F}}, \dot{\gamma}_{\mathsf{min}})}{f(c_{\mathsf{F}}, 10\,\mathrm{s}^{-1})} \tag{3.58}$$

lie between 12% to 14% for all investigated fiber volume fractions.

3.4.3 Comparison to mean-field results

In the following, we compare the computational results with mean-field estimates. In the Newtonian and Cross-type cases, we use the Mori-Tanaka model (3.40) to calculate the apparent mean-field viscosity $\eta_{\mathsf{app}}^{\mathsf{MF}}$. Then, we compare the apparent mean-field viscosity $\eta_{\mathsf{app}}^{\mathsf{MF}}$ with the apparent computational viscosity $\eta_{\mathsf{app}}^{\mathsf{FFT}}$ via the deviation

$$e_{\mathsf{MF}} = \frac{\left|\eta_{\mathsf{app}}^{\mathsf{MF}} - \eta_{\mathsf{app}}^{\mathsf{FFT}}\right|}{\eta_{\mathsf{app}}^{\mathsf{FFT}}}. \tag{3.59}$$

To reduce dimensional complexity, and to avoid compromising the comparison with potential interpolation errors, as discussed in section 3.4.1, we focus our discussion on the two scalar quantities η_{app}^{x} and η_{app}^{y}. The results for the Newtonian and the Cross-type case are shown in Figures 3.12 and 3.13, as well as Figure 3.14. In the Newtonian case, the elongational viscosities η_{app}^{x} and η_{app}^{y} obtained via the mean-field method are lower than the ones obtained via the FFT-based computational method. Also, for a fiber volume fraction $c_{\mathsf{F}} = 5\%$, the mean-field and FFT-based results for η_{app}^{x} and η_{app}^{y} can still be considered similar for engineering purposes, as the deviation e_{MF} is below 5.7%. However, for increasing fiber volume fractions c_{F}, the deviation e_{MF} increases monotonically up to 26.8% for the elongational viscosity η_{app}^{x} and 23.5% for the elongational viscosity η_{app}^{y}.

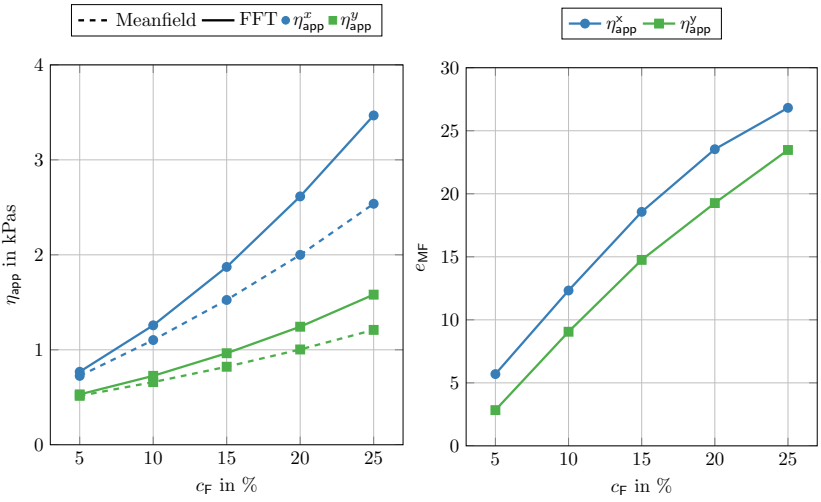

(a) Apparent viscosities η^x_{app} and η^y_{app} **(b)** Deviation e_{MF}

Figure 3.12: Apparent viscosities η^x_{app} and η^y_{app} for the mean-field model and the FFT-based computational method, and deviation e_{MF} (3.56) for fiber volume fractions $c_{\mathsf{F}} \in \{5, 10, 15, 20, 25\}\%$ in the Newtonian case. Figure adapted from Sterr et al. (2023, Figure 12).

In the Cross-type case, for shear rates $\dot{\gamma} \approx 10\,\mathrm{s}^{-1}, \dot{\gamma} \approx 10^5\,\mathrm{s}^{-1}$, we observe the same results for the deviation e_{MF} as in the Newtonian case. This is a direct result of the two Newtonian regions of the Cross-type matrix viscosity η at the shear rate limits $\dot{\gamma} \to 0\,\mathrm{s}^{-1}$ and $\dot{\gamma} \to \infty\,\mathrm{s}^{-1}$. The largest deviation e_{MF} occurs for a shear rate $\dot{\gamma} = 10^3\,\mathrm{s}^{-1}$, where the matrix nonlinearity is highest. As we already observed for the anisotropy measures f_1 and f_2 in section 3.4.1, the fiber volume fraction c_{F} influences the shear rate $\dot{\gamma}$ at which the maximum deviation e_{MF} occurs. In particular, for both elongational viscosities η^x_{app} and η^y_{app}, the maximum observed deviation for a fiber volume fraction $c_{\mathsf{F}} = 25\%$ occurs at a lower shear rate $\dot{\gamma} = 10^3\,\mathrm{s}^{-1}$, whereas it occurs at a shear rate

$\dot{\gamma} = 2 \cdot 10^3\,\mathrm{s}^{-1}$ for a fiber volume fraction $c_\mathsf{F} = 5\%$.

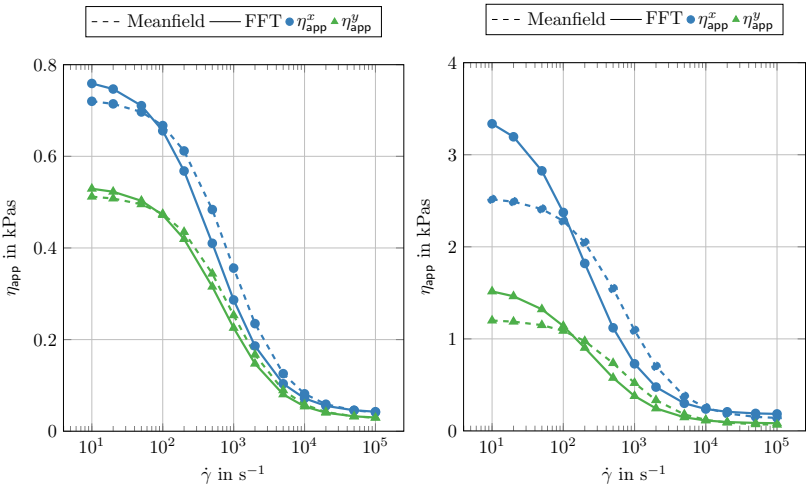

(a) $c_\mathsf{F} = 5\%$ **(b)** $c_\mathsf{F} = 25\%$

Figure 3.13: Apparent viscosities η^x_{app} and η^y_{app} for the mean-field model and the FFT-based computational method for fiber volume fractions $c_\mathsf{F} \in \{5, 25\}\%$ and shear rates $\dot{\gamma} \in [10, 10^5]\,\mathrm{s}^{-1}$ in the Cross-type case. Figure adapted from Sterr et al. (2023, Figure 13).

As an additional consequence of the Cross-type material law (3.2), the curves of the elongational viscosities η^x_{app} and η^y_{app} for the two calculation methods intersect twice. For the fiber volume fractions $c_\mathsf{F} = 5\%$ and $c_\mathsf{F} = 25\%$, the first intersection occurs at shear rates $\dot{\gamma} \approx 10^2\,\mathrm{s}^{-1}$ while the second intersection occurs in the shear rate interval $[10^4, 5 \cdot 10^4]\,\mathrm{s}^{-1}$, depending on the fiber volume fraction c_F. For higher fiber volume fractions c_F the second intersection occurs at lower macroscopic shear rates $\dot{\gamma}$, because the decreased fiber to fiber distance leads to higher microscopic shear rates. Consequently, we observe an earlier transition into the second Newtonian regime at the shear

rate limit $\dot{\gamma} \to \infty\,\mathrm{s}^{-1}$. In between the intersections of the elongational viscosity curves, the elongational viscosity η_{app} obtained via the mean-field model is higher than for the computational approach.

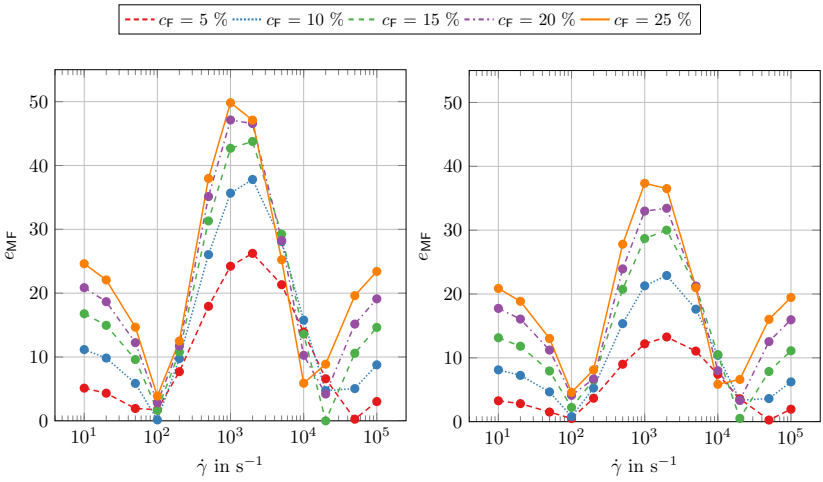

(a) e_{MF} of η^{x}_{app} **(b)** e_{MF} of η^{y}_{app}

Figure 3.14: Deviation e_{MF} (3.56) of the elongational viscosities η^{x}_{app} and η^{y}_{app} for fiber volume fractions $c_{\mathsf{F}} \in \{5, 10, 15, 20, 25\}\%$ and shear rates $\dot{\gamma} \in [10, 10^5]\,\mathrm{s}^{-1}$ in the Cross-type case. Figure adapted from Sterr et al. (2023, Figure 14).

3.5 Conclusions

This chapter was devoted to study the effect of shear-thinning matrix behavior on the effective viscosity of fiber suspensions. We focused our considerations on shear rates of interest for engineering manufacturing processes, like injection and compression molding. For our investigations, we made use of a Cross-type viscosity model and an

FFT-based computational method to determine the effective viscosity of fiber suspensions over a wide range of shear rates. We found the resolution error of the microstructure discretization to be dependent on the shear rate and load direction, with the minimum resolution error occurring at medium shear rates and pure shear loads. To our surprise, we found the representative volume element size to be highly similar in a Newtonian case with aligned microstructure and a Cross-type case with transversely isotropic microstructure. Over the considered shear rate interval, we found the Cross-type suspension viscosity to vary strongly in magnitude and in degree of anisotropy. Finally, we observed substantial deviations between the computational estimates and Mori-Tanaka type mean-field estimates for the suspension viscosity.

Chapter 4

Machine learning assisted discovery of effective viscous material laws for shear-thinning fiber suspensions[1]

4.1 Introduction

Viscosity models for fiber polymer suspensions are widely used in molding process simulations of composite parts (Kennedy and Zheng, 2013), which play a major role in the lightweight design of engineering systems, i.e., in the automotive, aerospace, and energy sectors (Henning et al., 2019; Qureshi, 2022). Molding process simulations are an established tool in composite part engineering, partly because of the industrial benefits of digital twins (Botín-Sanabria et al., 2022) and virtual process chains (Henning et al., 2019; Görthofer et al., 2019; Meyer et al., 2023). In molding simulations for fiber reinforced plastics, accurate modeling of the suspension viscosity is crucial to predict various parameters of engineering interest. The suspension viscosity influences manufacturing process parameters (Castro and Tomlinson, 1990; Goodship, 2017), as

[1] This chapter is based on the sections 1 to 5 of the publication "Machine learning assisted discovery of effective viscous material laws for shear-thinning fiber suspensions" (Sterr et al., 2024b).

well as fiber orientation and fiber volume distributions (Tseng et al., 2018). Consequently, flow fields (Karl et al., 2021) and final part properties (Böhlke et al., 2019; Karl et al., 2021) are also affected by the suspension viscosity. In light of the analytical and experimental difficulties involved when studying the viscosity of fiber suspensions with non-Newtonian solvents, computational approaches provide insights and observations that are otherwise hard to obtain. Švec et al. (2012) combined the lattice Boltzmann method for fluid flow, an immersed boundary procedure for the interaction between fluid and rigid particles, and a mass tracking algorithm for the free surface representation to simulate slump tests of a suspension of rigid spherical particles and fibers suspended in a Bingham-type fluid. In comparison with a slump test of pure matrix material, they observed a smaller spread and increased height in the slump test of the suspension, suggesting an increased effective yield stress. Using a Finite Element Method (FEM) based approach, Domurath et al. (2020) investigated the rheological coefficients of the transversely isotropic fluid equation by Ericksen (1960) in the context of rigid fibers suspended in a power-law fluid. In a simple shear flow, they found the model by Souloumiac and Vincent (1998) to overpredict the orientation dependence of a rheological coefficient. Combining the RVE method (Kanit et al., 2003) and Fast Fourier Transform (FFT) based computational techniques (Schneider, 2021), Sterr et al. (2023) extended work by Bertóti et al. (2021) on Newtonian fiber suspensions to suspensions with non-Newtonian solvents. They visualized the anisotropic viscosity tensor in the case of a Cross-type matrix fluid and studied the effects of fiber volume fraction and shear rate on the suspension viscosity.

In this chapter, we combine high fidelity, FFT-based computational methods and a supervised machine learning strategy to discover material models for the effective viscosity of shear-thinning fiber suspensions. To do so, we study the anisotropic and shear rate dependent effective

viscosity of fiber suspensions with a Cross-type matrix behavior and a fiber volume fraction of 25%. In section 4.2 we outline the setup for the FFT-based computational investigations, where we compute the effective material response for 109 different fiber orientation states and a variety of loading states. In terms of computational scope, this constitutes a significant extension to previous FFT-based work on shear-thinning fiber suspensions, in which a single fiber orientation state was considered (Sterr et al., 2023). Based on the computational data, we visualize the suspension viscosity tensor in three dimensions and formulate an anisotropy criterion applicable in a non-linear setting using a loading direction and shear rate dependent scalar viscosity, see section 4.3. We find that the anisotropy of the suspension viscosity shows a significantly different shear rate dependence for different fiber orientation states. Also, for all investigated microstructures, we confirm that the anisotropy of the suspension viscosity depends on the degree of non-linearity of the matrix material, which was previously only studied for a transversely isotropic microstructure (Sterr et al., 2023). In section 4.4, based on the insights into the shear rate and orientation state dependence of the suspension viscosity, we formulate requirements a model of the suspension viscosity needs to fulfill. According to the formulated requirements we propose four models with different numbers of parameters, as well as different phenomenological and theoretical motivations. Using the ADAM algorithm, we employ supervised machine learning techniques for non-convex optimization to learn the parameters of the model candidates. Overall, three models achieve similar maximum validation errors below 5.15 %, while one model based on superposition and orientation averaging performs unfavorably.

4.2 A computational study of the effective behavior of shear-thinning fiber suspensions

4.2.1 Computational homogenization procedure

In this chapter, we consider incompressible, shear-thinning fiber suspensions, occupying a rectangular volume $Y \subseteq \mathbb{R}^3$. First, we give a short summary of the numerical procedure for the homogenization of shear-thinning fiber suspensions detailed in section 3.2. We are interested in computing the effective viscous stress $\bar{\boldsymbol{\tau}} \in \mathsf{Sym}_0(3)$ of the suspension in response to an applied, effective shear rate tensor $\bar{\boldsymbol{D}} \in \mathsf{Sym}_0(3)$, where $\mathsf{Sym}_0(3)$ denotes the vector space of symmetric and traceless second-order tensors. For a pressure field $p : Y \to \mathbb{R}$, a solenoidal velocity field $\boldsymbol{v} : Y \to \mathbb{R}^3$ and a local viscous stress field

$$\boldsymbol{\tau} = \mathcal{T}(\cdot, \bar{\boldsymbol{D}} + \nabla^{\mathsf{s}} \boldsymbol{v}), \tag{4.1}$$

with associated stress operator

$$\mathcal{T} : Y \times \mathsf{Sym}_0(3) \to \mathsf{Sym}_0(3), \tag{4.2}$$

$$(\boldsymbol{x}, \boldsymbol{D}) \mapsto \frac{\partial \Psi}{\partial \boldsymbol{D}}(\boldsymbol{x}, \boldsymbol{D}), \tag{4.3}$$

and dissipation potential $\Psi : Y \times \mathsf{Sym}_0(3) \to \mathbb{R}$, the local balance of linear momentum without inertial effects

$$\operatorname{div}(\boldsymbol{\tau}) - \nabla p = \boldsymbol{0}, \tag{4.4}$$

needs to be fulfilled. In the context of suspensions with rigid inclusions, the local viscous stress $\boldsymbol{\tau}$ in equation (4.4) is, constitutively, not well-defined inside the rigid inclusions. We address this issue by changing to a dual formulation as follows. With the complementary dissipation

potential

$$\Phi(\boldsymbol{\tau}) := \sup\left\{\boldsymbol{\tau}\cdot\boldsymbol{D} - \Psi(\boldsymbol{D}) \,|\, \boldsymbol{D}\in \mathsf{Sym}_0(3)\right\}, \tag{4.5}$$

arising as the Legendre–Fenchel dual of the dissipation potential Ψ, we search for minimizers of the variational problem

$$\left\langle \Phi(\cdot,\boldsymbol{\tau}) - \boldsymbol{\tau}\cdot\bar{\boldsymbol{D}}\right\rangle_Y \longrightarrow \inf\,. \tag{4.6}$$

Here, $\langle\cdot\rangle_Y$ denotes the spatial average

$$\langle\cdot\rangle_Y \equiv \frac{1}{|Y|}\int_Y (\cdot)\,\mathrm{d}Y(\boldsymbol{x}) \quad \text{with} \quad |Y| \equiv \int_Y \mathrm{d}Y(\boldsymbol{x}), \tag{4.7}$$

and the infimum is taken over all stress fields $\boldsymbol{\tau}$ satisfying the equilibrium equation (4.4). Minimizers of the variational problem (4.6) satisfy the Euler–Lagrange equation

$$\mathbb{P}_{\mathcal{E}}\left[\frac{\partial\Phi}{\partial\boldsymbol{\tau}}(\boldsymbol{\tau}_k) - \bar{\boldsymbol{D}}\right] = \boldsymbol{0}, \tag{4.8}$$

where $\mathbb{P}_{\mathcal{E}}$ refers to the L^2-projector onto the shear stresses satisfying the equilibrium equation (4.4). We refer to Bertóti et al. (2021, §2) for a closed form expression of the action of $\mathbb{P}_{\mathcal{E}}$ in Fourier space. In case of suspensions with rigid particles the shear rate tensor $\boldsymbol{D}$ and hence the derivative $\partial\Phi/\partial\boldsymbol{\tau}$ vanishes inside the particles. Thus, the formulation of the optimization problem (4.6) in terms of the complementary dissipation potential Φ is advantageous for numerical schemes based on the Euler–Lagrange equation (4.8). If the optimization problem (4.6) is convex, a minimizer can be found with, e.g., gradient descent (Sterr et al., 2023), the Barzilai–Borwein method (Barzilai and Borwein, 1988), or Newton-CG (Dembo et al., 1982; Schneider, 2020a) approaches. Finally, the effective viscous stress $\bar{\boldsymbol{\tau}}$ can be computed by spatial averaging, such that

$$\bar{\boldsymbol{\tau}} = \langle\boldsymbol{\tau}\rangle_Y\,. \tag{4.9}$$

4.2.2 Computational study setup and material parameters

To study the material response of shear-thinning fiber suspensions with a variety of microstructures, we generated fiber suspension microstructures for 109 points of the fiber orientation triangle S_T (2.37), see Figs. 4.1a and 4.2, using the sequential addition and migration method (Schneider, 2017). Following Köbler et al. (2018), we use a CMYK coloring scheme to visualize the fiber orientation state within the fiber orientation triangle S_T. The isotropic, unidirectional, and planar isotropic orientation states represent the corners of the fiber orientation triangle and are colored cyan, magenta, and yellow, respectively. Building upon the investigations in Sterr et al. (2023), a commercially available polyamide 6 (BASF, 2020) was chosen as the matrix material, and a Cross-type material law (3.2) was fitted to the available material data for shear rates $\dot{\gamma}$ in the interval $[1.7, 16300]\,\mathrm{s}^{-1}$ at a temperature of $250°\mathrm{C}$. The resulting model parameters are collected in Table 4.1, and equal the parameters presented in section 3.2.1.

η_0	η_∞	k	m
288.9 Pa s	15.0 Pa s	$10.9 \cdot 10^{-4}$	1.1

Table 4.1: Parameters of the Cross-type material law (3.2) for a commercially available polyamide 6 (BASF, 2020). Table adapted from Sterr et al. (2024b, Table 1).

The viscosities η_0 and η_∞ define the material behavior for shear rates $\dot{\gamma} = 0$ and $\dot{\gamma} \to \infty$, respectively, while the parameters k and m control the non-linear transition between the viscosities η_0 and η_∞. The suspension microstructures were discretized on a staggered grid (Harlow and Welch, 1965) using composite voxels (Kabel et al., 2017) with a general dual mixing rule for the special case of rigid particles (Sterr et al., 2023). The resulting non-linear system of equations was solved with a Newton-CG

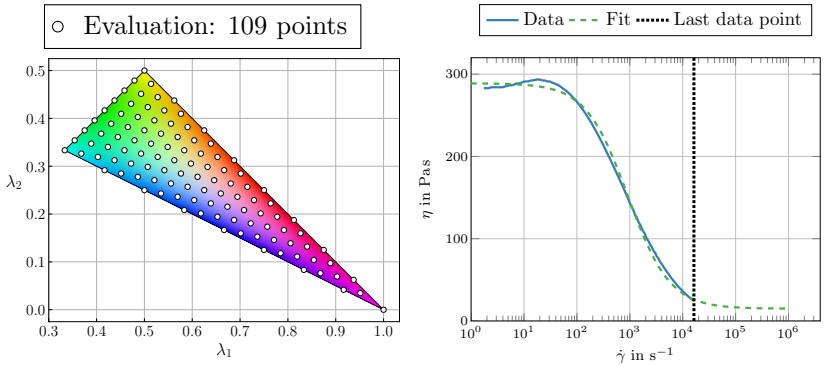

(a) Fiber orientation triangle S_{T} **(b)** Cross-type fit

Figure 4.1: Fiber orientation triangle S_{T} in CMYK coloring with 109 evaluation points (a), and material data with Cross-type fit for Ultramid®B3K (b). Figure adapted from Sterr et al. (2024b, Figure 1).

approach. To limit the required computational effort, we restricted to microstructures with a fiber volume fraction $c_{\mathsf{F}} = 25\%$, where all fibers have equal length ℓ and diameter d. More precisely, we prescribed an aspect ratio $r_{\mathsf{a}} = \ell/d$ of 10. The resolutions and sizes of the microstructure volume elements were chosen according to the investigations in Sterr et al. (2023), such that the number of voxels per fiber diameter is $v/d = 15$ and the edge length of the cubic volume elements is $L = 2.2\ell$.

Furthermore, we consider the same flow scenarios as in the previous chapter 3. More specifically, for each macroscopic scalar shear rate $\dot{\gamma}$ in the set of studied shear rates $S_{\dot{\gamma}}$ (3.44) we investigate the six load cases collected in the matrix $\bar{\bar{D}}$ (3.35). The set of studied shear rates $S_{\dot{\gamma}}$ is intended to cover a broad variety of engineering process shear rates, and is motivated by the typical shear rates in compression molding, standard injection molding, as well as thin-wall and micro molding (Valero, 2020; Friesenbichler et al., 2011). For shear rates $\dot{\gamma}$, where the matrix behavior is mostly Newtonian and the superposition of material responses is valid, we compute and collect the components of the effective viscosity

tensor $\bar{\mathbb{V}}$ in a matrix $\underline{\underline{\bar{V}}}$ with

$$\underline{\underline{\bar{\tau}}} = \underline{\underline{\bar{V}}}\,\underline{\underline{\bar{D}}}, \quad \text{i.e.,} \quad \underline{\underline{\bar{V}}} = \underline{\underline{\bar{\tau}}}\,\underline{\underline{\bar{D}}}^{\dagger}. \tag{4.10}$$

Here, $(\cdot)^{\dagger}$ stands for the Moore–Penrose pseudoinverse, and $\underline{\underline{\bar{\tau}}}$ collects the computed effective stresses

$$\underline{\underline{\bar{\tau}}} = \begin{bmatrix} \bar{\tau}_{11}^{(1)} & \bar{\tau}_{11}^{(2)} & \bar{\tau}_{11}^{(3)} & \bar{\tau}_{11}^{(4)} & \bar{\tau}_{11}^{(5)} & \bar{\tau}_{11}^{(6)} \\ \bar{\tau}_{22}^{(1)} & \bar{\tau}_{22}^{(2)} & \bar{\tau}_{22}^{(3)} & \bar{\tau}_{22}^{(4)} & \bar{\tau}_{22}^{(5)} & \bar{\tau}_{22}^{(6)} \\ \bar{\tau}_{33}^{(1)} & \bar{\tau}_{33}^{(2)} & \bar{\tau}_{33}^{(3)} & \bar{\tau}_{33}^{(4)} & \bar{\tau}_{33}^{(5)} & \bar{\tau}_{33}^{(6)} \\ \sqrt{2}\bar{\tau}_{23}^{(1)} & \sqrt{2}\bar{\tau}_{23}^{(2)} & \sqrt{2}\bar{\tau}_{23}^{(3)} & \sqrt{2}\bar{\tau}_{23}^{(4)} & \sqrt{2}\bar{\tau}_{23}^{(5)} & \sqrt{2}\bar{\tau}_{23}^{(6)} \\ \sqrt{2}\bar{\tau}_{13}^{(1)} & \sqrt{2}\bar{\tau}_{13}^{(2)} & \sqrt{2}\bar{\tau}_{13}^{(3)} & \sqrt{2}\bar{\tau}_{13}^{(4)} & \sqrt{2}\bar{\tau}_{13}^{(5)} & \sqrt{2}\bar{\tau}_{13}^{(6)} \\ \sqrt{2}\bar{\tau}_{12}^{(1)} & \sqrt{2}\bar{\tau}_{12}^{(2)} & \sqrt{2}\bar{\tau}_{12}^{(3)} & \sqrt{2}\bar{\tau}_{12}^{(4)} & \sqrt{2}\bar{\tau}_{12}^{(5)} & \sqrt{2}\bar{\tau}_{12}^{(6)} \end{bmatrix}. \tag{4.11}$$

4.3 Spatial representation and anisotropy of the effective suspension viscosity

With the goal of modeling the effective behavior of shear-thinning fiber suspensions in mind, it is essential to understand the anisotropic effective viscosity of such suspensions, as well as its dependence on the fiber orientation state $\underline{\lambda}$ and the shear rate $\dot{\gamma}$ first. Accordingly, we begin by visualizing the effective viscosity and studying its anisotropy for low shear rates $\dot{\gamma}$ in the following, before studying the effects of non-linear shear-thinning. To reduce the dimensional complexity when studying the effective viscosity, we use a scalar elongational viscosity η_{app}. Following Sterr et al. (2023, §4), we define the viscosity η_{app} based on a modified approach by Böhlke and Brüggemann (2001), such that

$$\eta_{\mathsf{app}}(\dot{\gamma}, \underline{\lambda}, \boldsymbol{d}) = \bar{\mathbb{V}}(\dot{\gamma}, \underline{\lambda}) \cdot (\boldsymbol{d} \otimes \boldsymbol{d} \otimes \boldsymbol{d} \otimes \boldsymbol{d}), \tag{4.12}$$

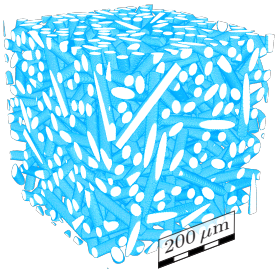

(a) $\lambda_1 = 0.\overline{33}, \lambda_2 = 0.\overline{33}$

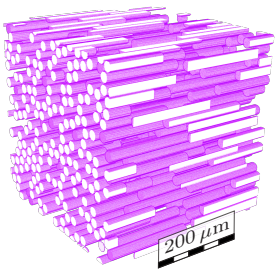

(b) $\lambda_1 = 1, \lambda_2 = 0$

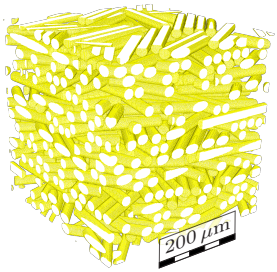

(c) $\lambda_1 = 0.5, \lambda_2 = 0.5$

Figure 4.2: Investigated microstructures for isotropic (a), unidirectional (b), and planar isotropic (c) fiber orientation states. Figure adapted from Sterr et al. (2024b, Figure 2).

where $\boldsymbol{d} \in S^2$ denotes the direction of elongation, $\underline{\lambda} \in S_\mathsf{T}$ refers to the fiber orientation state, and S_T is the fiber orientation triangle defined in equation (2.37). We use equation (4.10) to approximate the effective viscosity $\bar{\mathbb{V}}$ and thus the elongational viscosity η_{app} with

$$\eta_{\mathsf{app}}(\dot{\gamma}, \underline{\lambda}, \boldsymbol{d}) \approx \underline{a}(\boldsymbol{d})^\mathsf{T} \underline{\bar{V}}(\dot{\gamma}, \underline{\lambda})\, \underline{a}(\boldsymbol{d}), \tag{4.13}$$

where $\underline{a}(\boldsymbol{d})$ denotes the components of $\boldsymbol{d} \otimes \boldsymbol{d}$ in Mandel notation. In addition to the elongational viscosity η_{app}, the bulk viscosity

$$\eta_{\mathsf{b}}(\dot{\gamma}, \underline{\lambda}, \boldsymbol{d}) = \boldsymbol{I} \cdot \bar{\mathbb{V}}(\dot{\gamma}, \underline{\lambda})(\boldsymbol{d} \otimes \boldsymbol{d}) = (\boldsymbol{d} \otimes \boldsymbol{d}) \cdot \bar{\mathbb{V}}[\boldsymbol{I}], \tag{4.14}$$

is required to capture all information contained in the effective viscosity $\bar{\mathbb{V}}$ (He and Curnier, 1995, Sec. 4.3) if the effective material is compressible. However, as we consider incompressible material behavior, the bulk viscosity η_b vanishes, since

$$\bar{\mathbb{V}}[\boldsymbol{I}] = 0. \tag{4.15}$$

Hence, the elongational viscosity η_app encodes all information contained in the matrix $\underline{\underline{\bar{V}}}(\dot{\gamma}, \underline{\lambda})$, and allows us to study the anisotropic flow resistance of the suspension in a complete manner. For the elongational viscosity and related quantities we omit denoting the dependence on the shear rate $\dot{\gamma}$, the fiber orientation state $\underline{\lambda}$, and the direction of elongation $\boldsymbol{d}$ explicitly. Because of the interpolating property of equation (4.10), we may visualize the direction-dependent material behavior for load cases not collected in $\underline{\underline{\bar{D}}}$, and develop intuition for the influence of different fiber orientation states on the elongational viscosity η_app. For a discussion on the applicability of equation (4.10) in the case of non-linear material behavior, we Sterr et al. (2023, §2.3, §4). For the visualization of the elongational viscosity η_app, we restrict to a shear rate $\dot{\gamma} = 10\,\mathrm{s}^{-1}$, where the material behavior is mostly linear and the superposition principle encoded in equation (4.10) holds. The elongational viscosity bodies for the isotropic, the planar isotropic, the transversely isotropic, and the unidirectional fiber orientation states are visualized in Figure 4.3 for a shear rate $\dot{\gamma} = 10\ \mathrm{s}^{-1}$. To study the suspension anisotropy at the same shear rate $\dot{\gamma} = 10\,\mathrm{s}^{-1}$, for each orientation state and over all directions $\boldsymbol{d}$, we compute the range $\Delta\eta_\mathsf{app}$ and the ratio r_app

$$\Delta\eta_\mathsf{app} = \max(\eta_\mathsf{app}) - \min(\eta_\mathsf{app}), \quad r_\mathsf{app} = \frac{\max(\eta_\mathsf{app})}{\min(\eta_\mathsf{app})}, \tag{4.16}$$

and collect the results in Table 4.2.

For the isotropic state, the elongational viscosity η_app lies between 1513 $\mathrm{Pa\,s}$ to 1576 $\mathrm{Pa\,s}$, resulting in a range $\Delta\eta_\mathsf{app} = 63\,\mathrm{Pa\,s}$ and a

ratio $r_{\mathsf{app}} = 1.04$. Because there is no principal fiber orientation axis in the isotropic state, the maximum viscosity η_{app}, the range $\Delta\eta_{\mathsf{app}}$, and the ratio r_{app} are lower than in the more strongly oriented states, see Figure 4.3a. In contrast, the maxima of the elongational viscosity η_{app} occur in the principal fiber orientation axes clearly visible in Figures 4.3b to 4.3d. For the planar isotropic state, the maximum of the elongational viscosity η_{app} occurs in the x-y plane with 1947 $\mathrm{Pa\,s}$, and for the transversely isotropic and unidirectional cases, the maxima occur in the x direction with 2973 $\mathrm{Pa\,s}$ and 4845 $\mathrm{Pa\,s}$, respectively. Also, with increasing degree of orientation, the range $\Delta\eta_{\mathsf{app}}$ and ratio r_{app} grow from 977 $\mathrm{Pa\,s}$ and 2.01 in the planar isotropic state, 1810 $\mathrm{Pa\,s}$ and 2.56 in the transversely isotropic state, and up to 4130 $\mathrm{Pa\,s}$ and 6.78 in the unidirectional state. The strong dependence of the maximum elongational viscosity, the range $\Delta\eta_{\mathsf{app}}$, and the ratio r_{app} on the orientation state highlights the influence of the fibers on the anisotropy and magnitude of the effective viscous material behavior. Furthermore, the location and magnitude of the minimum elongational viscosity η_{app} depend on the orientation state as well.

	Iso	Piso	Tiso	UD
$\Delta\eta_{\mathsf{app}}$	63	977	1810	4130
r_{app}	1.04	2.01	2.56	6.78

Table 4.2: Range $\Delta\eta_{\mathsf{app}}$ (4.16) and ratio r_{app} (4.16) of the elongational viscosity η_{app} at a shear rate $\dot{\gamma} = 10\ \mathrm{s}^{-1}$ for isotropic (Iso), planar isotropic (Piso), transversely isotropic (Tiso), and unidirectional (UD) fiber orientation states. Table adapted from Sterr et al. (2024b, Table 2).

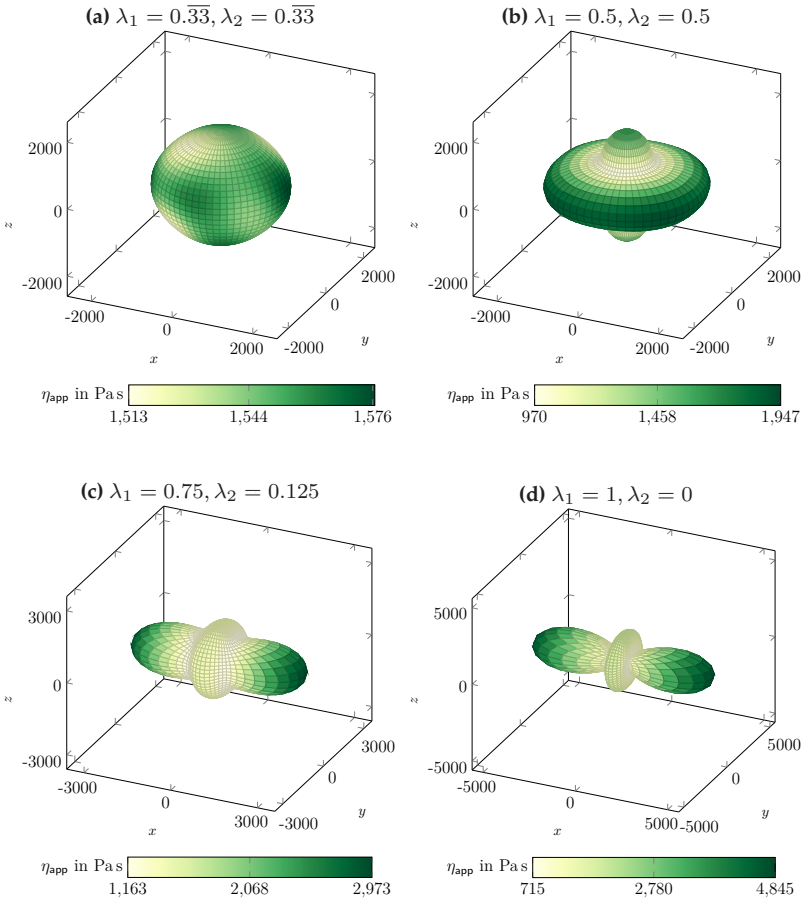

Figure 4.3: Elongational viscosity η_{app} at a shear rate $\dot{\gamma} = 10\,1/\mathrm{s}$ for isotropic (a), planar isotropic (b), transversely isotropic (c), and unidirectional (d) fiber orientation states. Figure adapted from Sterr et al. (2024b, Figure 3).

In an isotropic volume element, the fibers increase the elongational viscosity η_{app} uniformly across orientation space. Consequently, with

a magnitude of 1513 $\mathrm{Pa\,s}$, the minimum of the effective viscosity η_{app} in the isotropic state is larger than in the other orientation states. In comparison, the minima of the effective viscosity η_{app} are 970 $\mathrm{Pa\,s}$ in the planar isotropic state, 1163 $\mathrm{Pa\,s}$ in the transversely isotropic state, and 715 $\mathrm{Pa\,s}$ in the unidirectional state. Interestingly, the minima of the elongational viscosity η_{app} occur in directions where there is the least flow along the main fiber orientation directions. Because of incompressibility, the direction with the least flow in fiber direction is not perpendicular to the principal fiber orientation axis. Rather, it occurs at a specific angle which depends on the orientation state.

So far, we investigated the effective viscosity of selected fiber suspensions for a relatively low shear rate $\dot{\gamma} = 10\,\mathrm{s}^{-1}$ using the elongational viscosity η_{app}, the range $\Delta\eta_{\mathsf{app}}$, and the ratio r_{app}. However, the ratio r_{app} or popular anisotropy measures used in crystal elasticity (Kube, 2016; Ranganathan and Ostoja-Starzewski, 2008; Zener and Siegel, 1949) rely on the existence of load independent stiffness and compliance tensors. To model the effective suspension viscosity, we want to study its load dependence for all shear rates $\dot{\gamma} \in S_{\dot{\gamma}}$ in the set $S_{\dot{\gamma}}$, which includes shear rates where the effective material behavior is non-linear. Thus, a way of computing the suspension anisotropy without relying on the interpolative properties of equation (4.10) is necessary and is introduced in the following. A convenient expression for the elongational viscosity η_{app} in terms of the investigated load cases collected in the matrix $\underline{\underline{\bar{D}}}$ follows from equation (4.12) with $\bar{\boldsymbol{D}} = \dot{\gamma}/\sqrt{2}\,\boldsymbol{d} \otimes \boldsymbol{d}$ and $\bar{\boldsymbol{\tau}} = \bar{\mathbb{V}}[\bar{\boldsymbol{D}}]$, such that

$$\eta_{\mathsf{app}}(\dot{\gamma}, \underline{\lambda}, \bar{\boldsymbol{D}}) = 2\frac{\bar{\boldsymbol{D}} \cdot \bar{\boldsymbol{\tau}}}{\bar{\boldsymbol{D}} \cdot \bar{\boldsymbol{D}}}. \tag{4.17}$$

We use this expression (4.17) to define a vector $\underline{\eta}$ for all studied shear rates $\dot{\gamma}$

$$\underline{\eta}(\dot{\gamma}, \underline{\lambda}) = (\eta_{\mathsf{app}}(\dot{\gamma}, \underline{\lambda}, \bar{\boldsymbol{D}}_1), \eta_{\mathsf{app}}(\dot{\gamma}, \underline{\lambda}, \bar{\boldsymbol{D}}_2), ..., \eta_{\mathsf{app}}(\dot{\gamma}, \underline{\lambda}, \bar{\boldsymbol{D}}_6))^{\mathsf{T}}, \tag{4.18}$$

which contains the elongational viscosity η_{app} for each load case $\bar{\boldsymbol{D}}_{\mathsf{i}}$ collected in the columns of the matrix $\underline{\underline{\bar{D}}}$. To measure the average magnitude and the dispersion of the elongational viscosities η_{app} collected in the vector $\underline{\eta}$, we compute the mean μ_η and the standard deviation s_η

$$\mu_\eta(\dot{\gamma}, \underline{\lambda}) = \frac{1}{6} \sum_{i=1}^{6} \eta_{\mathsf{app},\mathsf{i}}(\dot{\gamma}, \underline{\lambda}), \tag{4.19}$$

$$s_\eta(\dot{\gamma}, \underline{\lambda}) = \sqrt{\frac{1}{6} \sum_{i=1}^{6} \left(\eta_{\mathsf{app},\mathsf{i}}(\dot{\gamma}, \underline{\lambda}) - \mu_\eta(\dot{\gamma}, \underline{\lambda})\right)^2}. \tag{4.20}$$

The standard deviation s_η is not a dimensionless quantity and its magnitude is a nominal measure of dispersion. Thus, the standard deviation s_η is unsuitable to interpret the dispersion of the values collected in the vector $\underline{\eta}$ in relation to their magnitude. Instead, we use the coefficient of variation C_η defined by the equation

$$C_\eta(\dot{\gamma}, \underline{\lambda}) = \frac{s_\eta(\dot{\gamma}, \underline{\lambda})}{\mu_\eta(\dot{\gamma}, \underline{\lambda})}, \tag{4.21}$$

to relate the standard deviation s_η to the mean μ_η and thus compute a dimensionless anisotropy measure of the suspension viscosity for a given fiber orientation state.

Also, the coefficient of variation C_η is a useful quantity to compare the anisotropy of fiber orientation states with elongational viscosities η_{app} of varying magnitudes. To study the maximum load dependent change of the anisotropy for a given fiber orientation state, we define the range over all shear rates ΔC_η

$$\Delta C_\eta(\underline{\lambda}) = \max_{\dot{\gamma}}(C_\eta(\dot{\gamma}, \underline{\lambda})) - \min_{\dot{\gamma}}(C_\eta(\dot{\gamma}, \underline{\lambda})). \tag{4.22}$$

The development of the coefficient of variation C_η for selected orientation states over the shear rate $\dot{\gamma}$, and the range ΔC_η for all fiber

orientation states are shown in Figure 4.4. For all investigated shear rates and orientation states, the coefficient of variation C_η is largest in the unidirectional state, and smallest in the isotropic state, see Figure 4.4(a). The coefficient of variation C_η for all other investigated orientation states lies between these bounds. Qualitatively, the coefficient of variation C_η, and hence, the degree of anisotropy at a given shear rate, decreases up to a shear rate $\dot{\gamma} \approx 10^3\,\mathrm{s}^{-1}$ for all orientation states. This decrease in the coefficient C_η suggests increased local velocity gradients, and thus stronger shear-thinning in the matrix, during flow along the fiber orientation directions. Quantitatively the range ΔC_η depends on the orientation state, and is largest in the unidirectional state, see Figure 4.4(b).

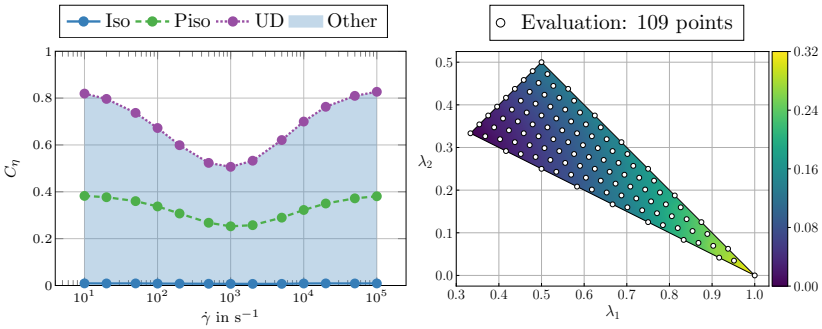

(a) C_η **(b)** ΔC_η

Figure 4.4: Coefficient of variation C_η for shear rates $\dot{\gamma} \in [10, 10^5]\,\mathrm{s}^{-1}$ (a), and range of the coefficient of variation ΔC_η (b) over the fiber orientation triangle S_T. Figure adapted from Sterr et al. (2024b, Figure 4).

In the isotropic state, the coefficient of variation C_η and its range ΔC_η are close to zero for all investigated shear rates, showing that non-linear shear thinning effects occur at equivalent strengths, independent of the load direction. With increasing degree of orientation, the coefficient of variation C_η and its range ΔC_η grow. In the planar isotropic

state, the coefficient of variation C_η varies with a range $\Delta C_\eta = 0.13$ between $C_\eta = 0.38$ at a shear rate $\dot{\gamma} = 10\,\mathrm{s}^{-1}$ and $C_\eta = 0.25$ at a shear rate $\dot{\gamma} = 10^3\,\mathrm{s}^{-1}$. The range ΔC_η is largest in the unidirectional state, where the coefficient of variation C_η varies strongly with a range $\Delta C_\eta = 0.32$ between $C_\eta = 0.82$ at a shear rate $\dot{\gamma} = 10\,\mathrm{s}^{-1}$ and $C_\eta = 0.50$ at a shear rate $\dot{\gamma} = 10^3\,\mathrm{s}^{-1}$. The distinct differences in the coefficient of variation C_η and the range ΔC_η between the studied fiber orientation states highlight the strong influence of the fiber orientation on the magnitude and anisotropy of the effective material behavior. As a consequence of the Cross-type material law (3.2) and increasing velocity gradients in the polymer matrix, the coefficient of variation C_η increases for shear rates $\dot{\gamma}$ larger than $10^3\,\mathrm{s}^{-1}$ up to similar values as observed for a shear rate $\dot{\gamma} = 10\,\mathrm{s}^{-1}$. The results discussed in this section thus underline the need to account for the shear rate and load direction dependent shear thinning behavior of the suspension when modeling the suspension viscosity. This is in line with findings in the literature (Koch, 1995; Favaloro et al., 2018; Pipes, 1992; Pipes et al., 1994), where the effect of the suspended fibers on the matrix shear rate is estimated using fiber orientation statistics. In the next section we will use a different approach, and discuss how the anisotropic shear thinning effect can be characterized with supervised machine learning based on the computational results of the FFT-based homogenization and knowledge of the local Cross-type material law.

4.4 Modeling the effective suspension viscosity

4.4.1 Model requirements

With the results presented in the previous section 4.3 at hand, we wish to model the effective viscosity of shear-thinning fiber suspensions with

analytical means and identify the model parameters using supervised machine learning. To do so, we first summarize the key criteria a model of the effective viscous behavior should fulfill. The model should

(I) be tensorial, i.e., capture shear rate and load direction dependence objectively.

(II) replicate the local Cross-type material behavior on the macro-scale, i.e., the model should show Newtonian behavior in the shear rate limits $\dot{\gamma} \to 0\,\mathrm{s}^{-1}$ and $\dot{\gamma} \to \infty\,\mathrm{s}^{-1}$, and capture the shear rate and load direction dependent, non-linear transition between the two Newtonian limits. This requirement is based on the investigations in Sterr et al. (2023, §4), the results of the anisotropy investigation in the previous section 4.3, and considerations in literature (Koch, 1995; Favaloro et al., 2018; Pipes, 1992; Pipes et al., 1994).

(III) yield an incompressible and orthotropic effective viscosity $\bar{\mathbb{V}}$. Because the fourth order fiber orientation tensors of the generated microstructures are orthotropic, see Schneider (2017) and Montgomery-Smith et al. (2011), the effective viscosity $\bar{\mathbb{V}}$ of the suspensions is orthotropic as well.

(IV) be applicable on the whole fiber orientation triangle S_T, as defined in equation (2.37).

In accordance with requirements (I) and (II), we restrict our investigations to tensorial models of the type

$$\bar{\mathbb{V}}(\boldsymbol{D}, \underline{a}) = \bar{\mathbb{V}}_\infty(\underline{a}) + \mathbb{T}_8(\boldsymbol{D}, \underline{a}) \left[\bar{\mathbb{V}}_0(\underline{a}) - \bar{\mathbb{V}}_\infty(\underline{a})\right], \tag{4.23}$$

where $\underline{a} \in \mathbb{R}^m$, $m \in \mathbb{N}$, is the vector of model parameters, $\mathbb{T}_8 : \mathsf{Sym}_0(3) \times \mathbb{R}^m \to (\mathbb{R}^3)^{\otimes 8}$ stands for an eighth order tensor function, and $\bar{\mathbb{V}}_0 : \mathbb{R}^m \to \mathsf{Sym}_0(3)$ as well as $\bar{\mathbb{V}}_\infty : \mathbb{R}^m \to \mathsf{Sym}_0(3)$ denote fourth order tensor functions. The functions $\bar{\mathbb{V}}_0$ and $\bar{\mathbb{V}}_\infty$ are used to construct the Newtonian viscosity tensors $\bar{\mathbb{V}}_0(\underline{a})$ and $\bar{\mathbb{V}}_\infty(\underline{a})$ in the shear rate limits $\dot{\gamma} \to 0\,\mathrm{s}^{-1}$ and $\dot{\gamma} \to \infty\,\mathrm{s}^{-1}$, respectively. Equation (4.23)

is a tensor-valued generalization of the Cross-type material law (3.2), where the scalar Newtonian viscosities are replaced by the viscosity tensors $\bar{\mathbb{V}}_0(\underline{a})$ and $\bar{\mathbb{V}}_\infty(\underline{a})$, and the function $\mathbb{T}_8$ is introduced to model the non-linear transition between the two Newtonian viscosity tensors $\bar{\mathbb{V}}_0(\underline{a})$ and $\bar{\mathbb{V}}_\infty(\underline{a})$. The function $\mathbb{T}_8$ varies between the individual models, and encodes the direction dependent non-linearity of the models as stated in requirement (II). In summary, three objects in the Ansatz (4.23) need to be modeled: the Newtonian viscosity tensors $\bar{\mathbb{V}}_0(\underline{a})$ and $\bar{\mathbb{V}}_\infty(\underline{a})$, as well as the eighth order tensor function $\mathbb{T}_8$ controlling the anisotropic and non-linear shear rate dependence. In the following sections, we discuss the respective modeling approaches for these three objects.

4.4.2 Modeling the Newtonian limits of the effective suspension viscosity

To integrate orthotropic symmetry and incompressibility according to requirement (III) into the models, we first consider the vector space V_0 of fourth order incompressible tensors with minor and major symmetries

$$\begin{aligned}\mathsf{V}_0 = \{\mathbb{X} \quad | \quad & \mathbb{X} \in (\mathbb{R}^3)^{\otimes 4}, \quad \text{and} \quad \mathbb{X}[\boldsymbol{I}] = 0 \\ & \text{and} \quad \mathbb{X}^{\mathsf{T}_H} = \mathbb{X}^{\mathsf{T}_L} = \mathbb{X}^{\mathsf{T}_R} = \mathbb{X}\},\end{aligned} \tag{4.24}$$

where $(\cdot)^{\mathsf{T}_H}$, $(\cdot)^{\mathsf{T}_L}$, and $(\cdot)^{\mathsf{T}_R}$ stand for major transposition, left transposition, and right transposition, respectively. Second, we then define a basis $\mathcal{B}$ of the space V_0

$$\underline{\underline{\mathcal{B}}} = \begin{bmatrix} 0 & \frac{-2}{\sqrt{6}} & 0 & 0 & 0 \\ \frac{-1}{\sqrt{2}} & \frac{1}{\sqrt{6}} & 0 & 0 & 0 \\ \frac{1}{\sqrt{2}} & \frac{1}{\sqrt{6}} & 0 & 0 & 0 \\ 0 & 0 & 1 & 0 & 0 \\ 0 & 0 & 0 & 1 & 0 \\ 0 & 0 & 0 & 0 & 1 \end{bmatrix}, \tag{4.25}$$

such that the columns of the matrix $\underline{\underline{\mathcal{B}}}$ represent the basis vectors of $\mathcal{B}$ in Mandel notation. Finally, using the basis $\mathcal{B}$, we define a function

$$\mathbb{A} : \mathbb{R}^6 \to \mathsf{V}_0^+(3), \tag{4.26}$$

$$\underline{a} \mapsto \mathcal{P}_{\mathcal{B}}^+ \mathbb{M}(\underline{a}) = \mathcal{P}_{\mathcal{B}}^+ \begin{bmatrix} a_1 & a_2 & 0 & 0 & 0 \\ a_2 & a_3 & 0 & 0 & 0 \\ 0 & 0 & a_4 & 0 & 0 \\ 0 & 0 & 0 & a_5 & 0 \\ 0 & 0 & 0 & 0 & a_6 \end{bmatrix}_{\mathcal{B}}, \tag{4.27}$$

which constructs an orthotropic fourth order tensor using the components a_i of the model parameter vector $\underline{a}$, and the non-unique projector $\mathcal{P}_{\mathcal{B}}^+$ into the space V_0^+ of fourth order tensors that are positive definite on the space spanned by the basis $\mathcal{B}$. Employing eigendecomposition, we define the action of the projector $\mathcal{P}_{\mathcal{B}}^+$ as

$$\mathcal{P}_{\mathcal{B}}^+[\mathbb{X}] = \mathcal{P}_{\mathcal{B}}^+ \left[\sum_{i=0}^{5} \lambda_i \, \boldsymbol{p}_i \otimes \boldsymbol{p}_i \right] = \sum_{i=0}^{5} \max(\lambda_i, \beta) \, \boldsymbol{p}_i \otimes \boldsymbol{p}_i, \tag{4.28}$$

where λ_i and $\boldsymbol{p}_i$ denote eigenvalue eigentensor pairs of a fourth order tensor $\mathbb{X}$ on the space spanned by the basis $\mathcal{B}$, and $\beta \in \mathbb{R}_{>0}$ is a small positive and real constant. The definition of the projection operator $\mathcal{P}_{\mathcal{B}}^+$ involves a tunable constant β, which is required for numerical purposes. In fact, formally setting β to zero leads to the projector onto positive semi-definite tensors, i.e., those which may be degenerate. However, positive definiteness on the incompressible subspace $\mathcal{B}$ is preferred over positive semi-definiteness, because of the following physical and numerical reasons. We wish to use the tensor function $\mathbb{A}$ to build fourth order tensors $\mathbb{X} \in \mathsf{V}_0^+$ from six model parameters, i.e., the viscosity tensors $\bar{\mathbb{V}}_0(\underline{a})$ and $\bar{\mathbb{V}}_\infty(\underline{a})$. Therefore, encoding a vanishing stress response through vanishing eigenvalues would not adhere to the physical model considered in the context of this thesis.

4.4.3 Modeling the anisotropic and non-linear shear rate dependence of the effective suspension viscosity

To capture the anisotropic and non-linear viscous behavior in accordance with requirement (II), we incorporate a generalized distance g from zero load

$$g : \mathsf{Sym}_0(3) \times \mathbb{R}^7 \to \mathbb{R}, \tag{4.29}$$

$$(\boldsymbol{D}, \underline{a}) \mapsto (\boldsymbol{D} \cdot \mathbb{A}(\underline{a})[\boldsymbol{D}])^{a_7}, \tag{4.30}$$

into the models, which is similar to the Mahalanobis distance (Mahalanobis, 1936) popular in statistics. The generalized distance g depends on the components a_i collected in the model parameter vector $\underline{a}$, as well as the magnitude and direction of the shear rate tensor $\boldsymbol{D}$. Because of these properties, we use the generalized distance g as a model building block to encode the fiber orientation state specific, anisotropic shear rate dependence of the effective suspension viscosity. However, for an exponent $a_7 < 1$ the gradient of this generalized distance g is singular whenever $\boldsymbol{D} \cdot \mathbb{A}(\underline{a})[\boldsymbol{D}]$ vanishes, posing a problem during gradient based learning of the model parameters $\underline{a}$. This singularity is circumvented by the enforced positive definiteness of the tensors constructed by the function $\mathbb{A}$ and non-vanishing load $\boldsymbol{D}$. Here, the constant β acts as a lower bound on the eigenvalues of the tensor $\mathbb{A}(\underline{a})$, as can be seen from equations (4.26) and (4.28), and restricts the space of possible tensors $\mathbb{A}(\underline{a})$ that can be constructed from the model parameters $\underline{a}$. Improper choice of the constant β, such that β is greater than the smallest eigenvalue of the optimal tensor $\mathbb{A}(\underline{a})$, could therefore influence the quality of fit. However, because we wish to learn the model parameters $\underline{a}$ from homogenization data, the optimal tensor $\mathbb{A}(\underline{a})$ and its smallest eigenvalue are not known a priori. Therefore, the constant β should be chosen to be a small number, and we nominally select $\beta = 10^{-6}$ in the unit of the associated eigenvalue λ_i. To model the anisotropic Cross-type

non-linearity using the generalized distance g, we define two non-linear eighth order tensor functions $\mathbb{T}_8^{(1)}$ and $\mathbb{T}_8^{(2)}$ through their actions on an orthotropic tensor $\mathbb{X} \in \mathsf{Sym}_0$. We define the function $\mathbb{T}_8^{(1)}$ through

$$\mathbb{T}_8^{(1)}(\boldsymbol{D}, \underline{a})\,[\mathbb{X}] = \frac{\mathbb{X}}{1 + g(\boldsymbol{D}, \underline{a})}, \quad \underline{a} \in \mathbb{R}^7, \tag{4.31}$$

such that the scalar shear rate dependence of the Cross-type model (3.2) is replaced by the generalized distance g (4.29). Thus, the function $\mathbb{T}_8^{(1)}$ scales all the components of the orthotropic tensor $\mathbb{X}$ equally, depending on the load $\boldsymbol{D}$ and the model parameter vector $\underline{a}$. Because all components of the tensor $\mathbb{X}$ are scaled equally, the anisotropy of the tensor $\mathbb{X}$ remains unchanged under the function $\mathbb{T}_8^{(1)}$. However, the non-linear shear rate dependence encoded in the function $\mathbb{T}_8^{(1)}$ may be anisotropic since the magnitude of the scaling depends on the function g, and hence on a possibly anisotropic tensor $\mathbb{A}(\underline{a})$ and the load $\boldsymbol{D}$. Of the seven model parameters collected in the model parameter vector $\underline{a}$, six model parameters control the influence of the direction of the load $\boldsymbol{D}$ on the scaling, and one parameter controls the rate of transition between the Newtonian limits for shear rates $\dot{\gamma} \to 0$ and $\dot{\gamma} \to \infty$.

To allow for greater flexibility in the scaling of the orthotropic tensor $\mathbb{X}$, we also define the tensor function $\mathbb{T}_8^{(2)}$ through

$$\mathbb{T}_8^{(2)}(\boldsymbol{D}, \underline{a})\,[\mathbb{X}] = \begin{bmatrix} z_{11} & z_{12} & 0 & 0 & 0 \\ z_{12} & z_{22} & 0 & 0 & 0 \\ 0 & 0 & z_{33} & 0 & 0 \\ 0 & 0 & 0 & z_{44} & 0 \\ 0 & 0 & 0 & 0 & z_{55} \end{bmatrix}_{\mathcal{B}}, \quad \underline{a} \in \mathbb{R}^{42}, \tag{4.32}$$

$$z_{11} = h_1(\boldsymbol{D}, \underline{a}) X_{11}, \qquad z_{12} = h_2(\boldsymbol{D}, \underline{a}) X_{12}, \tag{4.33}$$

$$z_{22} = h_3(\boldsymbol{D}, \underline{a}) X_{22}, \qquad z_{33} = h_4(\boldsymbol{D}, \underline{a}) X_{33}, \tag{4.34}$$

$$z_{44} = h_5(\boldsymbol{D}, \underline{a}) X_{44}, \qquad z_{55} = h_6(\boldsymbol{D}, \underline{a}) X_{55}, \tag{4.35}$$

such that the six components of the tensor $\mathbb{X}$ are scaled individually by a scalar $h_i(\boldsymbol{D}, \underline{a}),\ i \in \{1,2,3,4,5,6\}$, defined as

$$h_i(\boldsymbol{D}, \underline{a}) = \frac{1}{1 + g(\boldsymbol{D}, \underline{f}_i)}, \quad \underline{f}_i = (a_{7(i-1)+1}, ..., a_{7i}) \in \mathbb{R}^7. \tag{4.36}$$

Like the scaling factor in the function $\mathbb{T}_8^{(1)}$, the scalars $h_i(\boldsymbol{D}, \underline{a})$ are each computed from seven model parameters, the shear rate tensor $\boldsymbol{D}$, and the function g. Therefore, the tensor $\mathbb{X}$ is not only scaled under the function $\mathbb{T}_8^{(2)}$, but the anisotropy of the tensor $\mathbb{X}$ may also change under the function $\mathbb{T}_8^{(2)}$. In this sense, the function $\mathbb{T}_8^{(1)}$ is a special case of the function $\mathbb{T}_8^{(2)}$, where all scalars $h_i(\boldsymbol{D}, \underline{a})$ are equal. The increased flexibility in the scaling of the tensor $\mathbb{X}$ with function $\mathbb{T}_8^{(2)}$ requires 36 parameters to control the influence of the direction of the load $\boldsymbol{D}$, and six parameters to control the rate of transition between the Newtonian limits for shear rates $\dot{\gamma} \to 0$ and $\dot{\gamma} \to \infty$. This results in a total of 42 parameters for the function $\mathbb{T}_8^{(2)}$.

4.4.4 Definitions of effective suspension viscosity models

In the following, we combine the definitions of the previous sections 4.4.2 and 4.4.3 with the Ansatz (4.23) to build four models for the effective suspension viscosity. With the symbol $+\!\!+$ denoting concatenation of vectors the four models presented in Table 4.3 are considered and described in the following.

Model 1

In Model 1, we use the function $\mathbb{A}$ (4.26) to construct the Newtonian viscosity tensors $\bar{\mathbb{V}}_0(\underline{b})$ and $\bar{\mathbb{V}}_\infty(\underline{c})$ from twelve model parameters collected in the vectors $\underline{b} \in \mathbb{R}^6$ and $\underline{c} \in \mathbb{R}^6$. Also, we use the function $\mathbb{T}_8^{(1)}$ (4.31) with seven parameters collected in the vector $\underline{d} \in \mathbb{R}^7$ to model the anisotropic and non-linear shear rate dependence of the effective sus-

pension viscosity. Overall, Model 1 has 19 parameters and is the most general considered model that uses the function $\mathbb{T}_8^{(1)}$.

Model 2

Like in Model 1, we use the function $\mathbb{A}$ to construct the Newtonian viscosity tensor $\bar{\mathbb{V}}_\infty(\underline{b})$ in the shear rate limit $\dot{\gamma} \to \infty\,\mathrm{s}^{-1}$ from six model parameters, and the non-linear function $\mathbb{T}_8^{(1)}$ to model the non-linear transition between the Newtonian limits with seven model parameters. These 13 parameters are collected in the vectors $\underline{c} \in \mathbb{R}^6$ and $\underline{d} \in \mathbb{R}^7$. However, in Model 1, the viscosity tensor $\bar{\mathbb{V}}_0(\underline{b})$ in the shear rate limit $\dot{\gamma} \to 0\,\mathrm{s}^{-1}$ is also constructed with the function $\mathbb{A}$ (4.26), using six model parameters. In Model 2, we exploit the fact that the viscosity tensors $\bar{\mathbb{V}}_0(\underline{b})$ and $\bar{\mathbb{V}}_\infty(\underline{c})$ share the same anisotropy in the shear rate limits $\dot{\gamma} \to 0\,\mathrm{s}^{-1}$ and $\dot{\gamma} \to \infty\,\mathrm{s}^{-1}$, see Figure 4.4 and Sterr et al. (2023), and express the viscosity tensor $\bar{\mathbb{V}}_0(\underline{b})$ as a scalar multiple of the tensor $\bar{\mathbb{V}}_\infty(\underline{c})$, such that the condition

$$\mathbb{V}_0(\underline{b}) = b_1\,\mathbb{V}_\infty(\underline{c}), \tag{4.37}$$

Model 1			**Model 2**		
parameters: $m = 19$,	$\underline{b}, \underline{c} \in \mathbb{R}^6$, $\underline{d} \in \mathbb{R}^7$		parameters: $m = 14$,	$\underline{b} \in \mathbb{R}^1$, $\underline{c} \in \mathbb{R}^6$, $\underline{d} \in \mathbb{R}^7$	
$\underline{a}$	$=$	$\underline{b} \shuffle \underline{c} \shuffle \underline{d}$	$\underline{a}$	$=$	$\underline{b} \shuffle \underline{c} \shuffle \underline{d}$
$\bar{\mathbb{V}}_0(\underline{b})$	$=$	$\mathbb{A}(\underline{b})$	$\bar{\mathbb{V}}_0(\underline{b})$	$=$	$b_1 \, \bar{\mathbb{V}}_\infty(\underline{c})$
$\bar{\mathbb{V}}_\infty(\underline{c})$	$=$	$\mathbb{A}(\underline{c})$	$\bar{\mathbb{V}}_\infty(\underline{c})$	$=$	$\mathbb{A}(\underline{c})$
$\mathbb{T}_8(\boldsymbol{D}, \underline{d})$	$=$	$\mathbb{T}_8^{(1)}(\boldsymbol{D}, \underline{d})$	$\mathbb{T}_8(\boldsymbol{D}, \underline{d})$	$=$	$\mathbb{T}_8^{(1)}(\boldsymbol{D}, \underline{d})$
$\bar{\mathbb{V}}(\boldsymbol{D}, \underline{a}) = \mathbb{A}(\underline{c}) + \dfrac{\mathbb{A}(\underline{b}) - \mathbb{A}(\underline{c})}{1 + (\boldsymbol{D} \cdot \mathbb{A}(\underline{d})[\boldsymbol{D}])^{d_7}}$			$\bar{\mathbb{V}}(\boldsymbol{D}, \underline{a}) = \mathbb{A}(\underline{c}) \left(1 + \dfrac{b_1 - 1}{1 + (\boldsymbol{D} \cdot \mathbb{A}(\underline{d})[\boldsymbol{D}])^{d_7}}\right)$		
Model 3			**Model 4**		
parameters: $m = 11$,	$\underline{b} \in \mathbb{R}^1$, $\underline{c} \in \mathbb{R}^3$, $\underline{d} \in \mathbb{R}^7$		parameters: $m = 49$,	$\underline{b} \in \mathbb{R}^1$, $\underline{c} \in \mathbb{R}^6$, $\underline{d} \in \mathbb{R}^{42}$	
$\underline{a}$	$=$	$\underline{b} \shuffle \underline{c} \shuffle \underline{d}$	$\underline{a}$	$=$	$\underline{b} \shuffle \underline{c} \shuffle \underline{d}$
$\bar{\mathbb{V}}_0(\underline{b})$	$=$	$b_1 \, \bar{\mathbb{V}}_\infty(\underline{c})$	$\bar{\mathbb{V}}_0(\underline{b})$	$=$	$b_1 \, \bar{\mathbb{V}}_\infty(\underline{c})$
$\bar{\mathbb{V}}_\infty(\underline{c})$	$=$	$\mathbb{P}_2 \left(c_1 \, \mathbb{P}_2 + c_2 \, \boldsymbol{I} \square_s \boldsymbol{N} + c_3 \, \mathbb{N}\right) \mathbb{P}_2$	$\bar{\mathbb{V}}_\infty(\underline{c})$	$=$	$\mathbb{A}(\underline{c})$
$\mathbb{T}_8(\boldsymbol{D}, \underline{d})$	$=$	$\mathbb{T}_8^{(1)}(\boldsymbol{D}, \underline{d})$	$\mathbb{T}_8(\boldsymbol{D}, \underline{d})$	$=$	$\mathbb{T}_8^{(2)}(\boldsymbol{D}, \underline{d})$
$\bar{\mathbb{V}}(\boldsymbol{D}, \underline{a}) = \bar{\mathbb{V}}_\infty(\underline{c}) \left(1 + \dfrac{b_1 - 1}{1 + (\boldsymbol{D} \cdot \mathbb{A}(\underline{d})[\boldsymbol{D}])^{d_7}}\right)$			$\bar{\mathbb{V}}(\boldsymbol{D}, \underline{a}) = \mathbb{A}(\underline{c}) + \mathbb{T}_8^{(2)}(\boldsymbol{D}, \underline{d}) \, [(b_1 - 1)\mathbb{A}(\underline{c})]$		

Table 4.3: Number of parameters m, choices for the functions $\bar{\mathbb{V}}_0$, $\bar{\mathbb{V}}_\infty$, and $\mathbb{T}_8$, as well as the complete expression for the effective viscosity tensor $\bar{\mathbb{V}}(\boldsymbol{D}, \underline{a})$ for the Models 1, 2, 3, and 4. Table adapted from Sterr et al. (2024b, Table 3).

is satisfied. This relation reduces the number of parameters from 19 in Model 1 to 14 in Model 2. We found that this adaption introduces only small errors, as we discuss in section 4.4.6 in more detail, and use equation (4.37) in Model 3 and Model 4 as well.

Model 3

In Model 3, like in Model 1 and Model 2, we use the function $\mathbb{T}_8^{(1)}$ to model the non-linear transition between the Newtonian limits with seven model parameters collected in the vector $\underline{d} \in \mathbb{R}^7$. Also, as in Model 2, we use equation (4.37) to relate the viscosity tensors $\bar{\mathbb{V}}_0(\underline{b})$ and $\bar{\mathbb{V}}_\infty(\underline{c})$ via a scalar coefficient collected in the vector $\underline{b} \in \mathbb{R}^1$. To further reduce the number of model parameters through physical considerations motivated by superposition and orientation averaging (Ericksen, 1960; Tucker III, 1991; Bertóti et al., 2021), we introduce the equation

$$\bar{\mathbb{V}}_\infty(\underline{c}) = \mathbb{P}_2 \left(c_1 \, \mathbb{P}_2 + c_2 \, \boldsymbol{I} \square_s \boldsymbol{N} + c_3 \, \mathbb{N}\right) \mathbb{P}_2, \tag{4.38}$$

for the viscosity tensor $\bar{\mathbb{V}}_\infty(\underline{c})$, where $\mathbb{P}_2$ denotes the identity on the space $\mathsf{Sym}_0(3)$. The operator $\square_s$ stands for the symmetrized box product, which, for the second order tensors $\boldsymbol{A}, \boldsymbol{B}, \boldsymbol{C} \in \left(\mathbb{R}^3\right)^{\otimes 2}$, is defined as

$$\boldsymbol{A} \square_s \boldsymbol{B} = \frac{1}{2}(\boldsymbol{A} \square \boldsymbol{B} + \boldsymbol{B} \square \boldsymbol{A}), \quad \text{where} (\boldsymbol{A} \square \boldsymbol{B})[\boldsymbol{C}] = \boldsymbol{A}\boldsymbol{C}\boldsymbol{B}. \tag{4.39}$$

Overall, this reduces the number of parameters from 14 in Model 2 to 11 in Model 3.

Model 4

In Model 4, in contrast to the Models 1, 2, and 3, we use the function $\mathbb{T}_8^{(2)}$ instead of the function $\mathbb{T}_8^{(1)}$ to model the non-linear transition between the Newtonian limits. As discussed in the previous section 4.4.3, this allows for greater flexibility in exchange for more model parameters, making Model 4 the most general of the considered models. Like in Model 2 and Model 3, we use seven parameters collected in the vectors $\underline{b} \in \mathbb{R}^1$ and $\underline{c} \in \mathbb{R}^6$ to model the viscosity tensors $\bar{\mathbb{V}}_0(\underline{b})$ and $\bar{\mathbb{V}}_\infty(\underline{c})$.

In combination with the 42 input parameters of the function $\mathbb{T}_8^{(2)}$, which we collect in the vector $\underline{d}$, this leads to a total of 49 model parameters for Model 4. Overall, each model parameter controls a distinct effect or quantity of the model. In other words, Model 4 could not be expressed with fewer parameters while maintaining the same type of non-linearity and the same degree of modeling flexibility.

4.4.5 Supervised learning of model parameters

In the previous sections 4.4.1 and 4.4.4, we described the requirements for models of the effective suspension viscosity and presented four model candidates satisfying these requirements. In this section, we discuss the supervised machine learning strategy we use to identify the model parameters. To learn the model parameters from the data obtained with FFT-based computational homogenization, we first construct a loss function $\mathcal{L}$ measuring the difference between the model predictions and the FFT-based computational results, and then minimize the loss $\mathcal{L}$ using the ADAM (Kingma and Ba, 2014) optimization algorithm. We consider all fiber orientation states $\underline{\lambda} \in S_{\mathsf{T}}^{109}$ in the set $S_{\mathsf{T}}^{109} \subset S_{\mathsf{T}}$ of 109 points of the discretized fiber orientation triangle shown in Figures 4.1a and 4.4(b). For every load case $\bar{\boldsymbol{D}}$, fiber orientation state $\underline{\lambda}$, and parameter vector $\underline{a}$, we define the loss $\mathcal{L}$

$$\mathcal{L}(\bar{\boldsymbol{D}}, \underline{\lambda}, \underline{a}) = \frac{||\bar{\boldsymbol{\tau}}^{\mathsf{FFT}}(\bar{\boldsymbol{D}}, \underline{\lambda}) - \bar{\boldsymbol{\tau}}^{\mathsf{Model}}(\bar{\boldsymbol{D}}, \underline{\lambda}, \underline{a})||_2}{||\bar{\boldsymbol{\tau}}^{\mathsf{FFT}}(\bar{\boldsymbol{D}}, \underline{\lambda})||_2}, \tag{4.40}$$

where $||\cdot||_2$ stands for the Euclidean norm, $\bar{\boldsymbol{\tau}}^{\mathsf{model}} : \mathsf{Sym}_0(3) \times \mathbb{R}^2 \times \mathbb{R}^m \to \mathsf{Sym}_0(3)$ refers to the effective stress predicted by a particular model, and $\bar{\boldsymbol{\tau}}^{\mathsf{FFT}} : \mathsf{Sym}_0(3) \times \mathbb{R}^2 \to \mathsf{Sym}_0(3)$ refers to the effective stress obtained with FFT-based computational homogenization. Similar to section 4.3, we omit the dependence of the loss $\mathcal{L}$ and the derived quantities on various variables for improved readability and compactness. For each model and fiber orientation

state $\underline{\lambda}$, we wish to identify the model parameters $\underline{a}$ minimizing the worst case loss $\mathcal{L}$ for the set of investigated load cases $\bar{\boldsymbol{D}}_{\dot{\gamma}}$, such that

$$\underline{a}(\underline{\lambda}) = \text{argmin}_{\underline{a}\in\mathbb{R}^m} \max_{\bar{\boldsymbol{D}}\in\bar{\boldsymbol{D}}_{\dot{\gamma}}} \mathcal{L}(\bar{\boldsymbol{D}}, \underline{\lambda}, \underline{a}). \tag{4.41}$$

Here, the set of investigated load cases $\bar{\boldsymbol{D}}_{\dot{\gamma}}$ is defined via equations (3.44) and (3.35). However, since the models described in the previous section are not convex in the model parameters $\underline{a}$ and have multiple local minima, the exact minimizer $\underline{a}$ is difficult to determine. We wish to start our investigations with a word of warning: identifying the model parameters from computational multiscale simulations does not qualify as a mathematically well-posed problem (Kabanikhin, 2008), for a number of reasons. For a start, there might not be a unique solution, and the outcome of the learning process, i.e., the model parameters, might change drastically for small variations in the data. Also, depending on the optimization algorithm and the optimization hyperparameters, the learned model parameters can vary as well. Accordingly, the model parameters obtained with the supervised learning procedure we present in this chapter are possibly not the global minimizers of the optimization problem (4.41). However, as we show in the next section 4.4.6, the presented supervised learning procedure can be employed to successfully identify model parameters which result in model predictions with engineering accuracy. To capitalize on the advances in the field of non-convex optimization and machine learning, we use the Python programming language and the machine learning framework PyTorch (Paszke et al., 2019) with version 1.12 to identify the model parameters $\underline{a}$. When this chapter was written, more recent PyTorch versions were available that feature Just In Time (JIT) compilation, which could possibly increase the performance of custom code modules. However, for compatibility with existing code, we use version 1.12. For each model and fiber orientation state $\underline{\lambda}$, we randomly initialized 5000 realizations of the parameter vector $\underline{a}$ and then used the field-tested ADAM (Kingma and

Ba, 2014) algorithm to improve the initial guesses, thus generating the set S_{min} of minimizing parameter vectors $\underline{a}$. We selected the ADAM algorithm from the optimization algorithms available in the PyTorch framework, since the ADAM algorithm combines an adaptive learning rate with a classical momentum (Polyak, 1964) based approach. This provides advantages over the standard gradient descent method (Kabel et al., 2014; Ruder, 2016), and algorithms relying on adaptive learning rates alone, such as AdaGrad (Duchi et al., 2011), AdaDelta (Zeiler, 2012) and RMSprop (Tieleman et al., 2012). For a detailed discussion on the convergence properties of the ADAM algorithm and its variants, we refer the reader to an article by Chen et al. (2018). Also, for an overview on a variety of other optimization algorithms in machine learning, we refer the reader to a review by Sun et al. (2019). Conveniently, the ADAM algorithm's learning rate hyperparameters are approximate bounds of the optimization step size. Exploiting this feature, we use PyTorch's option to define parameter groups with individually varying learning options for parameters with different magnitudes, such that the step sizes for nominally large parameters are not bounded by the step sizes for nominally small ones. As a viable alternative to first-order optimization techniques, PyTorch also offers the powerful second-order optimization algorithm L-BFGS (Liu and Nocedal, 1989). However, when this chapter was written, the PyTorch L-BFGS algorithm did not support multiple learning rates and parameter groups, which we have found to be valuable in accelerating convergence. Therefore, we opted to use the first-order optimization algorithm ADAM. Overall, we use four parameter groups, with one group each for the parameters of the functions $\bar{\mathbb{V}}_0$ and $\bar{\mathbb{V}}_\infty$, as well as one group each for the parameters associated with the anisotropy and the rate of non-linear transition encoded in the tensor function $\mathbb{T}_8$, see equations (4.31), (4.32) and (4.36). We distinguish the two parameter groups associated with the tensor function $\mathbb{T}_8$ with the symbols G_8^{aniso}, which contains six parameters in case of the function $\mathbb{T}_8^{(1)}$ and 36 parameters in the case

of the function $\mathbb{T}_8^{(2)}$, as well as the group G_8^{expo} containing one and six parameters for the functions $\mathbb{T}_8^{(1)}$ and $\mathbb{T}_8^{(2)}$, respectively. Except for Model 1, the learning rates for the respective parameter groups were chosen as shown in Table 4.4. For Model 1 in particular, the learning rate for the parameters associated with the function $\bar{\mathbb{V}}_0$ was chosen as 0.5, because Model 1 does not use the scalar relationship (4.37). We determined the numerical values of the learning rates for each parameter group by trial and error. To improve convergence towards minima as the learning process proceeds (Darken and Moody, 1990; Darken et al., 1992), we used PyTorch's ReduceLROnPlateau learning rate scheduler to half the learning rates if the loss $\mathcal{L}$ has not improved for 200 epochs. This rule was applied with a cooldown of 400 epochs and all other options were kept standard. For the ADAM algorithm, other than the learning rates, standard hyperparameters were used such that the two momentum coefficients β_1 and β_2 are set to $\beta_1 = 0.9$ and $\beta_2 = 0.999$, and the stabilization constant ε is set to $\varepsilon = 10^{-8}$. Finally, we consider the learning process to be finished when the loss $\mathcal{L}$ has not improved for 2000 epochs.

	$\bar{\mathbb{V}}_0$	$\bar{\mathbb{V}}_\infty$	G_8^{aniso}	G_8^{expo}
Learning rate	$5 \cdot 10^{-3}$	$5 \cdot 10^{-1}$	$5 \cdot 10^{-7}$	$5 \cdot 10^{-2}$

Table 4.4: Learning rate hyperparameter by parameter group for use with the ADAM algorithm. Table adapted from Sterr et al. (2024b, Table 4).

4.4.6 Model accuracy

To compare the accuracy of the presented models, we define error measures and describe a validation procedure in the following. Since finding a global minimum for the problem (4.41) is hard, we restrict to the set of minimizing parameters S_{min}, and identify the parameters $\underline{a}^{\mathsf{min}} \in S_{\mathsf{min}}$ minimizing the worst case loss $\mathcal{L}$ over the set of investigated load

cases $\bar{\boldsymbol{D}}_{\dot{\gamma}}$, such that

$$\underline{a}^{\mathsf{min}}(\underline{\lambda}) = \text{argmin}_{\underline{a}\in S_{\mathsf{min}}} \max_{\bar{\boldsymbol{D}}\in\bar{\boldsymbol{D}}_{\dot{\gamma}}} \mathcal{L}(\bar{\boldsymbol{D}}, \underline{\lambda}, \underline{a}). \tag{4.42}$$

The minimizing parameters $\underline{a}^{\mathsf{min}}$ are only available on the given discretization points $\underline{\lambda}$ where homogenization data is available as well. Yet, in accordance with requirement (IV), we are interested in generalizing a given model for fiber orientation states $\underline{\lambda}$ where no minimizing parameters $\underline{a}^{\mathsf{min}}$ are available. For this purpose, we follow Köbler et al. (2018) and use a convex linear combination to interpolate stresses as follows. Suppose the nodes $\underline{\lambda}_1, \underline{\lambda}_2$, and $\underline{\lambda}_3$ form a triangle and the minimizing parameters $\underline{a}^{\mathsf{min}}$ are known in those nodes. Then we compute the effective stresses $\bar{\boldsymbol{\tau}}^{\mathsf{C}}$ at some point $\underline{\lambda}$

$$\bar{\boldsymbol{\tau}}^{\mathsf{C}}(\bar{\boldsymbol{D}}, \underline{\lambda}) = \sum_{i=1}^{3} s_i\, \bar{\boldsymbol{\tau}}^{\mathsf{model}}(\bar{\boldsymbol{D}}, \underline{\lambda}_i, \underline{a}^{\mathsf{min}}(\underline{\lambda}_i)), \tag{4.43}$$

$$\underline{\lambda} = s_1\, \underline{\lambda}_1 + s_2\, \underline{\lambda}_2 + s_3\, \underline{\lambda}_3, \quad s_i \geq 0,\, i \in 1,2,3,\, \sum_{i=1}^{3} s_i = 1, \tag{4.44}$$

through interpolation of the model stresses $\bar{\boldsymbol{\tau}}^{\mathsf{model}}$ at the points $\underline{\lambda}_1, \underline{\lambda}_2$, and $\underline{\lambda}_3$. In addition to generalizing the models over the entire fiber orientation triangle S_{T}, we use equation (4.43) to validate the models against the data obtained with FFT-based computational homogenization. For this purpose, we define the validation error e_{V} similarly to the loss $\mathcal{L}$, i.e., we define

$$e_{\mathsf{V}}(\bar{\boldsymbol{D}}, \underline{\lambda}) = \frac{||\bar{\boldsymbol{\tau}}^{\mathsf{FFT}}(\bar{\boldsymbol{D}}, \underline{\lambda}) - \bar{\boldsymbol{\tau}}^{\mathsf{C}}(\bar{\boldsymbol{D}}, \underline{\lambda})||_2}{||\bar{\boldsymbol{\tau}}^{\mathsf{FFT}}(\bar{\boldsymbol{D}}, \underline{\lambda})||_2}, \tag{4.45}$$

for each considered model. Of the 109 triangulation points $\underline{\lambda}$ contained in the set S_{T}^{109} we designate 45 points as the set $S_{\mathsf{T}}^{\mathsf{F}} \subset S_{\mathsf{T}}^{109}$ of fitting points $\underline{\lambda}^{\mathsf{F}}$, see Figure 4.5. For validation purposes, we designate the

centroids of the triangles formed by the fitting points $\underline{\lambda}^{\mathsf{F}}$ as validation points, defining the set $S_{\mathsf{T}}^{\mathsf{V}} \subset S_{\mathsf{T}}^{109}$ of 64 validation points $\underline{\lambda}^{\mathsf{V}}$. By definition of the interpolation (4.43), the loss $\mathcal{L}$ coincides with the validation error e_{V} at the fitting points $\underline{\lambda}^{\mathsf{F}}$. To study the quality of fit and the quality of the stress interpolation, we define the largest loss $\mathcal{L}^{\max}$ and the largest validation error $e_{\mathsf{V}}^{\max}$

$$\mathcal{L}^{\max} = \max_{\underline{\lambda} \in S_{\mathsf{T}}^{109}} \max_{\bar{\boldsymbol{D}} \in \bar{\boldsymbol{D}}_{\dot{\gamma}}} \mathcal{L}(\bar{\boldsymbol{D}}, \underline{\lambda}, \underline{a}^{\min}(\underline{\lambda})), \quad e_{\mathsf{V}}^{\max} = \max_{\underline{\lambda} \in S_{\mathsf{T}}^{109}} \max_{\bar{\boldsymbol{D}} \in \bar{\boldsymbol{D}}_{\dot{\gamma}}} e_{\mathsf{V}}(\bar{\boldsymbol{D}}, \underline{\lambda}). \tag{4.46}$$

Furthermore, we define the mean validation error $e_{\mathsf{V}}^{\mathsf{mean}}$ and the maximum validation error $e_{\mathsf{V}}^{\bar{\boldsymbol{D}}}$ over the set of investigated load cases $\bar{\boldsymbol{D}}_{\dot{\gamma}}$

$$e_{\mathsf{V}}^{\mathsf{mean}} = \frac{1}{109} \sum_{\underline{\lambda} \in S_{\mathsf{T}}^{109}} \max_{\bar{\boldsymbol{D}} \in \bar{\boldsymbol{D}}_{\dot{\gamma}}} e_{\mathsf{V}}(\bar{\boldsymbol{D}}, \underline{\lambda}), \quad e_{\mathsf{V}}^{\bar{\boldsymbol{D}}}(\underline{\lambda}) = \max_{\bar{\boldsymbol{D}} \in \bar{\boldsymbol{D}}_{\dot{\gamma}}} e_{\mathsf{V}}(\bar{\boldsymbol{D}}, \underline{\lambda}), \tag{4.47}$$

that occurred for a given model on the discretized fiber orientation triangle. Before discussing the prediction accuracy of the presented models in detail, we briefly summarize the supervised learning procedure presented in the previous section 4.4.5, and the validation approach for the stress interpolation (4.43) discussed above. For each model, and in each of the 109 investigated triangulation points $\underline{\lambda} \in S_{\mathsf{T}}^{109}$, we conducted 5000 optimization runs for the minimization problem (4.41) and thus obtained the set S_{min} of minimizing parameter vectors $\underline{a}$. From this set S_{min}, we identified the single best parameter vector $\underline{a}^{\mathsf{min}} \in S_{\mathsf{min}}$ (4.42), which is associated with the smallest worst case loss of a model in a fixed triangulation point $\underline{\lambda}$. To study whether stress interpolation (4.43) can be used to generalize a model beyond points where the parameters $\underline{a}^{\mathsf{min}}$ are available, we designated the 45 points $\underline{\lambda}^{\mathsf{F}} \in S_{\mathsf{T}}^{\mathsf{F}}$ as fitting points and the 64 points $\underline{\lambda}^{\mathsf{V}} \in S_{\mathsf{T}}^{\mathsf{V}}$ as validation points. On these points $\underline{\lambda}^{\mathsf{F}}$ and $\underline{\lambda}^{\mathsf{V}}$, we compute the validation error e_{V} (4.45) using the stress interpolation procedure defined through the equations (4.43) and (4.44),

such that only the parameter vectors $\underline{a}^{\min}$ in the fitting points are used. Finally, to investigate whether a model captures the underlying material behavior appropriately, how stress interpolation affects the prediction quality, and how the prediction quality varies over the fiber orientation triangle S_T, we are interested in the error measures $\mathcal{L}^{\max}$, $e_\mathsf{V}^{\max}$, $e_\mathsf{V}^{\text{mean}}$, and $e_\mathsf{V}^{\bar{\boldsymbol{D}}}$. Thus, we list the largest Loss $\mathcal{L}^{\max}$, as well as the validation errors $e_\mathsf{V}^{\max}$, and $e_\mathsf{V}^{\text{mean}}$ in Table 4.5, visualize the validation error $e_\mathsf{V}^{\bar{\boldsymbol{D}}}$ over the fiber orientation triangle S_T in Figure 4.5, and discuss the errors in the following.

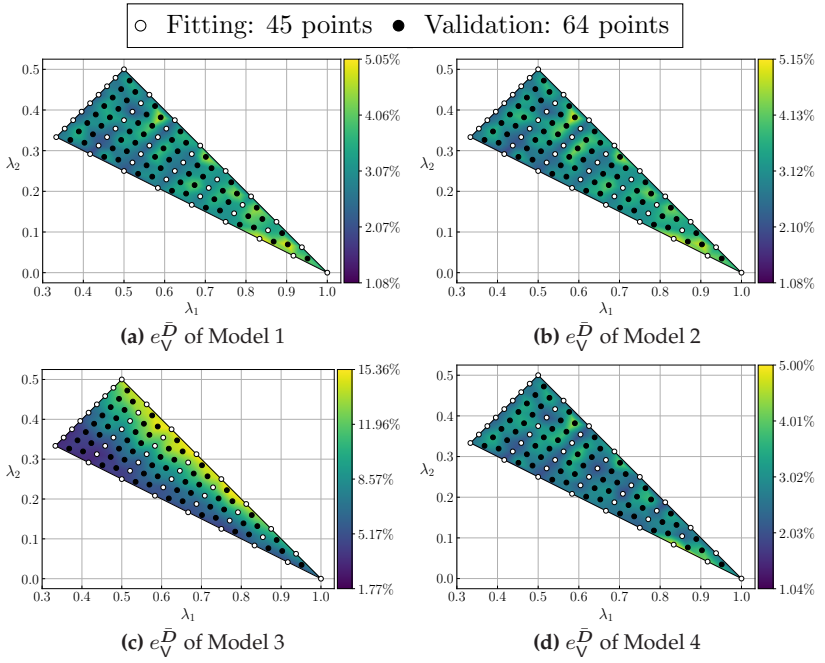

(a) $e_\mathsf{V}^{\bar{\boldsymbol{D}}}$ of Model 1 **(b)** $e_\mathsf{V}^{\bar{\boldsymbol{D}}}$ of Model 2

(c) $e_\mathsf{V}^{\bar{\boldsymbol{D}}}$ of Model 3 **(d)** $e_\mathsf{V}^{\bar{\boldsymbol{D}}}$ of Model 4

Figure 4.5: Validation error $e_\mathsf{V}^{\bar{\boldsymbol{D}}}$ over the fiber orientation triangle S_T for Models 1 to 4. Figure adapted from Sterr et al. (2024b, Figure 5).

	Model 1	Model 2	Model 3	Model 4
$\mathcal{L}^{\max}$ in %	5.00	5.00	15.36	5.00
$e_{\mathrm{V}}^{\max}$ in %	5.05	5.15	15.36	5.00
$e_{\mathrm{V}}^{\mathrm{mean}}$ in %	2.65	2.73	7.76	2.28

Table 4.5: Largest loss $\mathcal{L}^{\max}$, as well as validation errors $e_{\mathrm{V}}^{\max}$, and $e_{\mathrm{V}}^{\mathrm{mean}}$ for the Models 1 to 4. Table adapted from Sterr et al. (2024b, Table 5).

Model 1 and Model 2 differ only in their modeling approach for the viscosity tensor $\bar{\mathbb{V}}_0(\underline{b})$, where the parameter based construction of an orthogonal tensor $\bar{\mathbb{V}}_0(\underline{b}) = \mathbb{A}(\underline{b})$ in Model 1 is replaced by the scalar relationship (4.37) in Model 2. This reduction in dimensionality does not increase the loss $\mathcal{L}$, as the largest loss $\mathcal{L}^{\max}$ for both Model 1 and Model 2 is 5.00%. Also, the largest validation error $e_{\mathrm{V}}^{\max} = 5.15\%$ and mean validation error $e_{\mathrm{V}}^{\mathrm{mean}} = 2.73\%$ of Model 2 are only 0.10% and 0.08% larger than the errors $e_{\mathrm{V}}^{\max} = 5.05\%$ and $e_{\mathrm{V}}^{\mathrm{mean}} = 2.65\%$ of Model 1. Hence, the scalar relationship defined by equation (4.37) appears to be a valid assumption in the context of the investigated physics and microstructures. The largest loss $\mathcal{L}^{\max}$ occurred for the orientation state $\underline{\lambda} = (0.83, 0.08)^{\mathsf{T}}$ for both Model 1 and Model 2. In contrast, the largest validation errors $e_{\mathrm{V}}^{\max}$ occurred at orientation states $\underline{\lambda} = (0.90, 0.07)^{\mathsf{T}}$ for Model 1 and $\underline{\lambda} = (0.59, 0.38)^{\mathsf{T}}$ for Model 2. For the chosen discretization of the fiber orientation triangle S_{T}, a small additional error is introduced by stress interpolation, as shown by the slight differences between the largest losses $\mathcal{L}^{\max}$ and the largest validation errors $e_{\mathrm{V}}^{\max}$ for Model 1 and Model 2. Among the investigated models, Model 3 shows the largest loss and the largest validation error with $\mathcal{L}^{\max} = 15.36\%$ and $e_{\mathrm{V}}^{\max} = 15.36\%$, occurring at the orientation state $\underline{\lambda} = (0.69, 0.31)^{\mathsf{T}}$. For orientation states towards the lower and left edges of the fiber orientation triangle S_{T}, the magnitude of the validation error $e_{\mathrm{V}}^{\bar{D}}$ for Model 3 is comparable to that of the other models, see Figure 4.5. However, a mean validation error $e_{\mathrm{V}}^{\mathrm{mean}} = 7.76\%$ in combination with the relatively large validation

errors $e_{\mathsf{V}}^{\bar{D}}$ occurring at orientation states towards the upper edge of the fiber orientation triangle S_{T} indicate that equation (4.38) is not a sufficiently accurate approximation over the whole fiber orientation triangle S_{T}. For the most general model, Model 4, the largest loss $\mathcal{L}^{\mathsf{max}}$ and the largest validation error $e_{\mathsf{V}}^{\mathsf{max}}$ are both 5.00% for the orientation state $\underline{\lambda} = (0.83, 0.08)^{\mathsf{T}}$. Hence, the increased anisotropic capability of Model 4 improves the quality of fit and prediction only slightly compared to Models 1 and 2, albeit Model 4 uses more parameters. The mean validation error $e_{\mathsf{V}}^{\mathsf{mean}} = 2.28\%$ of Model 4 is also only 0.37% and 0.45% lower than for Models 1 and 2. In summary, Model 3 performed the worst among the investigated models and Model 4 performed the best. The orientation averaging incorporated in Model 3 reduced the prediction accuracy, while the anisotropic function $\mathbb{T}^{(2)}$ improved the prediction accuracy of Model 4. However, Models 1 and 2 use fewer parameters than Model 4 and show rather similar prediction accuracy. Consequently, the degree of anisotropic non-linearity encoded in Model 1 and Model 2 seems to be sufficient to capture the effective viscous behavior to engineering accuracy in the investigated load cases. In terms of practical implementation, computational efficiency and balanced prediction accuracy we consider Model 2 the best of the investigated models, since it uses a moderate amount of parameters and yields accuracy comparable to Model 4.

4.5 Conclusions

In this chapter, we used supervised machine learning and FFT-based computational techniques to discover models for the effective suspension viscosity of fiber suspensions with shear-thinning matrix behavior. We first extended the computational investigations of previous work to a broad variety of fiber orientation states. For all considered orientation states, we studied the anisotropy and shear rate dependence of the

suspension viscosity over a wide range of shear rates of engineering interest. Confirming previous observations in the case of a transversely isotropic orientation state, we found that the anisotropy of the suspension viscosity for a particular orientation state varies substantially depending on the load direction and shear rate. Furthermore, the degree of non-linearity of the matrix material in the studied volume elements influences the anisotropy of the suspension viscosity strongly. Based on the observed material behavior, we introduced four requirements a model of the suspension viscosity should satisfy, and formulated four model candidates according to these requirements. Using supervised machine learning techniques for non-convex optimization, we identified the model parameters based on the high-fidelity FFT-based computational results, and found that three of the four presented models achieve validation errors below 5.15 %. One model containing an approximation of the suspension viscosity based on superposition and orientation averaging did not perform favorably when compared with the other presented models.

Chapter 5

Deep material networks for fiber suspensions with infinite material contrast[1]

5.1 Introduction

For composites with kinematically unconstrained solid phases, the literature presented in section 1.2.4 provides compelling evidence for the accuracy and versatility of (direct) DMNs. However, the (direct) DMN architecture has yet to be applied to composites involving fluids or infinite material contrast, which is required for suspensions of rigid fibers. Because (direct) DMNs are based on laminates of solids, the treatment of fluids with a DMN architecture requires a different type of building block. Additionally, treatment of infinite material contrast with DMNs is challenging, because the rank-one laminates of a DMN have singular effective properties if one of the phases is singular, i.e., rigid. Therefore, the singular effective properties of the rank-one laminates may propagate through the whole DMN during the training and evaluation processes, rendering the effective properties of the DMN singular as

[1] This chapter is based on the sections 1 to 5 of the publication "Deep material networks for fiber suspensions with infinite material contrast" (Sterr et al., 2024b).

well. In this chapter we address these issues and propose an architecture to treat suspensions of rigid fibers.

We extend the direct DMN architecture for kinematically unconstrained solid phases with finite material contrast to an architecture that is able to treat suspensions of rigid fibers. In particular, this task requires the treatment of fluid phases and infinite material contrast. We name this architecture the Flexible DMN (FDMN) architecture. To treat fluid materials with FDMNs, we derive homogenization blocks for layered emulsions that are governed by Stokes flow, and consist of possibly incompressible phases with finite material contrast. In section 5.2.1, we establish that the velocity field in this type of layered material is phase-wise affine, if the dissipation potentials of the phases are strictly rank-one convex. We use this result and follow an analytical procedure described by Milton (2002, §9) to derive the closed form linear homogenization function of the considered layered emulsions in section 5.2.2. To treat infinite material contrast, we study a particular type of layered material, namely, coated layered materials (CLMs), in section 5.2.3. We obtain closed form homogenization functions for CLMs with kinematically unconstrained or incompressible phases. With the objective of using CLMs as FDMN building blocks in the presence of rigid fibers, we derive conditions for the required number of layering directions and their orientation, such that the effective properties of CLM are non-singular. We do so for CLMs with incompressible and rigid phases.

In section 5.3, we present the FDMN architecture as an extension of the (direct) DMN architecture. An FDMN arises by replacing the rank-one laminates of a (direct) DMN with rank-one layered materials capable of treating fluids, and non-singular CLMs capable of treating infinite material contrast. Also, we discuss the material sampling, the offline training procedure, as well as the online evaluation of FDMNs in the context of incompressible rigid fiber suspensions. We apply FDMNs to predict the viscous response of fiber polymer suspensions in section 5.4,

demonstrating both the ability to handle incompressible fluid phases and infinite material contrast. We use FFT-based computational homogenization techniques to generate linear training data and non-linear validation data for shear-thinning fiber suspensions with a Cross-type matrix behavior, and a fiber volume fraction of 25%. We consider 31 different fiber orientation states and a variety of incompressible elongational and shear flows. Using the computational data, we train FDMNs for all fiber orientation states, and study the prediction accuracy of the FDMNs in the non-linear case. For all investigated load cases and microstructures, the FDMNs achieve validation errors below 4.31% over a wide range of shear rates relevant to engineering processes. Not considering the time required to generate the training data and to train an FDMN, the FDMNs achieve speedup factors between 11785 and 17225 compared to FFT-based computations. Finally, we compare the prediction accuracy of the FDMN based approach with a different machine learning approach by Sterr et al. (2024b), and find that FDMNs offer better accuracy and flexibility at a higher computational cost for the considered material and flow scenarios.

5.2 Homogenization of layered emulsions with infinite material contrast

5.2.1 Phase-wise affine displacement and velocity fields in laminates and emulsions

Like for (direct) DMNs, the building blocks of an FDMN should admit linear homogenization functions in closed form, and there should exist efficient solution schemes to compute the stress response of the building blocks in case their phases are non-linear. In analogy to the laminate based architecture of the (direct) DMN, we thus consider

layered emulsions as the building blocks of the FDMN architecture. Like laminates, layered emulsions consist of multiple, possibly nonlinear, fluid materials, that are arranged such that every phase boundary between the phases is orthogonal to the layering direction $\boldsymbol{n} \in \mathcal{S}^2$, on the 2-sphere $\mathcal{S}^2$. For the offline training and the online evaluation of an FDMN with layered emulsions as building blocks, knowing the homogenization functions of layered emulsions with linear and nonlinear phases is necessary. Primarily, we look for similarities between the homogenization of layered emulsions and solid laminates that can be leveraged. In laminates, the displacement fields are phase-wise affine, and we wish to know if the velocity fields in layered emulsions belong to a particular class of fields as well. If the velocity fields are phase-wise affine, established solution techniques on (direct) DMN architectures (Gajek et al., 2020) can be employed for the online evaluation of the FDMN, and convenient linear homogenization equations can be employed for the offline training. We follow a procedure detailed by Kabel et al. (2016b) on the homogenization of laminates, and establish the existence and uniqueness of phase-wise affine velocity fields in a particular type of emulsion. We consider a K-phase layered emulsion with layering direction $\boldsymbol{n}$, which, similar to a laminate, is constructed by arranging K-phases so that the direction $\boldsymbol{n}$ is orthogonal to all phase boundaries. The emulsion occupies a rectangular and periodic volume $Y \subset \mathbb{R}^3$, and consists of non-Newtonian phases with rank-one convex dissipation potential $\Psi_k : (\mathbb{R}^3)^{\otimes 2} \to \mathbb{R}$, such that

$$\Psi_k(\boldsymbol{L} + \beta \boldsymbol{a} \otimes \boldsymbol{b}) \leq \beta \Psi_k(\boldsymbol{L} + \boldsymbol{a} \otimes \boldsymbol{b}) + (1 - \beta)\Psi_k(\boldsymbol{L}), \\ \forall\, \beta \in [0, 1],\, \boldsymbol{a}, \boldsymbol{b} \in \mathbb{R}^3 \backslash \{\boldsymbol{0}\}, \tag{5.1}$$

where $\boldsymbol{L} \in (\mathbb{R}^3)^{\otimes 2}$ denotes the velocity gradient, and the operator $(\cdot)^{\otimes a}$ constructs a tensor space of a-th order. Also, $Y_k \subset Y$ denotes the sub

volume of the k-th phase, and the phases do not intersect, i.e.,

$$Y_j \cap Y_k = \varnothing \quad \text{if} \quad j \neq k, \tag{5.2}$$

and form the volume Y, such that

$$Y = \bigcup_{j=1}^{K} Y_j. \tag{5.3}$$

Let the operator $\langle\cdot\rangle_Y$ denote volume averaging of a quantity over a volume Y, i.e.,

$$\langle\cdot\rangle_Y \equiv \frac{1}{|Y|}\int_Y (\cdot)\,\mathrm{d}Y(\boldsymbol{x}) \quad \text{with} \quad |Y| \equiv \int_Y \mathrm{d}Y(\boldsymbol{x}). \tag{5.4}$$

Then, we express the velocity field $\boldsymbol{v} : Y \to \mathbb{R}^3$ as

$$\boldsymbol{v} = \bar{\boldsymbol{L}}\boldsymbol{x} + \hat{\boldsymbol{v}}, \quad \text{with} \quad \langle\nabla\hat{\boldsymbol{v}}\rangle_Y = \boldsymbol{0}, \tag{5.5}$$

where $\bar{\boldsymbol{L}} \in (\mathbb{R}^3)^{\otimes 2}$ stands for the prescribed effective velocity gradient and $\hat{\boldsymbol{v}}$ is the velocity fluctuation field. Accordingly, the periodic dissipation potential function $\Psi : Y \times (\mathbb{R}^3)^{\otimes 2} \to \mathbb{R}$ of the emulsion is defined through

$$\Psi(\boldsymbol{x}, \nabla^{\mathrm{s}}\boldsymbol{v}) = \sum_{i}^{K} \chi_k(\boldsymbol{x})\Psi_k(\boldsymbol{x}, \nabla^{\mathrm{s}}\boldsymbol{v}), \tag{5.6}$$

where $\chi_k : Y \to \{0, 1\}$ refers to the characteristic function of the sub volume Y_k, and ∇^{s} stands for the symmetrized gradient. Let the flow inside the emulsion be governed by Stokes flow, i.e., the advectorial forces in the layered emulsion are small in contrast to the viscous forces, then the steady state balance of mass

$$\operatorname{div}(\rho\boldsymbol{v}) = 0, \tag{5.7}$$

where $\rho : Y :\to \mathbb{R}$ denotes the mass density field, is satisfied. Additionally, the stress field

$$\boldsymbol{\sigma} = \mathcal{S}(\cdot, \bar{\boldsymbol{D}} + \nabla^s \hat{\boldsymbol{v}}) \tag{5.8}$$

in terms of the effective strain rate tensor $\bar{\boldsymbol{D}} = (\bar{\boldsymbol{L}} + \bar{\boldsymbol{L}}^{\mathsf{T}})/2$, and the associated stress operator $\mathcal{S}$ on the space of symmetric second order tensors $\mathsf{Sym}(3) \subset (\mathbb{R}^3)^{\otimes 2}$ (Edelen, 1973)

$$\mathcal{S} : Y \times \mathsf{Sym}(3) \to \mathsf{Sym}(3), \tag{5.9}$$

$$(\boldsymbol{x}, \boldsymbol{D}) \mapsto \frac{\partial \Psi}{\partial \boldsymbol{D}}(\boldsymbol{x}, \boldsymbol{D}), \tag{5.10}$$

satisfies the balance of linear momentum without inertial effects and volume forces

$$\operatorname{div}(\boldsymbol{\sigma}) = \boldsymbol{0}. \tag{5.11}$$

Therefore, the effective response of the emulsion is obtained from the minimization problem

$$\left\langle \Psi(\boldsymbol{x}, \bar{\boldsymbol{D}} + \nabla^{\mathsf{s}} \hat{\boldsymbol{v}}) \right\rangle_Y \longrightarrow \min_{\hat{\boldsymbol{v}} \in \mathcal{A}}, \tag{5.12}$$

where $\mathcal{A}$ stands for the admissible set

$$\mathcal{A} = \left\{ \hat{\boldsymbol{v}} : Y \to \mathbb{R}^3 \quad \middle| \quad \operatorname{div}(\rho \boldsymbol{v}) = 0 \quad \text{and} \quad \langle \nabla \hat{\boldsymbol{v}} \rangle_Y = \boldsymbol{0} \right\} \tag{5.13}$$

Hence, assuming there is no slip between the phases, the proof by Kabel et al. (2016b, §2) extends to layered emulsions with finite material contrast. Therefore, if the dissipation potentials Ψ_k are strictly rank-one convex, there exists a unique minimizer $\hat{\boldsymbol{v}}$ in the class of phase-wise affine velocity fields. As a special case, this is also true for incompressible Stokes flows, for which the balance of mass simplifies to

$$\operatorname{div}(\boldsymbol{v}) = 0. \tag{5.14}$$

In the following, we use the term *layered emulsion* only for the type of emulsion defined above.

5.2.2 Two-phase layered emulsions with Newtonian phases

Similar to two-phase laminates of linear elastic solid materials, we wish to find a convenient closed form expression for the linear homogenization function of two-phase layered emulsions. With the goal of using layered emulsions as building blocks of an FDMN, we dedicate this section to deriving such a closed form expression for two-phase layered emulsions with kinematically unconstrained or incompressible Newtonian phases. For this purpose, we employ the results of the previous section 5.2.1, and extend an existing homogenization approach for two-phase laminates of linear elastic phases by Milton (2002, §9). To emphasize the link between the linear homogenization of laminates and layered emulsions we define the class of linear materials $\mathcal{M}$, and study layered materials of solids and fluids in parallel. A material m_k in the class of linear materials $\mathcal{M}$ is characterized by the primal material tensor $\mathbb{M}_k$ or its dual tensor $\mathbb{K}_k \equiv \mathbb{M}_k^{-1}$, such that

$$(\mathbb{M}_k, \mathbb{K}_k) \in \{(\mathsf{M}^+)^2, (\mathsf{M}_0^+)^2\}. \tag{5.15}$$

Here, the convex cones $\mathsf{M}^+ \subset (\mathbb{R}^3)^{\otimes 4}$ and $\mathsf{M}_0^+ \subset (\mathbb{R}^3)^{\otimes 4}$ comprise all fourth order tensors $\boldsymbol{X} \in (\mathbb{R}^3)^{\otimes 4}$, which are positive definite on the vector spaces of symmetric second order tensors $\mathsf{Sym}(3)$ and traceless symmetric second order tensors $\mathsf{Sym}_0(3) \subset \mathsf{Sym}(3)$, respectively. Additionally, a tensor $\mathbb{X} \in \{\mathsf{M}^+, \mathsf{M}_0^+\}$ has minor and major symmetries

$$\mathbb{X} = \mathbb{X}^{\mathsf{T}_\mathsf{H}} = \mathbb{X}^{\mathsf{T}_\mathsf{L}} = \mathbb{X}^{\mathsf{T}_\mathsf{R}}, \tag{5.16}$$

and a tensor $\mathbb{X} \in \mathsf{M}_0^+$ maps the second order unit tensor $\boldsymbol{I}$ to zero, such that

$$\ker \mathbb{X} = \boldsymbol{I}, \quad \text{i.e.,} \quad \mathbb{X}[\boldsymbol{I}] = \boldsymbol{0}. \tag{5.17}$$

Here, we define the map $\mathbb{T}[\boldsymbol{Y}]$ in component form and in the standard basis of $\mathbb{R}^3$ as

$$\mathbb{T}[\boldsymbol{Y}] \mathrel{\hat{=}} T_{ijkl} Y_{kl}, \quad \text{for some} \quad \boldsymbol{Y} \in (\mathbb{R}^3)^{\otimes 2}, \mathbb{T} \in (\mathbb{R}^3)^{\otimes 4}. \tag{5.18}$$

Any material $m_k \in \mathcal{M}$ follows the linear constitutive equations

$$\boldsymbol{\sigma}^{co} = \mathbb{M}_k[\nabla^{\mathsf{s}} \boldsymbol{w}] \quad \text{and} \quad \nabla^{\mathsf{s}} \boldsymbol{w} = \mathbb{K}_k[\boldsymbol{\sigma}^{co}], \tag{5.19}$$

if the material m_k is not subjected to kinematic constraints, or the constitutive equation

$$\boldsymbol{\sigma}^{ico} = \boldsymbol{\tau} - p\boldsymbol{I} = \mathbb{M}_k[\nabla^{\mathsf{s}} \boldsymbol{w}] - p\boldsymbol{I}, \quad \text{and} \quad \nabla^{\mathsf{s}} \boldsymbol{w} = \mathbb{K}_k[\boldsymbol{\tau}], \tag{5.20}$$

if the material m_k is incompressible. Here, $\boldsymbol{w}$ denotes the field associated with the type of material m_k, i.e., the displacement field $\boldsymbol{u}$ for linear elastic solids or the velocity field $\boldsymbol{v}$ for linearly viscous fluids. For the constitutive equation (5.20) we use an additive split of the stress field $\boldsymbol{\sigma}$

$$\boldsymbol{\sigma} = \boldsymbol{\tau} - p\boldsymbol{I}, \tag{5.21}$$

into the deviatoric stress field $\boldsymbol{\tau} : Y \to \mathsf{Sym}_0(3)$ and the pressure field $p : Y \to \mathbb{R}$. Here, we use $Y \subset \mathbb{R}^3$ to denote the volume occupied by a two-phase layered material, i.e., a laminate or a layered emulsion, and $Y_1, Y_2 \subset Y$ to denote the volume occupied by the two phases $m_1, m_2 \in \mathcal{M}$ of the layered material. We define the effective properties $(\bar{\mathbb{M}}, \bar{\mathbb{K}}) \in \{(\mathsf{M}^+)^2, (\mathsf{M}_0^+)^2\}$ of the layered material in the sense of the Hill-Mandel condition (Hill, 1963; Mandel, 1966)

$$\langle \boldsymbol{\sigma} \cdot \nabla^{\mathsf{s}} \boldsymbol{w} \rangle_Y = \langle \boldsymbol{\sigma} \rangle_Y \cdot \langle \nabla^{\mathsf{s}} \boldsymbol{w} \rangle_Y \equiv \bar{\mathbb{M}} \cdot (\langle \nabla^{\mathsf{s}} \boldsymbol{w} \rangle_Y \otimes \langle \nabla^{\mathsf{s}} \boldsymbol{w} \rangle_Y). \tag{5.22}$$

Then, for perfectly bonded laminates of linear solid materials without kinematic constraints, a closed form expression for the primal or dual effective properties of the laminate $\bar{\mathbb{A}} \in \{\bar{\mathbb{M}}, \bar{\mathbb{K}}\}$ can be derived using the procedure detailed by Milton (2002, §9), such that

$$\Big(\big(\bar{\mathbb{A}} - \mathbb{A}_0\big)^{-1} + \mathbb{\Gamma}_{\mathbb{A}_0}(\boldsymbol{n})\Big)^{-1} = \Big\langle \Big((\mathbb{A}(\boldsymbol{x}) - \mathbb{A}_0)^{-1} + \mathbb{\Gamma}_{\mathbb{A}_0}(\boldsymbol{n}) \Big)^{-1} \Big\rangle . \tag{5.23}$$

Here, the inverse is taken on the space M^+ in which $\bar{\mathbb{A}} \in \mathsf{M}^+$ lives, $\mathbb{A} : Y \to \mathsf{M}^+$ denotes the field of the phase wise primal or dual material properties

$$\mathbb{A} : Y \to \mathsf{M}^+, \quad \boldsymbol{x} \mapsto \begin{cases} \mathbb{A}_1 & \text{if } \boldsymbol{x} \in Y_1, \\ \mathbb{A}_2 & \text{if } \boldsymbol{x} \in Y_2, \end{cases} \tag{5.24}$$

and $\mathbb{A}_0 \in \mathsf{M}^+$ refers to an arbitrary reference material tensor such that the term $(\mathbb{A}(\boldsymbol{x}) - \mathbb{A}_0)$ is invertible. Also, the operator $\mathbb{\Gamma}_{\mathbb{A}_0}(\boldsymbol{n}) \in (\mathbb{R}^3)^{\otimes 4}$ is defined as

$$\mathbb{\Gamma}_{\mathbb{A}_0}(\boldsymbol{n}) = \mathbb{\Gamma}_{\mathbb{I}}(\boldsymbol{n}) \left[\mathbb{\Gamma}_{\mathbb{I}}(\boldsymbol{n}) \mathbb{A}_0 \mathbb{\Gamma}_{\mathbb{I}}(\boldsymbol{n})\right]^{\dagger} \mathbb{\Gamma}_{\mathbb{I}}(\boldsymbol{n}), \tag{5.25}$$

where $(\cdot)^{\dagger}$ stands for the Moore–Penrose pseudoinverse, and the operators $\mathbb{\Gamma}_{\mathbb{A}_0}(\boldsymbol{n})$ and $\mathbb{\Gamma}_{\mathbb{I}}(\boldsymbol{n})$ project onto the same subspace with respect to different inner products. More specifically, the operator $\mathbb{\Gamma}_{\mathbb{A}_0}(\boldsymbol{n})$ is an orthogonal projector with respect to the $\mathbb{A}_0$-weighted inner product

$$\langle \boldsymbol{X}, \boldsymbol{X} \rangle_{\mathbb{A}_0} = \boldsymbol{X} \cdot \mathbb{A}_0[\boldsymbol{X}], \quad \boldsymbol{X} \in \mathsf{Sym}(3), \tag{5.26}$$

and the operator $\mathbb{\Gamma}_{\mathbb{I}}(\boldsymbol{n})$ is an orthogonal projector with respect to the Frobenius inner product

$$\langle \boldsymbol{X}, \boldsymbol{X} \rangle_{\mathsf{F}} = \boldsymbol{X} \cdot \mathbb{I}[\boldsymbol{X}] = \boldsymbol{X} \cdot \boldsymbol{X}, \quad \boldsymbol{X} \in \mathsf{Sym}(3), \tag{5.27}$$

where $\mathbb{I} \in (\mathbb{R}^3)^{\otimes 4}$ denotes the fourth order identity tensor. The operator $\mathbb{\Gamma}_{\mathbb{I}}(\boldsymbol{n})$ encodes restrictions imposed by the periodicity of the laminate, the perfect bonding of the phases, the momentum balance (5.11), and the constitutive equation (5.19). Depending on whether we wish to compute the effective primal or the effective dual properties of the laminate, a different operator $\mathbb{\Gamma}_{\mathbb{I}}(\boldsymbol{n})$ is required. For the homogenization of the primal effective properties, i.e., $\bar{\mathbb{A}} = \bar{\mathbb{M}}$, the operator $\mathbb{\Gamma}_{\mathbb{I}}(\boldsymbol{n})$ equals the operator $\mathbb{\Gamma}_1^{\mathsf{co}}(\boldsymbol{n})$. For the homogenization of the dual effective properties, i.e., $\bar{\mathbb{A}} = \bar{\mathbb{K}}$, the operator $\mathbb{\Gamma}_{\mathbb{I}}(\boldsymbol{n})$ equals the operator $\mathbb{\Gamma}_2^{\mathsf{co}}(\boldsymbol{n})$. The operators $\mathbb{\Gamma}_1^{\mathsf{co}}$ and $\mathbb{\Gamma}_2^{\mathsf{co}}$, are defined through their action on a second order tensor $\boldsymbol{X} \in \mathsf{Sym}(3)$

$$\mathbb{\Gamma}_1^{\mathsf{co}}(\boldsymbol{n})[\boldsymbol{X}] = 2(\boldsymbol{X}\boldsymbol{n}) \otimes_{\mathsf{s}} \boldsymbol{n} - (\boldsymbol{n} \cdot \boldsymbol{X}\boldsymbol{n})\boldsymbol{n} \otimes \boldsymbol{n} \tag{5.28}$$

and

$$\mathbb{\Gamma}_2^{\mathsf{co}}(\boldsymbol{n})[\boldsymbol{X}] = \boldsymbol{X} - \mathbb{\Gamma}_1^{\mathsf{co}}(\boldsymbol{n})\boldsymbol{X}, \tag{5.29}$$

where $\otimes_{\mathsf{s}}$ denotes the symmetrized dyadic product. The operators $\mathbb{\Gamma}_1^{\mathsf{co}}$ and $\mathbb{\Gamma}_2^{\mathsf{co}}$ project onto the subspaces

$$\mathcal{E}^{\mathsf{co}} = \left\{ \mathsf{Sym}(3) \ni \boldsymbol{X} = \boldsymbol{d} \otimes \boldsymbol{n} + \boldsymbol{n} \otimes \boldsymbol{d} \quad \middle| \quad \boldsymbol{d} \in \mathbb{R}^3 \right\} \tag{5.30}$$

and

$$\mathcal{S}^{\mathsf{co}} = \left\{ \mathsf{Sym}(3) \ni \boldsymbol{X} \quad | \quad \boldsymbol{X}\boldsymbol{n} = \boldsymbol{0} \right\}, \tag{5.31}$$

and arise from the fact that the jumps of the field $[\![\nabla^{\mathsf{s}} \boldsymbol{w}]\!] \in \mathcal{E}^{\mathsf{co}}$

$$[\![\nabla^{\mathsf{s}} \boldsymbol{w}]\!] = [\![\nabla \boldsymbol{w}\, \boldsymbol{n}]\!] \otimes_{\mathsf{s}} \boldsymbol{n}, \tag{5.32}$$

and the jump of the stress $[\![\boldsymbol{\sigma}]\!] \in \mathcal{S}^{\mathsf{co}}$ live on mutually orthogonal subspaces (Milton, 2002, §9), because it holds that

$$[\![\boldsymbol{\sigma}\boldsymbol{n}]\!] = \boldsymbol{0}. \tag{5.33}$$

Interestingly, the constitutive equations for kinematically unconstrained linear elastic solids and linearly viscous fluids share the same structure, see equation (5.19). Additionally, equations (5.32) and (5.33) are satisfied for layered emulsions by definition, because there is no slip between the phases, and the momentum balance (5.11) is satisfied. Thus, the homogenization problem for the considered layered emulsions has the same structure as the homogenization problem for laminates. As a result, the effective properties $\bar{\mathbb{A}} \in \mathsf{M}^+$ of a two-phase layered emulsion of kinematically unconstrained materials $m_1, m_2 \in \mathcal{M}$ can be computed with equation (5.23). If the kinematic field $\boldsymbol{w}$ is solenoidal such that the incompressible balance of mass (5.14) is satisfied, it follows from equation (5.32) that

$$[\![\nabla^{\mathsf{s}} \boldsymbol{w}\, \boldsymbol{n}]\!] \cdot \boldsymbol{n} = 0. \tag{5.34}$$

Also, if the materials $m_1, m_2 \in \mathcal{M}$ are incompressible, it follows from equations (5.21) and (5.33) that

$$[\![\boldsymbol{\sigma}\boldsymbol{n}]\!] = \boldsymbol{0} \quad \Longleftrightarrow \quad [\![\boldsymbol{\tau}\boldsymbol{n}]\!] = [\![p]\!]\boldsymbol{n}. \tag{5.35}$$

Therefore, the jumps $[\![\nabla^{\mathsf{s}}\boldsymbol{w}]\!] \in \mathcal{E}^{\mathsf{ico}}$ and $[\![\boldsymbol{\sigma}]\!] \in \mathcal{S}^{\mathsf{ico}}$ live in the mutually orthogonal spaces

$$\mathcal{E}^{\mathsf{ico}} = \left\{ \mathsf{Sym}_0(3) \ni \boldsymbol{X} = 2\,\boldsymbol{d} \otimes_{\mathsf{s}} \boldsymbol{n} - 2(\boldsymbol{d}\cdot\boldsymbol{n})\boldsymbol{n}\otimes\boldsymbol{n} \quad \middle| \quad \boldsymbol{d} \in \mathbb{R}^3 \right\} \tag{5.36}$$

and

$$\mathcal{S}^{\mathsf{ico}} = \left\{ \mathsf{Sym}_0(3) \ni \boldsymbol{X} \quad \middle| \quad \boldsymbol{X}\boldsymbol{n} = a\boldsymbol{n}, \quad a \in \mathbb{R} \right\}. \tag{5.37}$$

The two operators $\mathbb{I}_1^{\mathsf{ico}}(\boldsymbol{n})$ and $\mathbb{I}_2^{\mathsf{ico}}(\boldsymbol{n})$, defined through their action on a traceless second order tensor $\boldsymbol{X} \in \mathsf{Sym}_0(3)$,

$$\mathbb{I}_1^{\mathsf{ico}}(\boldsymbol{n})[\boldsymbol{X}] = 2(\boldsymbol{X}\boldsymbol{n}) \otimes_{\mathsf{s}} \boldsymbol{n} - 2(\boldsymbol{n}\cdot\boldsymbol{X}\boldsymbol{n})\boldsymbol{n}\otimes\boldsymbol{n} \tag{5.38}$$

and

$$\mathbb{I}_2^{\mathsf{ico}}(\boldsymbol{n})[\boldsymbol{X}] = \boldsymbol{X} - \mathbb{I}_2^{\mathsf{ico}}(\boldsymbol{n})[\boldsymbol{X}], \tag{5.39}$$

project onto the spaces $\mathcal{E}^{\text{ico}}$ and $\mathcal{S}^{\text{ico}}$, respectively. Consequently, the procedure detailed in Milton (2002) can be used to compute the effective properties $\bar{\mathbb{A}} \in \mathsf{M}_0^+$ of a layered material with incompressible constituents. In this context the homogenization equation (5.23) applies if the property field $\mathbb{A} : Y :\to \mathsf{M}_0^+$, the reference properties $\mathbb{A}_0 \in \mathsf{M}_0^+$, and the operator $\mathbb{\Gamma}_{\mathbb{I}}(\boldsymbol{n}) \in (\mathbb{\Gamma}_1^{\text{ico}}(\boldsymbol{n}), \mathbb{\Gamma}_2^{\text{ico}}(\boldsymbol{n}))$ are selected based on whether the tensor $\bar{\mathbb{A}}$ represents primal or dual effective properties. In summary, for a layered material consisting of linear materials $m_1, m_2 \in \mathcal{M}$, the effective material properties $(\bar{\mathbb{M}}, \bar{\mathbb{K}}) \in \{(\mathsf{M}^+)^2, (\mathsf{M}_0^+)^2\}$ can be computed with the homogenization equation (5.23). The choice of the operator $\mathbb{\Gamma}_{\mathbb{I}}(\boldsymbol{n})$ depends on whether the phases are compressible or incompressible, and whether the primal or dual effective tensors are sought.

5.2.3 Coated layered materials

Because we are interested in building FDMNs for suspensions of rigid particles, the architecture of the FDMN should be capable of handling infinitely viscous, i.e., rigid, phases. In this section, we leverage the homogenization equation (5.23) to study the homogenization of repeatedly layered materials in the presence of rigid phases. We define and use the term *rank* of a layered material in the following to better distinguish between the possible ways to construct layered materials. The rank $R \in \mathbb{N}_{\geq 0}$ of a hierarchical, layered material defines the number of layering steps that are needed to construct the material using layering directions $\boldsymbol{n}_r \in \mathcal{S}^2$, such that the index r starts at one and ends at R, i.e., $r \in \{1, ..., R\}$. By definition, a rank-0 layered material is simply a single phase material without any layering. Also, the materials that are layered at each layering step need not be the same. For example, let the first layer in a rank-2 layered material consist of the materials m_1 and m_2. Then, the second layer may consist of the materials m_1 and m_2 in the form of the first layer, and a third material m_3.

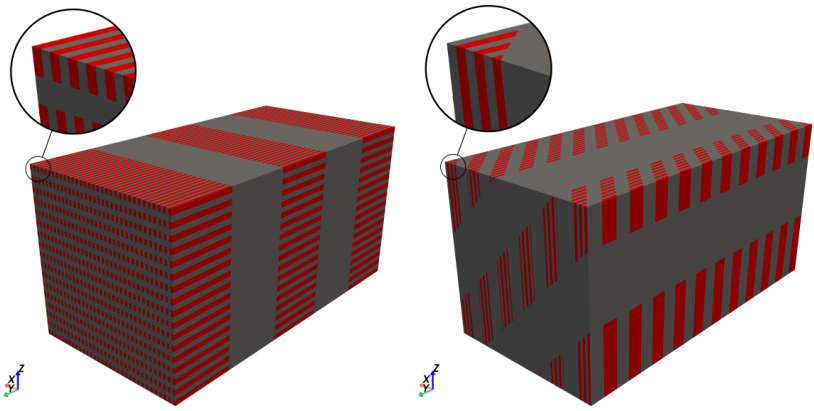

(a) Orthogonal layering directions **(b)** Non-orthogonal layering directions

Figure 5.1: Rank-three, coated layered materials with orthogonal layering directions (a), and non-orthogonal layering directions (b). The core material is shown in red and the coating material is shown in gray. We hint at the separation of length scales between the material layers through our choice of the layer thicknesses. Figure adapted from Sterr et al. (2024a, Figure 1).

Rank-one two-phase layered materials are unsuitable as DMN building blocks in the case of infinite material contrast, because their effective properties are always singular if one phase is singular. In search of a building block capable of handling rigid phases, we study the effective properties of a particular type of layered material following the terminology and the analytical approach detailed by Milton (2002, §9). We refer to this particular type of layered materials as coated layered materials (CLMs). To construct a CLM, one material m_2, called the coating, is repeatedly layered onto another material m_1, called the core. The layering process is divided into multiple steps, such that the r-th layering step is applied in direction $\boldsymbol{n}_r$, and the total number of layering steps equals the rank R of the CLM. As an example, two rank-three CLMs are depicted in Figure 5.1, where the layering directions $\boldsymbol{n}_r \in \mathcal{N}_1$

of the material shown in Figure 5.1a are

$$\mathcal{N}_1 = \left\{(1,0,0)_{\{\boldsymbol{e}_i\}}, (0,0,1)_{\{\boldsymbol{e}_i\}}, (0,1,0)_{\{\boldsymbol{e}_i\}}\right\}, \tag{5.40}$$

and the layering directions $\boldsymbol{n}_r \in \mathcal{N}_2$ of the material shown in Figure 5.1b are

$$\mathcal{N}_2 = \left\{(1,0,0)_{\{\boldsymbol{e}_i\}}, \frac{1}{\sqrt{2}}(1,1,0)_{\{\boldsymbol{e}_i\}}, \frac{1}{\sqrt{2}}(1,0,1)_{\{\boldsymbol{e}_i\}}\right\}. \tag{5.41}$$

As described, the gray coating material m_2 is repeatedly applied in layers, such that for $r > 1$, the r-th sub layer of the rank-three CLM is constructed by layering a rank-$(r-1)$ layered material with the coating material m_2. By definition, the 0-th sub layer of the rank-three CLM is purely made of the core material m_1. We wish to compute the effective properties $\bar{\mathbb{A}}$ of a coated layered material by repeatedly applying the homogenization equation (5.23). For the recursive application of the rank-one homogenization formula (5.23) to be valid, the phases at each homogenization step must be homogeneous on the length scale of the respective layering step. This requires a separation of length scales, in the sense that the thickness δ_r of the material sections in the rank-r sub layer is drastically smaller than the thickness δ_{r+1} of the material sections in the next sub layer, i.e., $\delta_r \ll \delta_{r+1}$. In Figure 5.1, we hint at this separation of length scales between the material layers through our choice of the layer thicknesses. Nonetheless, we retain a visible degree of inhomogeneity, so that the layer structures can be distinguished for illustration purposes.

Before we repeatedly apply equation (5.23) to derive an expression for the effective properties $\bar{\mathbb{A}}$, we first simplify the expression (5.23) for the case at hand. We let the reference material properties $\mathbb{A}_0$ in equation (5.23) approach the properties $\mathbb{A}_2$ of the coating material m_2,

resulting in the equation (Milton, 2002, §9)

$$(1 - f_2)(\bar{\mathbb{A}} - \mathbb{A}_2)^{-1} = (\mathbb{A}_1 - \mathbb{A}_2)^{-1} + f_2 \mathbb{\Gamma}_{\mathbb{A}_2}(\boldsymbol{n}). \tag{5.42}$$

Here, the coating material m_2 must not be rigid or a void, the tensor $(\mathbb{A}_1 - \mathbb{A}_2)$ must be invertible, and f_2 denotes the volume fraction of the coating material m_2. Also, the fourth order tensor $\mathbb{\Gamma}_{\mathbb{A}_2}(\boldsymbol{n}_r) \in (\mathbb{R}^3)^{\otimes 4}$ is defined by equation (5.25) as

$$\mathbb{\Gamma}_{\mathbb{A}_2}(\boldsymbol{n}_r) = \mathbb{\Gamma}_{\mathbb{I}}(\boldsymbol{n}_r) \left[\mathbb{\Gamma}_{\mathbb{I}}(\boldsymbol{n}_r)\mathbb{A}_2\mathbb{\Gamma}_{\mathbb{I}}(\boldsymbol{n}_r)\right]^{\dagger} \mathbb{\Gamma}_{\mathbb{I}}(\boldsymbol{n}_r), \tag{5.43}$$

where the inverse is taken on the subspace onto which $\mathbb{\Gamma}_{\mathbb{I}}$ projects. To compute the effective properties $\bar{\mathbb{A}}$ of a rank-R CLM, we recursively apply equation (5.42) for the effective material properties of rank-one layered materials, such that (Milton, 2002, §9)

$$(1 - f_2)(\bar{\mathbb{A}} - \mathbb{A}_2)^{-1} = (\mathbb{A}_1 - \mathbb{A}_2)^{-1} + f_2 \sum_{r=1}^{R} c_r \mathbb{\Gamma}_{\mathbb{A}_2}(\boldsymbol{n}_r). \tag{5.44}$$

Here, the scalars c_r are computed from the volume fractions $f_1^{(r)}$ of the core material m_1 in the rank-r sub layer of the rank-three CLM, such that

$$c_r = \frac{f_1^{(r-1)} - f_1^{(r)}}{f_2}, \tag{5.45}$$

i.e., the properties

$$\sum_{r=1}^{R} c_r = 1 \quad \text{and} \quad c_r > 0, \tag{5.46}$$

hold. Because the rank-0 sub layer consists solely of the core material m_1 by definition, the volume fraction $f^{(0)} = 1$ is one. Equation (5.44) is essential to compute the effective properties of layered materials with infinite material contrast, and thus for the treatment of such materials using a DMN architecture. In Appendix A, we employ equation (5.44)

to study the conditions under which the effective properties $\bar{\mathbb{A}}$ of a CLM are singular when the core material m_1 is rigid. With the objective of applying FDMNs to suspensions of rigid fibers in mind, we summarize the results pertaining to rank-R CLMs with a *rigid* core material m_1 and an *incompressible* coating material m_2 with the following statements.

1. The effective properties $\bar{\mathbb{A}}$ of a CLM of rank $R < 3$ are always singular.
2. For rank-3 CLMs, the effective properties $\bar{\mathbb{A}}$ are singular if at least one layering direction is orthogonal to two other layering directions, or if at least two layering directions are collinear.
3. Rank-3 CLMs with mutually non-orthogonal and mutually non-collinear layering directions $\boldsymbol{n}_1, \boldsymbol{n}_2$, and $\boldsymbol{n}_3$ have non-singular effective properties. Thus, in the context of this thesis, we require

$$0 < |\boldsymbol{n}_1 \cdot \boldsymbol{n}_2| < 1, \quad 0 < |\boldsymbol{n}_1 \cdot \boldsymbol{n}_3| < 1, \quad 0 < |\boldsymbol{n}_2 \cdot \boldsymbol{n}_3| < 1. \tag{5.47}$$

The statements 1-3 are of critical importance for the treatment of incompressible suspensions of rigid particles using a DMN architecture. It follows that CLMs with an incompressible coating material and rigid core material should be at least of rank $R = 3$ and have non-collinear and mutually non-orthogonal layering directions to be non-singular. Therefore, we leverage such non-singular-singular rank-3 CLMs in the FDMN architecture to treat suspensions of rigid fibers, as we explain in section 5.3.2.

5.3 Identifying deep material networks for suspensions of rigid fibers

5.3.1 Architecture of direct deep material networks

Because the FDMN architecture extends the (direct) DMN framework, we briefly summarize the direct DMN architecture in this section, before presenting the FDMN architecture in the next section 5.3.2. For in depth discussions and explanations of the direct DMN architecture, we refer the reader to articles by Gajek et al. (2020; 2021; 2022). A two-phase direct DMN is defined as a perfect binary tree, consisting of two-phase laminates $\mathcal{B}_k^i$ as nodes, see Figure 5.2a. The laminates $\mathcal{B}_k^i$ are defined by a single lamination direction $\boldsymbol{n}_k^i$ and two volume fractions $c_{k,1}^1$ and $c_{k,1}^2$. The DMN tree is ordered, rooted and has depth K. We use the letter $k = 1, ..., K$ to denote the depth of a node and the letter $i = 1, ..., 2^{k-1}$ to indicate the horizontal position of a node in the respective layer. We

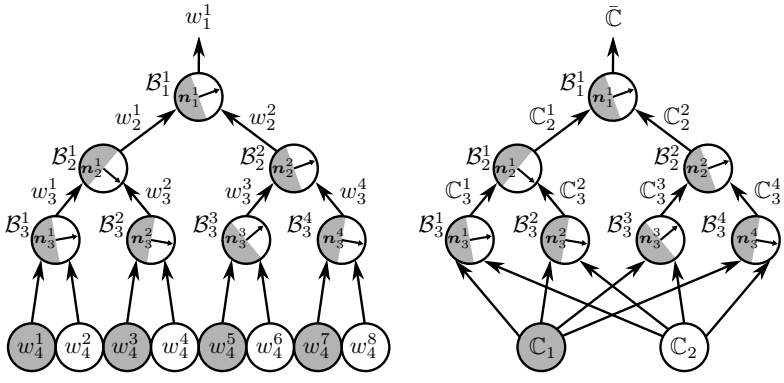

(a) Weight propagation **(b)** Stiffness propagation

Figure 5.2: Weight and stiffness propagation (from the bottom to the top) in a two-phase direct DMN (Gajek et al., 2021) of depth K = 3, by Gajek et al. (2022, Fig. 1), licensed under CC BY 4.0

parametrize a direct DMN by the two vectors $\underline{n} \in (\mathbb{R}^3)^{2^K-1}$

$$\underline{n} = (\boldsymbol{n}_K^1, ..., \boldsymbol{n}_K^{2^{K-1}}, \boldsymbol{n}_{K-1}^1, ..., \boldsymbol{n}_{K-1}^{2^{K-2}}, ..., \boldsymbol{n}_1^1), \tag{5.48}$$

and $\underline{w} \in \mathbb{R}^{2^K}$

$$\underline{w} = (w_{K+1}^1, ..., w_{K+1}^{2^K}). \tag{5.49}$$

Instead of the laminate volume fractions, the direct DMN is parametrized in terms of the weights w_{K+1}^i to improve numerical stability during the training process (Liu et al., 2019b; Liu and Wu, 2019). The i-th weight in the k-th layer is computed from the pairwise summation of the weights in the previous layer $k+1$, see Figure 5.2a, such that

$$w_k^i = w_{k+1}^{2i-1} + w_{k+1}^{2i}, \tag{5.50}$$

and the volume fractions $c_{k,1}^i$ and $c_{k,2}^i$ follow from

$$c_{k,1}^i = \frac{w_{k+1}^{2i-1}}{w_{k+1}^{2i-1} + w_{k+1}^{2i}}, \quad \text{and} \quad c_{k,2}^i = 1 - c_{k,1}^i. \tag{5.51}$$

Additionally, the weights w_{K+1}^i need to be positive and sum to unity, such that

$$w_{K+1}^i \geq 0 \quad \text{and} \quad \sum_i^{2^K} w_{K+1}^i = 1. \tag{5.52}$$

The vectors $\underline{n}$ and $\underline{w}$ fully parametrize a direct DMN of depth K and are identified by fitting the linear homogenization function of the DMN to the linear homogenization function of the microstructure of interest. The fitting process is carried out by using supervised machine learning, and we refer to this process as *offline training*. To evaluate the linear homogenization function of the DMN during the offline training, input stiffness pairs are propagated through the network of homogenization blocks $\mathcal{B}_k^i$, see Figure 5.2b. Consequently, if the stiffness $\mathbb{C}_k^i$ of a homogenization block $\mathcal{B}_k^i$ is singular, this singular stiffness can propagate

through the whole DMN, which is undesirable for the offline training. Once the parameter vectors $\underline{n}$ and $\underline{w}$ are known, they remain unchanged and are used in the *online evaluation* to predict the non-linear response of the studied material. In sections 5.3.4, 5.4.2, and 5.3.5, we discuss the offline training and the online evaluation for the proposed FDMN architecture.

5.3.2 Architecture of flexible deep material networks

With the results of the previous sections 5.2.1-5.2.3 at hand, we present an extended DMN architecture that is able to treat fluid phases and infinite material contrast. Compared to the architecture of (direct) DMNs shown in Figure 5.2, the lowest layer of laminates is replaced by a layer of rank-R CLMs $\mathcal{C}_R$, see Figure 5.3. The rank R of the CLM $\mathcal{C}_R$ and the

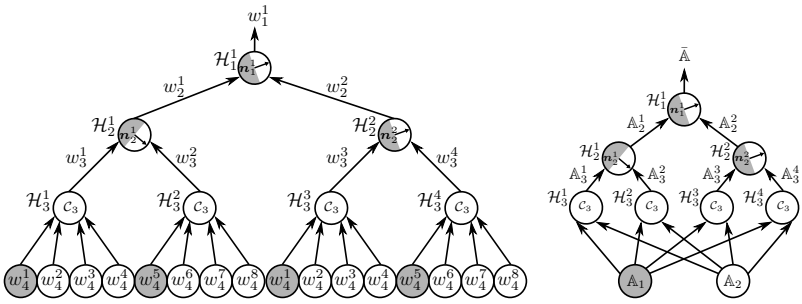

(a) Weight propagation

(b) Material tensor propagation

Figure 5.3: Weight and material property propagation (from the bottom to the top) in a two-phase FDMN (Gajek et al., 2021) of depth $K = 3$ with rank-3 CLMs. Figure adapted from Sterr et al. (2024a, Figure 3).

restrictions on its layering directions $\boldsymbol{n}_r$ are problem dependent, and chosen such that the non-singularity condition (A.11) is satisfied. This guarantees that only non-singular material tensors $\mathbb{A}_k^i$ are propagated

through the network. If all phases are kinematically unconstrained, solid, and non-singular, rank-one CLMs can be employed to recover the direct DMN architecture. However, in the case of incompressible suspensions of rigid particles, the CLMs are of rank $R = 3$ and have mutually non-collinear and non-orthogonal layering directions $\boldsymbol{n}_r$, as per statements 1-3. Additionally, the homogenization blocks $\mathcal{H}_k^i$ implement the general homogenization function defined by equation (5.23) in which the projector function $\mathbb{\Gamma}_{\mathbb{I}}$ depends on the physics of the investigated problem. This allows the treatment of composites consisting of linear materials $m \in \mathcal{M}$, including incompressible linearly viscous fluids. For problems involving two-phase materials, $R + 1$ weights and two materials are assigned to each CLM. The number of layering directions N_{n} and the number of input weights N_{w} in a two-phase FDMN of depth K with rank-R CLMs are

$$N_{\mathsf{n}} = 2^{K-1}(R+1) - 1, \quad N_{\mathsf{w}} = 2^{K-1}(R+1). \tag{5.53}$$

As an example, Figures 5.3a and 5.3b show the weight and material property propagation of a two-phase FDMN of depth $K = 3$ with two-phase CLMs of rank $R = 3$ as bottom layer. Of the four weights of a rank-3 CLM, one is associated with the core material m_1, and three are associated with the coating material m_2. This doubles the number of weights for an FDMN with rank-3 CLMs as compared to a DMN of the same depth K. Additionally, each rank-3 CLM block $\mathcal{C}_3$ has three layering directions $\boldsymbol{n}_r$ instead of one layering direction like rank-one laminates. To reduce the number of free parameters and ensure the CLMs are non-singular, the relative angles between the layering directions $\boldsymbol{n}_r$ are fixed, while their joint orientation in space is determined through the offline training, as we explain in section 5.3.4 in more detail. Because CLMs are based on the repeated layering of rank-one layered materials, an FDMN of depth K can be considered to be a special case of a (direct) DMN of depth $K+(R-1)$ with generalized

homogenization blocks. Then, a CLM represents a subtree of the DMN of depth $K + (R - 1)$, in which the weights w_k^i of certain phases are set to zero, such that a CLM emerges, see Figure 5.4. In particular,

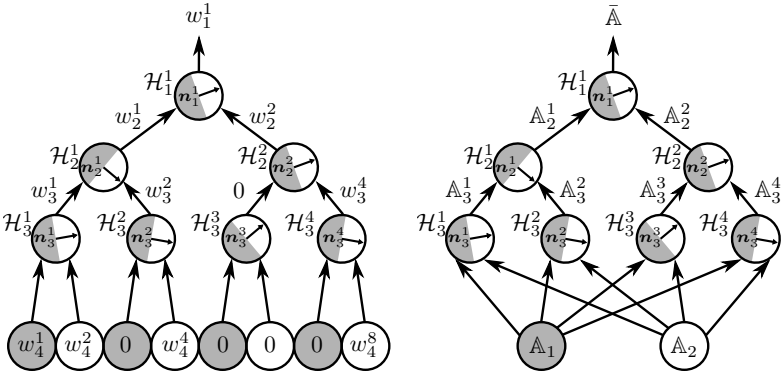

(a) Weight propagation **(b)** Material tensor propagation

Figure 5.4: Weight and material property propagation (from the bottom to the top) in a two-phase DMN of depth $K = 3$, representing a two-phase rank-3 CLM. Figure adapted from Sterr et al. (2024a, Figure 4).

except for one phase, the weights associated with the singular core material m_1 are set to zero. Additionally, R weights associated with the non-singular coating material m_2 must be non-zero, such that the rank R of the CLM is maintained. Technically, (direct) DMNs are therefore able to treat infinite material contrast intrinsically. However, the weights w_k^i need to be identified during the offline training, and might not always have appropriate values to generate CLMs with the required rank, such that singular material tensors $\mathbb{A}_k^i$ might propagate through the whole DMN. Also, if the layering normals are not chosen appropriately, the singular material properties may propagate through the whole DMN as well. Controlling the weights and normals via the implementation of the CLM blocks instead of learning them is therefore preferable to

prevent singularities during the offline training. Furthermore, FDMNs of depth K have fewer free parameters compared to equivalent DMNs of depth $K + R - 1$, which aids in the offline training as well.

Hypothetically, the presented FDMN architecture could be applied to problems with more than two phases as well. Let N_R denote the number of non-singular phases and N_S denote the number of singular phases. Then, for each singular phase, the FDMN needs to contain at least one CLM to which the phase is assigned, and which has non-singular effective properties. This requires a minimum of N_S CLMs. Additionally, the coatings of the CLMs can be constructed by mixing the non-singular phases, possibly by constructing N_R-phase layered materials. However, the application of FDMNs to materials with voids or more than two phases is beyond the scope of this thesis, because we focus on suspensions of rigid fibers.

5.3.3 Material sampling

For materials with solid phases, DMNs are trained by sampling the linear elastic homogenization function of the microstructure of interest with randomly generated input materials (Liu et al., 2019b; Liu and Wu, 2019; Gajek et al., 2021; 2022), and fitting the DMN parameters to replicate the desired homogenization function. Similarly, in the case of rigid particles suspended in viscous media, we train FDMNs to learn the linear viscous homogenization function with the goal of predicting non-linear viscous behavior. Consequently, we sample the linear viscous homogenization function by using randomly generated, linearly viscous input materials. We base our sampling strategy on the approach used by Gajek et al. (2021). In the article by Gajek et al. (2021) on glass fiber reinforced polyamide composites, the authors chose the stiffness samples for the fiber material to be isotropic, and the stiffness samples for to the polyamide matrix to be transversely isotropic. This strategy leads to a smaller sample space compared to sampling orthotropic stiffnesses

for both the fiber and the matrix materials, as suggested by Liu et al. (2019b) and Liu and Wu (2019). To reduce the computational cost of sampling even further for the considered case of fiber suspension, we only generate sample viscosities for the matrix material and consider the suspended fibers to be rigid in all computations. To generate samples for the matrix material, we follow Gajek et al. (2021) and choose the sample viscosity $\mathbb{V}^s$ pertaining to the s-th sample to be transversely isotropic, such that

$$\mathbb{V}^s = 2\eta_2 \left(\mathbb{P}_2 - g \boldsymbol{A}'(\underline{a}) \otimes \boldsymbol{A}'(\underline{a}) \right), \tag{5.54}$$

where the scalar $g \in [0, 1)$ defines the magnitude of the perturbation by the unitary and deviatoric tensor $\boldsymbol{A}'(\underline{a}) \in \mathsf{Sym}_0(3)$, the vector $\underline{a} \in \mathbb{R}^4$ collects four angles, and we consider the scalar viscosities

$$\eta_2 = 10^p \mathrm{GPa}, \quad p \in [-3, 3]. \tag{5.55}$$

For a fiber reinforced polyamide, Gajek et al. (2021) employed an ansatz of the form (5.54) to sample the material tangents of a J2-elastoplastic matrix material. Similarly, with the objective of applying FDMNs to fiber suspensions with a shear-thinning polyamide matrix as detailed in section 5.4.1, we use equation (5.54) to sample the material tangents of a Cross-type (3.2) matrix material. The tensor function $\boldsymbol{A}'$ is defined by an eigenvalue decomposition (Gajek et al., 2021)

$$\boldsymbol{A}' : \mathbb{R}^4 \to \mathsf{Sym}_0(3), \tag{5.56}$$

$$(a_1, a_2, a_3, a_4)^\mathsf{T} \mapsto \boldsymbol{Q}(a_2, a_3, a_4) \boldsymbol{A}(a_1) \boldsymbol{Q}(a_2, a_3, a_4)^\mathsf{T}, \tag{5.57}$$

into the orthogonal tensor $\boldsymbol{Q}(a_2, a_3, a_4)$ and a diagonal tensor $\boldsymbol{A}(a_1)$ in terms of the vector $\underline{a} = (a_1, a_2, a_3, a_4)^\mathsf{T}$. The tensor $\boldsymbol{A}(a_1)$ is constructed

from the angle a_1 via (Gajek et al., 2021)

$$\boldsymbol{A} = \frac{1}{\sqrt{\frac{\xi_1+1}{2\,\xi_1+1}}}\mathbf{diag}\left(\xi_2\cos\left(a_1\right), \xi_2\sin\left(a_1\right), \frac{1}{\sqrt{2}}\right), \tag{5.58}$$

$$\xi_1 = \cos\left(a_1\right)\sin\left(a_1\right), \quad \xi_2 = \frac{-\sqrt{2}}{2\cos\left(a_1\right)+2\sin\left(a_1\right)}, \tag{5.59}$$

and the tensor $\boldsymbol{Q}(a_2, a_3, a_4)$ represents a rotation around the direction $\boldsymbol{n}$, such that

$$\boldsymbol{Q}(a_2, a_3, a_4) : \mathbb{R}^3 \to \mathbb{R}^3 \tag{5.60}$$

$$\boldsymbol{x} \mapsto \cos\left(a_2\right)\boldsymbol{x} + \sin\left(a_2\right)\boldsymbol{n}\times\boldsymbol{x} + (1-\cos\left(a_2\right))(\boldsymbol{n}\cdot\boldsymbol{x})\boldsymbol{n}, \tag{5.61}$$

$$\boldsymbol{n} = \sin\left(a_3\right)\cos\left(a_4\right)\boldsymbol{e}_1 + \sin\left(a_3\right)\sin\left(a_4\right)\boldsymbol{e}_2 + \cos\left(a_3\right)\boldsymbol{e}_3. \tag{5.62}$$

Here, the operator **diag** constructs a second order tensor in the standard basis $\boldsymbol{e}_i$ of $\mathbb{R}^3$, and the components of the vector $\underline{a}$ live on the intervals

$$a_1 \in [0, 2\pi], \quad a_2 - \sin(a_2) \in [0, \pi], \quad a_3 \in [0, \pi], \quad a_4 \in [0, 2\pi]. \tag{5.63}$$

We sample the space of the variables p and $\underline{a}$ using the scrambled Sobol sequence (Owen, 1998; Sobol, 1967), and employ an FFT-based computational procedure to compute the resulting effective viscosities $\bar{\mathbb{V}}^s$ (Bertóti et al., 2021; Sterr et al., 2023), see section 5.4.

5.3.4 Offline training

Using the material sampling procedure described in the previous section 5.3.3, we wish to optimize the parameters of the FDMN with regard to the training data set. For the case of rigid fibers suspended in viscous media, we consider FDMNs with rank-3 CLMs as bottom layer, which satisfy the requirements derived in section A.2. We collect all layering

directions of the FDMN in a vector

$$\underline{n} = (\boldsymbol{n}_K^1, ..., \boldsymbol{n}_K^{3(2^{K-1})}, \boldsymbol{n}_{K-1}^1, ..., \boldsymbol{n}_{K-1}^{2^{K-2}}, ..., \boldsymbol{n}_2^1, \boldsymbol{n}_2^2, \boldsymbol{n}_1^1), \tag{5.64}$$

where we used the fact that the k-th layer contains 2^{k-1} normals if $k < K$, and the K-th layer contains $3(2^{K-1})$ normals. Because the homogenization blocks in the K-th layer are rank-three CLMs, the number of normals is different from the other layers. Each normal $\boldsymbol{n}_k^i$ in the k-th layer for $k < K$ is constructed using two angles a_k^i and b_k^i via

$$\boldsymbol{n}_k^i = \sin\left(b_k^i\right)\cos\left(a_k^i\right)\boldsymbol{e}_1 + \sin\left(b_k^i\right)\sin\left(a_k^i\right)\boldsymbol{e}_2 + \cos\left(b_k^i\right)\boldsymbol{e}_3. \tag{5.65}$$

However, for the normals $\boldsymbol{n}_K^i$ in the K-th layer, the procedure is different. To avoid singular effective properties during the evaluation of the FDMN in accordance with the discussion in sections 5.2.3 and A.2, we ensure that the three layering normals of a rank-three CLM block are not mutually non-orthogonal and mutually non-collinear as follows. First, for each rank-three CLM block $\mathcal{C}_3^i$, we compute the components Q_{op}^i of the orthogonal tensor $\boldsymbol{Q}^i$ in the standard basis $\{\boldsymbol{e}_i\}$ using three Euler angles $c_K^i, d_K^i, e_K^i \in [0, 2\pi]$ via

$$Q_{op}^i = G_{om}^i T_{mn}^i W_{np}^i \tag{5.66}$$

$$G_{om}^i = \begin{bmatrix} 1 & 0 & 0 \\ 0 & \cos\left(c_K^i\right) & -\sin\left(c_K^i\right) \\ 0 & \sin\left(c_K^i\right) & \cos\left(c_K^i\right) \end{bmatrix}, \tag{5.67}$$

$$T_{mn}^i = \begin{bmatrix} \cos\left(d_K^i\right) & 0 & \sin\left(d_K^i\right) \\ 0 & 1 & 0 \\ -\sin\left(d_K^i\right) & 0 & \cos\left(d_K^i\right) \end{bmatrix}, \tag{5.68}$$

$$W_{np}^i = \begin{bmatrix} \cos\left(e_K^i\right) & -\sin\left(e_K^i\right) & 0 \\ \sin\left(e_K^i\right) & \cos\left(e_K^i\right) & 0 \\ 0 & 0 & 1 \end{bmatrix}. \tag{5.69}$$

Then, we compute the layering directions $\boldsymbol{n}_K^{3(i-1)+1}$, $\boldsymbol{n}_K^{3(i-1)+2}$, $\boldsymbol{n}_K^{3(i-1)+3}$ of the rank-three CLM $\mathcal{C}_3^i$ via

$$\boldsymbol{n}_K^{3(i-1)+1} = \boldsymbol{q}_1^i, \tag{5.70}$$

$$\boldsymbol{n}_K^{3(i-1)+2} = \frac{1}{\sqrt{2}} \left(\boldsymbol{q}_1^i + \boldsymbol{q}_2^i \right), \tag{5.71}$$

$$\boldsymbol{n}_K^{3(i-1)+3} = \frac{1}{\sqrt{2}} \left(\boldsymbol{q}_1^i + \boldsymbol{q}_3^i \right), \tag{5.72}$$

where $\boldsymbol{q}_1^i$, $\boldsymbol{q}_2^i$, and $\boldsymbol{q}_3^i$ are the first, second, and third column vectors of the tensor $\boldsymbol{Q}^i$ in the standard basis $\boldsymbol{e}_i$, respectively. This leads to a total of N_α angles with

$$N_\alpha = 5 \left(2^{K-1} \right) - 2. \tag{5.73}$$

The angles between the layering directions are fixed for each CLM $\mathcal{C}_3$, but the three layering directions are rotated together during training. Other procedures than the one presented here are viable as well, as long as the constructed vectors $\boldsymbol{n}_K^{3(i-1)+1}$, $\boldsymbol{n}_K^{3(i-1)+2}$, and $\boldsymbol{n}_K^{3(i-1)+3}$ are mutually non-collinear and non-orthogonal. Alternatively, one could parametrize each of the three layering directions $\boldsymbol{n}_K^{3(i-1)+1}$, $\boldsymbol{n}_K^{3(i-1)+2}$, and $\boldsymbol{n}_K^{3(i-1)+3}$ with two angles each, and identify the angles independently. Then, the effective properties of the CLM $\mathcal{C}_3^i$ are non-singular almost surely, because the probability of any two of the three layering directions being collinear or one vector being orthogonal to the other two is zero. However, parametrizing each of the three layering directions with two angles requires twice the amount of angles in the CLM layer of the FDMN as compared to the presented procedure.

To define the linear homogenization function of the FDMN, we collect all N_α angles of the layering directions in the vector $\underline{\alpha}$

$$\begin{aligned} \underline{\alpha} = (&c_K^1, d_K^1, e_K^1, ..., c_K^{3(2^{K-1})}, d_K^{3(2^{K-1})}, e_K^{3(2^{K-1})}, \\ &a_{K-1}^1, b_{K-1}^1, ..., a_{K-1}^{2^{K-2}}, b_{K-1}^{2^{K-2}}, ..., a_1^1, b_1^1), \end{aligned} \tag{5.74}$$

and collect all N_{w} input weights of the FDMN in the vector

$$\underline{w} = (w_{K+1}^1, ..., w_{K+1}^{N_{\mathsf{w}}}). \tag{5.75}$$

We follow Gajek et al. (2020) and define the loss function $\mathcal{L} : \mathbb{R}^{\otimes N_\alpha} \times \mathbb{R}^{\otimes N_{\mathsf{w}}} \to \mathbb{R}$ in terms of the linear homogenization function $\mathcal{DMN}_{\mathsf{L}} : \mathcal{A} \times \mathcal{A} \times \mathbb{R}^{\otimes N_\alpha} \times \mathbb{R}^{\otimes N_{\mathsf{w}}} \to \mathcal{A}$ of the FDMN as

$$\begin{aligned}\mathcal{L}\left(\underline{\alpha}, \underline{w}\right) =& \frac{1}{N_{\mathsf{b}}} \sqrt[q]{\sum_{s=1}^{N_{\mathsf{b}}} \left(\frac{\left\| \bar{\mathbb{A}}^s - \mathcal{DMN}_{\mathsf{L}}\left(\mathbb{A}_1^s, \mathbb{A}_2^s, \underline{\alpha}, \underline{w}\right) \right\|_p}{\left\| \bar{\mathbb{A}}^s \right\|_p} \right)^q} + \\ & \lambda \left(\sum_{i=1}^{N_{\mathsf{w}}} w_{K+1}^i - 1 \right)^2,\end{aligned} \tag{5.76}$$

where N_{b} is the number of samples, $\mathbb{A}_1^s, \mathbb{A}_2^s \in \mathcal{A}$ denote the material tensors of the phases of a sample, and $\bar{\mathbb{A}}^s \in \mathcal{A}$ denotes the effective material tensor of a sample. Additionally, the class of material tensors $\mathcal{A} \in \{\mathsf{M}, \mathsf{M}_0\}$ depends on the considered problem, we follow Gajek et al. (2020) and choose the constants $p, q \in \mathbb{N}_{\geq 0}$ as $p = 1$ and $q = 10$, and the operator $\|\cdot\|_1$ refers to the ℓ^1-norm of the components in Mandel notation. The second summand in equation (5.76) encodes the simplex constraint on the weights of the DMN

$$\sum_{i=1}^{N_{\mathsf{w}}} w_{K+1}^i = 1, \quad \text{where} \quad w_{K+1}^i \geq 0, \tag{5.77}$$

in the form of a quadratic penalty term with the penalty parameter $\lambda > 0$. We implement the offline training in the Python programming language and use the machine learning framework PyTorch (Paszke et al., 2019) to identify the vectors $\underline{\alpha}$ and $\underline{w}$. To do so, we leverage the automatic differentiation capabilities of PyTorch to solve the minimization problem

$$\mathcal{L}\left(\underline{\alpha}, \underline{w}\right) \to \min_{\underline{\alpha}, \underline{w}}, \tag{5.78}$$

using the RAdam(Liu et al., 2019a) optimizer. We use mini batches of N_b samples to compute the parameter updates

$$\underline{\alpha}_{q+1} = \underline{\alpha}_q - \kappa_{q,\alpha} \frac{\partial \mathcal{L}}{\partial \underline{\alpha}}(\underline{\alpha}, \underline{w}), \quad \underline{w}_{q+1} = \underline{w}_q - \kappa_{q,w} \frac{\partial \mathcal{L}}{\partial \underline{w}}(\underline{\alpha}, \underline{w}) \tag{5.79}$$

for every epoch q. Also, we follow previous work (Liu et al., 2019b; Liu and Wu, 2019; Gajek et al., 2020) and use perfect binary trees without tree compression (Liu et al., 2019b; Liu and Wu, 2019; Gajek et al., 2021)

5.3.5 Online evaluation

In section 5.2.1, we showed that the velocity fields in layered emulsions are phase-wise affine, and thus the online evaluation procedure of direct DMNs can be employed for FDMNs as well if the phases are kinematically unconstrained. However, for FDMNs with incompressible phases, the online evaluation procedure needs to be adapted, as we discuss in the following. We define the linear operator $\underline{\underline{A}} : (\mathbb{R}^3)^{\otimes N_\mathsf{n}} \to (\mathsf{Sym}_0(3))^{N_\mathsf{w}}$ which maps the emulsion-wise jumps $\underline{b} \in (\mathbb{R}^3)^{\otimes N_\mathsf{n}}$ of the velocity gradient onto the phase-wise strain rate fluctuations. Also, we express the effective dissipation potential $\bar{\Psi} : (\mathsf{Sym}_0(3))^{N_\mathsf{w}} \to \mathbb{R}$ of the FDMN in terms of the phase-wise dissipation potentials $\Psi_i : \mathsf{Sym}_0(3) \to \mathbb{R}$, the respective weights w^i_{K+1}, and the phase-wise strain rate tensor $\boldsymbol{D}_i \in \mathsf{Sym}_0(3)$ as

$$\bar{\Psi}\left(\underline{\bar{D}} + \underline{\underline{A}}\,\underline{b}\right) = \sum_{i=1}^{N_\mathsf{w}} w^i_{K+1} \Psi_i(\boldsymbol{D}_i), \tag{5.80}$$

where all entries of the vector $\underline{\bar{D}} \in (\mathsf{Sym}_0(3))^{N_\mathsf{w}}$ equal the effective strain rate $\bar{\boldsymbol{D}}$, i.e.,

$$\underline{\bar{D}} = (\bar{\boldsymbol{D}}, \bar{\boldsymbol{D}}, ..., \bar{\boldsymbol{D}}). \tag{5.81}$$

Thus, the minimization problem for the online, non-linear evaluation of the FDMN is

$$\bar{\Psi}\left(\underline{\bar{D}} + \underline{\underline{A}}\,\underline{b}\right) \rightarrow \min_{\underline{b} \in (\mathbb{R}^3)^{\otimes N_\mathsf{n}}}, \tag{5.82}$$

and the Euler–Lagrange equation of the problem (5.82) reads

$$\frac{\partial \bar{\Psi}}{\partial \underline{b}}\left(\underline{\bar{D}} + \underline{\underline{A}}\,\underline{b}\right) = \underline{\underline{A}}^{\mathsf{T}} \frac{\partial \bar{\Psi}}{\partial \underline{D}}\left(\underline{\bar{D}} + \underline{\underline{A}}\,\underline{b}\right) = \underline{0}. \tag{5.83}$$

In terms of a weight matrix $\underline{\underline{W}} : (\mathsf{Sym}_0(3))^{N_\mathsf{w}} \rightarrow (\mathsf{Sym}_0(3))^{N_\mathsf{w}}$ defined by its action on a vector $\underline{d} \in (\mathsf{Sym}_0(3))^{N_\mathsf{w}}$

$$\underline{\underline{W}}\,\underline{d} = \left(w_{K+1}^1 d_1, w_{K+1}^2 d_2, ..., w_{K+1}^{N_\mathsf{w}} d_K\right), \tag{5.84}$$

we may write the Euler–Lagrange equation (5.83) as

$$\underline{\underline{A}}^{\mathsf{T}}\,\underline{\underline{W}}\,\underline{\tau}\left(\underline{\bar{D}} + \underline{\underline{A}}\,\underline{b}\right) = \underline{0}, \tag{5.85}$$

with the vector of phase wise stresses $\underline{\tau}\left(\underline{\bar{D}} + \underline{\underline{A}}\,\underline{b}\right) \in (\mathsf{Sym}_0(3))_\mathsf{w}^N$. Therefore, the jump vector $\underline{b}$ satisfying equation (5.85) is determined using a Newton scheme with the update rule

$$\underline{b}_{n+1} = \underline{b}_n + s_n \Delta \underline{b}_n, \tag{5.86}$$

containing the iteration count n, the backtracking factor s_n, and the update direction $\Delta \underline{b}_n$. The update direction $\Delta \underline{b}_n$ solves the linear system

$$\underline{\underline{H}}\Delta \underline{b}_n = \left(\underline{\underline{A}}^{\mathsf{T}}\,\underline{\underline{W}}\,\underline{\tau}\left(\underline{\bar{D}} + \underline{\underline{A}}\,\underline{b}\right)\underline{\underline{A}}\right)\Delta \underline{b}_n = \underline{\underline{A}}^{\mathsf{T}}\,\underline{\underline{W}}\,\underline{\tau}\left(\underline{\bar{D}} + \underline{\underline{A}}\,\underline{b}\right). \tag{5.87}$$

So far, the procedure is completely analogous to the approaches for (direct) DMNs presented in previous work (Gajek et al., 2020; 2021; 2022). However, in the case of incompressible phases, the matrix $\underline{\underline{A}}$ is symmetric but singular, and the solution of the equation system (5.87) is not unique. However, because of incompressibility, we know that the i-th entry $\boldsymbol{b}_i$

of the jump vector $\underline{b}$ is orthogonal to the i-th entry $\boldsymbol{n}_i$ of the vector of layering normals $\underline{n}$, i.e.,

$$\boldsymbol{b}_i \cdot \boldsymbol{n}_i = 0. \tag{5.88}$$

Hence, we construct the block diagonal matrix $\underline{\underline{N}} : (\mathbb{R}^3)^{\otimes N_\mathsf{n}} \to (\mathbb{R}^3)^{\otimes N_\mathsf{n}}$ consisting of N_w blocks $\boldsymbol{N}_i$ on the main diagonal, which are defined as

$$\boldsymbol{N}_i = \beta_i \boldsymbol{n}_i \otimes \boldsymbol{n}_i, \quad i \in \{1, ..., N_\mathsf{w}\} \tag{5.89}$$

with the constant $\beta_i \in \mathbb{R}_{>0}$. By definition, it holds that

$$\boldsymbol{N}_i \boldsymbol{b}_i = \boldsymbol{0}, \tag{5.90}$$

and the jump vector $\underline{b}$ is in the kernel of $\underline{\underline{N}}$, such that

$$\underline{\underline{N}}\, \underline{b} = \underline{0}. \tag{5.91}$$

Thus, we add equations (5.87) and (5.91), such that the solution $\Delta \underline{b}_n$ of the resulting update rule

$$\left(\underline{\underline{H}} + \underline{\underline{N}}\right) \Delta \underline{b}_n = \underline{\underline{A}}^\mathsf{T} \underline{\underline{W}}\, \underline{\tau} \left(\underline{\bar{D}} + \underline{\underline{A}}\, \underline{b}\right), \tag{5.92}$$

is unique. However, floating point precision may cause issues during the addition of the operators $\underline{\underline{H}}$ and $\underline{\underline{N}}$, if numbers of largely different magnitudes are summed. To remedy this issue, the scalars β_i need to be chosen according to the magnitude of the entries in the matrix $\underline{\underline{H}}$. Furthermore, some input weights w^i_{K+1} might become equal to, or close to zero during training, which might render the system matrix $(\underline{\underline{H}} + \underline{\underline{N}})$ ill-conditioned. Thus, it might be difficult to obtain accurate update directions $\Delta \underline{b}_n$ by solving equation (5.92). While it is generally possible to prune the FDMN tree (Liu and Wu, 2019) by removing phases with vanishing or almost vanishing volume fractions, this might collapse the rank-3 CLMs of the bottom FDMN layer into layered materials of

a lesser rank. In case of infinite material contrast, this could result in the propagation of singular effective properties through the FDMN. It is therefore preferable to work with possibly ill-conditioned systems and to employ appropriate methods for the solution of ill-conditioned systems (Neumaier, 1998). Alternatively, multiple FDMNs can be trained and the ones with the best online evaluation results can be selected. In this thesis, we follow the latter approach.

5.4 Application to rigid fibers suspended in polyamide 6

5.4.1 Material description and computational aspects

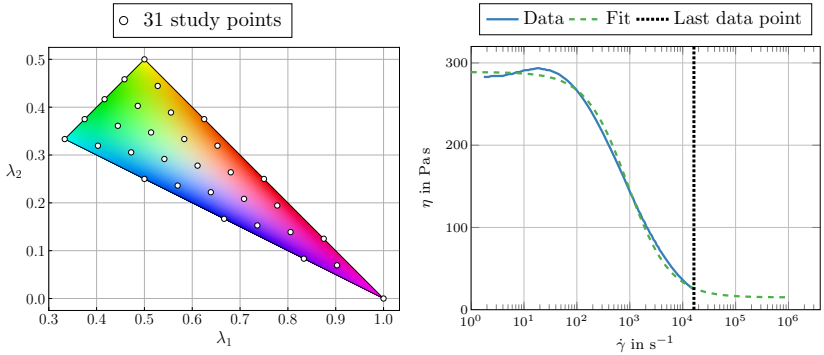

(a) Fiber orientation triangle S_T **(b)** Cross-type fit

Figure 5.5: Fiber orientation triangle S_T in CMYK coloring with 31 evaluation points (a), and material data with Cross-type fit for Ultramid®B3K (b). Figure adapted from Sterr et al. (2024a, Figure 5).

To generate the training data and the online validation data for the FDMN, we use FFT-based computational procedures to compute the

effective viscous response of fiber suspensions (Bertóti et al., 2021; Sterr et al., 2023). We generate the required fiber suspension microstructures using the sequential addition and migration method (Schneider, 2017) for 31 orientation states $\underline{\lambda}$ in the fiber orientation triangle S_T, see Figure 5.5a. For the visualization of the orientation triangle S_T, which is defined in equation (2.37), we follow Köbler et al. (2018), and use a CMYK coloring scheme. To keep the computational effort for computing the effective viscous responses feasible, we restrict to microstructures with a fiber volume fraction of 25%, and assign all fibers the length ℓ and the diameter d. Also, we set the aspect ratio $r_a = \ell/d$ of all fibers to 10, and use the results of Sterr et al. (2023) regarding the required resolution and size of the microstructure volume elements. Consequently, we choose a resolution of 15 voxels per fiber diameter, as well as cubic volume elements with edge size $L = 2.2\ell$. Regarding the matrix material, we build on the investigations in Sterr et al. (2023; 2024b), and prescribe a commercially available polyamide 6 (BASF, 2020) as the matrix material. As in the previous chapters 3 and 4, we use a Cross-type constitutive equation (3.2) with the material parameters collected in Table 4.1. Additionally, we investigate the same flow scenarios as in the previous chapters 3 and 4. More specifically, for all non-Newtonian considerations, we investigate the six load cases collected in the matrix $\underline{\underline{\bar{D}}}$ (3.35) for each macroscopic scalar shear rate $\dot{\gamma}$ in the set of studied shear rates $S_{\dot{\gamma}}$ (3.44). Consequently, the set $\bar{\boldsymbol{D}}_{\dot{\gamma}}$ of all investigated load cases is defined by the equations (3.35) and (3.44). Because the viscous stress inside the rigid fibers is, constitutively, not well-defined (Sterr et al., 2023), we employ a dual formulation of the associated homogenization problem for the FFT-based computations. We discretize the microstructures on a staggered grid (Harlow and Welch, 1965), and solve the resulting equation systems with the conjugate gradient method (CG) for linear computations, and with a Newton-CG approach for non-linear computations. With the goal of training an FDMN for each of the 31 fiber orientation states shown in Figure 5.5a,

we generate 32 sample viscosities with the procedure described in section 5.3.3, and compute the corresponding effective viscosities. To compute a single effective viscosity, five FFT-based computations are necessary (Bertóti et al., 2021), leading to a total of 4960 computations, and 992 computed effective viscosities. In the previous sections 5.2.3 and 5.3.2, we studied the linear homogenization functions of CLMs, and presented the FDMN architecture to treat infinite material contrast and incompressible materials. In the following, we discuss the material sampling for the offline training, the offline training procedure, and the online evaluation of FDMNs for suspensions of rigid particles.

5.4.2 Offline training

With the linear training data at hand, we wish to train FDMNs for the prediction of the non-Newtonian viscous behavior of shear-thinning fiber polymer suspensions. We follow previous work (Gajek et al., 2020; 2021) and choose the depth of the FDMN as $K = 8$ to achieve sufficient prediction quality for non-linear computations. An FDMN of depth $K = 8$ with CLMs of rank $R = 3$ has 512 weights and 638 angles as free parameters, as per equations (5.53) and (5.73). For each microstructure, we define the training data $\mathcal{S}^{\mathsf{D}}$ as

$$\mathcal{S}^{\mathsf{D}} = \{(\mathbb{V}_1^s, \mathbb{V}_F, \bar{\mathbb{V}}^s) \quad | \quad s \in (1, ..., 32)\}, \tag{5.93}$$

where $\mathbb{V}_1^s$ denotes the sample viscosities generated with equation (5.54), $\mathbb{V}_F$ denotes the infinite viscosity of the rigid fibers, and $\bar{\mathbb{V}}^s$ stands for the effective viscosity of the sample s. For each microstructure, we split the training data $\mathcal{S}^{\mathsf{D}}$ into the training set $\mathcal{S}^{\mathsf{t}} \subset \mathcal{S}^{\mathsf{D}}$ and the validation set $\mathcal{S}^{\mathsf{v}} \subset \mathcal{S}^{\mathsf{D}}$, which consist of 90% and 10% of the total training data, respectively. The training set $\mathcal{S}^{\mathsf{t}}$ and the validation set $\mathcal{S}^{\mathsf{v}}$ share no samples, i.e., $\mathcal{S}^{\mathsf{t}} \cap \mathcal{S}^{\mathsf{v}} = \varnothing$.

As an initial guess for the FDMN parameters, we uniformly sample all angles $\underline{\alpha}$ and weights $\underline{w}$ from their respective intervals, and rescale the weights $\underline{w}$ such that they sum to unity. Because we use a relatively small set of 32 samples as training data, we dedicate a large portion of it to the training set $\mathcal{S}^{\mathrm{t}}$, and choose to train 20 FDMNs per fiber orientation state $\underline{\lambda}$. Furthermore, we train the FDMNs on mini batches with size $N_{\mathrm{b}} = 8$, for which we draw randomly from the training set $\mathcal{S}^{\mathrm{t}}$. In case the last batch is smaller than eight samples, we drop the batch. Because the initialization of the parameter vectors $\underline{\alpha}$ and $\underline{w}$, as well as the offline training process are random, the FDMNs differ in their parameters and quality of fit. By training 20 FDMNs per fiber orientation state, we leverage this randomness with the goal of obtaining FDMNs with a high quality of fit. This strategy aims to reduce the total computational effort required to obtain sufficiently accurate FDMNs, because repeatedly training FDMNs on 32 samples requires less computational resources than conducting full field simulations for larger sample sizes. For the minimization of the loss function $\mathcal{L}$, we choose the RAdam algorithm (Liu et al., 2019a) and use a learning rate sweep (Smith and Topin, 2019) to determine the learning rates $\kappa_{0,\alpha}$ and $\kappa_{0,w}$. With the learning rate sweep we obtain highly similar learning rates for both parameter groups $\underline{\alpha}$ and $\underline{w}$, such that $\kappa_{0,\alpha} = \kappa_{0,w} = 1 \cdot 10^{-2}$. As the learning process advances, we use PyTorch's StepLR learning rate scheduler to improve convergence towards minima (Darken and Moody, 1990; Darken et al., 1992). To do so, we multiply the learning rates $\kappa_{0,\alpha}$ and $\kappa_{0,w}$ with a constant factor $f_{LR} = 0.75$ every 150 epochs. Other than the learning rates, we used standard hyperparameters for the two momentum coefficients $\beta_1 = 0.9$ and $\beta = 0.999$, as well as the stabilization constant $\varepsilon = 10^{-8}$. Overall, we train every FDMNs for a total of 2000 epochs each.

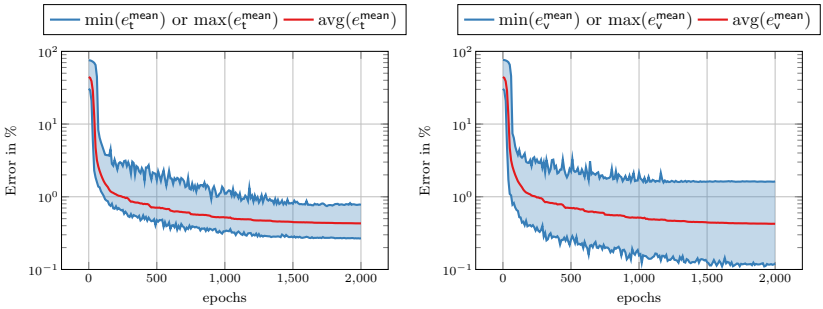

(a) Training set $\mathcal{S}^{\mathsf{t}}$ **(b)** Validation set $\mathcal{S}^{\mathsf{v}}$

Figure 5.6: Minimum, maximum, and average mean error e^{mean} of all trained FDMNs for the training set $\mathcal{S}^{\mathsf{t}}$ (a) and the validation set $\mathcal{S}^{\mathsf{v}}$ (b). Figure adapted from Sterr et al. (2024a, Figure 6).

To measure the quality of fit, we define the mean error e^{mean} over a subset $\mathcal{S}$ of the training data $\mathcal{S}^{\mathsf{D}}$ as

$$e^{\mathsf{mean}} = \frac{1}{|\mathcal{S}|} \sum_{\left(\mathbb{V}_1^s, \mathbb{V}_F, \bar{\mathbb{V}}^s\right) \in \mathcal{S}} \frac{\left\| \mathcal{DMN}_{\mathsf{L}}(\mathbb{V}_1^s, \mathbb{V}_F, \underline{\alpha}, \underline{w}) - \bar{\mathbb{V}}^s \right\|_1}{\left\| \bar{\mathbb{V}}^s \right\|_1}, \tag{5.94}$$

where $|\mathcal{S}|$ is the cardinality of the set $\mathcal{S}$. Depending on the fiber orientation state $\underline{\lambda}$ and the initial guesses of the angles $\underline{\alpha}$ and the weights $\underline{w}$, the quality of fit varies per DMN. Therefore, for the whole training process of all 620 FDMNs, we visualize the smallest mean error $\min(e^{\mathsf{mean}})$, the largest mean error $\max(e^{\mathsf{mean}})$, and the average mean error $\mathrm{avg}(e^{\mathsf{mean}})$ for the training and validation sets $\mathcal{S}^{\mathsf{t}}$ and $\mathcal{S}^{\mathsf{v}}$ per epoch in Figure 5.6. For the training and the validation set, we observe that the three considered error measures drop rapidly at the beginning of the training, and continue to improve as the training continues. As the learning rates are small for epochs larger than 1500, the errors do not change significantly at the end of the training, and convergence is ensured. Evidently, the largest mean error $\max(e_{\mathsf{t}}^{\mathsf{mean}})$ on the training set $\mathcal{S}^{\mathsf{t}}$ drops below 1% at the end of the

training process, while the smallest mean error $\min(e_{\mathsf{t}}^{\mathsf{mean}})$ falls below 0.3%. This indicates a high quality of fit on the training set $\mathcal{S}^{\mathsf{t}}$ for all FDMNs. Compared to the training set $\mathcal{S}^{\mathsf{t}}$, the spread between the largest mean error $\max(e_{\mathsf{v}}^{\mathsf{mean}})$ and the smallest mean error $\min(e_{\mathsf{v}}^{\mathsf{mean}})$ for the validation set $\mathcal{S}^{\mathsf{v}}$ is larger. However, the largest mean error $\max(e_{\mathsf{v}}^{\mathsf{mean}})$ stays below 2% for all considered FDMNs and does not fluctuate by a large margin. Additionally, the average mean error $\mathrm{avg}(e_{\mathsf{v}}^{\mathsf{mean}})$ decreases continuously during training. Consequently, the prediction quality on both the training and validation set improve on average as the training progresses, although the largest mean validation error $\max(e_{\mathsf{v}}^{\mathsf{mean}})$ does not improve significantly after 1250 training epochs. Overall, this indicates that no pronounced overfitting to the training data set $\mathcal{S}^{\mathsf{t}}$ occurs.

5.4.3 Online evaluation

To measure the online performance of an FDMN, we define the online error function $e_{\mathsf{on}} : \mathsf{Sym}_0(3) \to \mathbb{R}$ as

$$e_{\mathsf{on}}(\bar{\boldsymbol{D}}) = \frac{\|\boldsymbol{\sigma}^{DMN}(\bar{\boldsymbol{D}}) - \boldsymbol{\sigma}^{FFT}(\bar{\boldsymbol{D}})\|_2}{\|\boldsymbol{\sigma}^{FFT}(\bar{\boldsymbol{D}})\|_2}, \tag{5.95}$$

where $\|\cdot\|_2$ denotes the ℓ^2-norm of the components in Mandel notation, $\bar{\boldsymbol{D}}$ stands for the prescribed effective strain rate tensor, and $\boldsymbol{\sigma}^{DMN} : \mathsf{Sym}_0(3) \to \mathsf{Sym}_0(3)$ and $\boldsymbol{\sigma}^{FFT} : \mathsf{Sym}_0(3) \to \mathsf{Sym}_0(3)$ are the stress functions of the FDMN and the FFT-based homogenization, respectively. We then choose the largest error over all load cases $e_{\mathsf{on}}^{\mathsf{max}}$ and the mean error over all load cases $e_{\mathsf{on}}^{\mathsf{mean}}$

$$e_{\mathsf{on}}^{\mathsf{max}} = \max_{\bar{\boldsymbol{D}} \in \bar{\boldsymbol{D}}_{\dot{\gamma}}} e_{\mathsf{on}}, \quad e_{\mathsf{on}}^{\mathsf{mean}} = \frac{1}{|\bar{\boldsymbol{D}}_{\dot{\gamma}}|} \sum_{\bar{\boldsymbol{D}} \in \bar{\boldsymbol{D}}_{\dot{\gamma}}} e_{\mathsf{on}}(\bar{\boldsymbol{D}}), \tag{5.96}$$

to study the performance of the different FDMNs. For each investigated orientation state $\underline{\lambda}$, we identify the FDMN with the smallest maximum

error $e_{\text{on}}^{\text{max}}$ and visualize the associated errors $e_{\text{on}}^{\text{mean}}$ and $e_{\text{on}}^{\text{max}}$ over the fiber orientation triangle, see Figures 5.7a and 5.7b

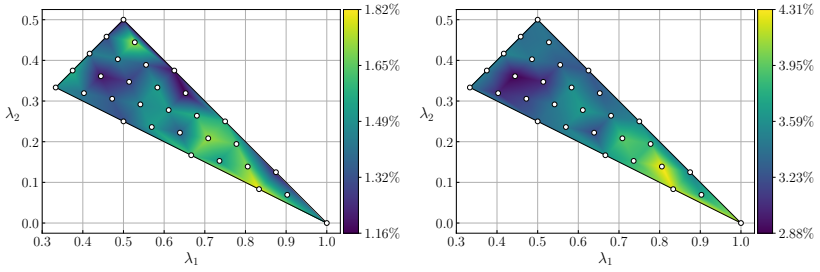

(a) Mean error $e_{\text{on}}^{\text{mean}}$ **(b)** Largest error $e_{\text{on}}^{\text{max}}$

Figure 5.7: Mean online error $e_{\text{on}}^{\text{mean}}$ (a) and largest online error $e_{\text{on}}^{\text{max}}$ (b) for the best FDMNs over the fiber orientation triangle. Figure adapted from Sterr et al. (2024a, Figure 7).

The maximum error $e_{\text{on}}^{\text{max}}$ of the best FDMNs range between 2.88% for the orientation state $\underline{\lambda} = (0.4444, 0.3611)^{\mathsf{T}}$, and 4.31% for the fiber orientation state $\underline{\lambda} = (0.8055, 0.1389)^{\mathsf{T}}$. Thus, for the investigated orientation states, the FDMNs yield sufficient prediction accuracy in terms of engineering requirements over a wide range of shear rates $\dot{\gamma} \in [10, 10^5]\,\mathrm{s}^{-1}$. Additionally, the relatively low maximum errors $e_{\text{on}}^{\text{max}}$ show that with fewer samples than in previous studies for solid materials, for example by Liu et al. (2019b) and Liu and Wu (2019) or Gajek et al. (2020; 2021; 2022), appropriately accurate FDMNs can be produced for suspensions of rigid fibers. Generally, the maximum error $e_{\text{on}}^{\text{max}}$ is larger for more strongly aligned oriented orientation states towards the lower right-hand side of the fiber orientation triangle than for less strongly aligned oriented orientation states towards the upper and the left-hand side. The mean error $e_{\text{on}}^{\text{mean}}$ ranges between 1.16% for the orientation state $\underline{\lambda} = (0.8334, 0.0833)^{\mathsf{T}}$, and 1.82% for the orientation

state $\underline{\lambda} = (0.6528, 0.3194)^{\mathsf{T}}$, underlining the prediction accuracy of the FDMNs.

To discuss one specific example, we take a more detailed look at the performance of the best FDMN at the fiber orientation state $\underline{\lambda} = (0.8055, 0.1389)^{\mathsf{T}}$ where the largest maximum error $e_{\mathsf{on}}^{\mathsf{max}} = 4.31\%$ occurs. Let the components of the strain rate tensor $\tilde{\boldsymbol{D}}_i \in \mathsf{Sym}_0(3)$, in the standard basis $\{\boldsymbol{e}_i\}$ and in Mandel notation, be given by the i-th column of the matrix $\bar{\underline{\underline{D}}}/\dot{\gamma}$, see equation (3.35). Then, the tensor $\tilde{\boldsymbol{D}}_i$ represents a load with unit norm, and we refer to the tensor $\tilde{\boldsymbol{D}}_i$ as load case. In the following, we discuss the observed stress responses and the prediction quality of the FDMN for all considered shear rates (3.44) and the six load cases defined in equation (3.35), see Figure 5.8. Because of the strong alignment of the fibers in the coordinate direction $\boldsymbol{e}_1$, the stress norms are the largest for the load case $\tilde{\boldsymbol{D}}_1$, which encodes incompressible elongational flow in the coordinate direction $\boldsymbol{e}_1$, see Figure 5.8a.

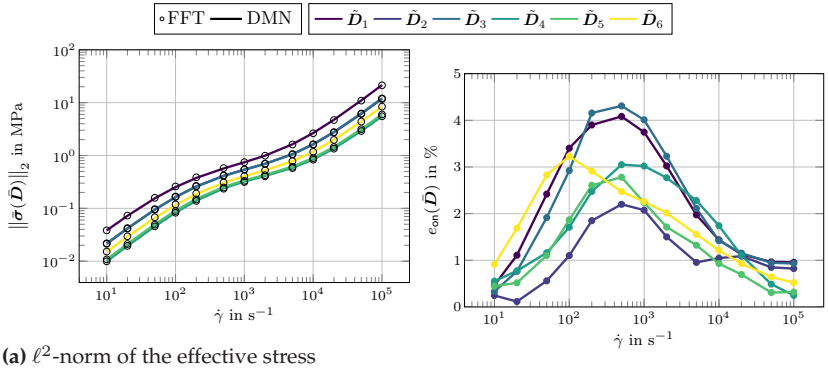

(a) ℓ^2-norm of the effective stress response $\bar{\boldsymbol{\sigma}}(\bar{\boldsymbol{D}})$

(b) Online error $e_{\mathsf{on}}(\bar{\boldsymbol{D}})$

Figure 5.8: ℓ^2-norm of the effective stress response $\bar{\boldsymbol{\sigma}}(\bar{\boldsymbol{D}})$ over the shear rate $\dot{\gamma} \in [10, 10^5]\,\mathrm{s}^{-1}$ at the orientation state $\underline{\lambda} = (0.8055, 0.1389)$ as computed with FFT-based homogenization and the best identified FDMN (a). Online error $e_{\mathsf{on}}(\bar{\boldsymbol{D}})$ of the FDMN over the shear rate $\dot{\gamma} \in [10, 10^5]\,\mathrm{s}^{-1}$ (b). Figure adapted from Sterr et al. (2024a, Figure 8).

The norms of the stress responses to elongational flow in the coordinate directions $\boldsymbol{e}_2$ and $\boldsymbol{e}_3$, i.e., the load cases $\tilde{\boldsymbol{D}}_2$ and $\tilde{\boldsymbol{D}}_3$, are comparatively small. For the largest considered shear rate of $\dot{\gamma} = 10^5\,\mathrm{s}^{-1}$, we observe a stress norm of 21 MPa for the load case $\tilde{\boldsymbol{D}}_1$, as well as 11.8 MPa and 12.1 MPa for the load cases $\tilde{\boldsymbol{D}}_2$ and $\tilde{\boldsymbol{D}}_3$, respectively. Because of the similar degrees of fiber alignment in the coordinate directions $\boldsymbol{e}_2$ and $\boldsymbol{e}_3$, the stress norms associated with the load cases $\tilde{\boldsymbol{D}}_2$ and $\tilde{\boldsymbol{D}}_3$ differ only slightly. Furthermore, the stress norms in response to shear in the load cases $\tilde{\boldsymbol{D}}_4$ and $\tilde{\boldsymbol{D}}_5$ are smaller than to shear in the load cases $\tilde{\boldsymbol{D}}_6$. Again, this is caused by the strong alignment of the fibers in the coordinate direction $\boldsymbol{e}_1$, which increases the flow resistance stronger in the $\boldsymbol{e}_1$-$\boldsymbol{e}_2$-plane than in other shear planes (Sterr et al., 2024b). For the largest considered shear rate of $\dot{\gamma} = 10^5\,\mathrm{s}^{-1}$, the stress norms are 5.5 MPa, 6.0 MPa, and 8.4 MPa for the load cases $\tilde{\boldsymbol{D}}_4$, $\tilde{\boldsymbol{D}}_5$, and $\tilde{\boldsymbol{D}}_6$, respectively. Overall, the predicted ℓ^2-norm of the effective stress response $\bar{\boldsymbol{\sigma}}^{DMN}$ of the FDMN agrees closely with the effective stress $\bar{\boldsymbol{\sigma}}^{FFT}$ computed via FFT-based homogenization for all investigated load directions $\tilde{\boldsymbol{D}}_i$, $i \in \{1, ..., 6\}$, and shear rates $\dot{\gamma} \in S_{\dot{\gamma}}$, see Figure 5.8a.

Not only the ℓ^2-norm of the effective stress response is predicted well by the FDMN, but the direction as well. This is evident from the relatively small online errors $e_{\mathsf{on}}(\bar{\boldsymbol{D}})$ shown in 5.8b. Depending on the load case, the error e_{on} increases up to a point in the interval $[10^2, 10^3]\,\mathrm{s}^{-1}$, before decreasing again for higher shear rates. The largest error occurs for the elongational load case $\tilde{\boldsymbol{D}}_3$ with 4.31%, and is closely followed by 4.08% for the elongational load case $\tilde{\boldsymbol{D}}_1$. For the shear load cases $\tilde{\boldsymbol{D}}_4$, $\tilde{\boldsymbol{D}}_5$, and $\tilde{\boldsymbol{D}}_6$, the largest errors are 3.05%, 2.78%, and 3.23%, respectively, while the largest error for the elongational load case $\tilde{\boldsymbol{D}}_2$ is 2.2%. The largest error for the shear load case $\tilde{\boldsymbol{D}}_6$ occurs at a shear rate of $\dot{\gamma} = 10^2\,\mathrm{s}^{-1}$, whereas the largest errors for all other load cases occur at a shear rate of $\dot{\gamma} = 5 \cdot 10^2\,\mathrm{s}^{-1}$. This is directly tied to the Cross-type constitutive equation (3.2), which has two Newtonian plateaus for low and high

shear rates and a non-linear transition in between. Consequently, for large shear rates $\dot{\gamma} \to \infty$ the Matrix behavior is Newtonian and the homogenization function of the microstructure approaches the linear homogenization function. Since the FDMN approximates the non-linear homogenization function the microstructure to first order (Gajek et al., 2020), the prediction quality depends on the degree to which the matrix behaves non-linearly. This is in line with previous observations regarding the modelling of shear-thinning fiber suspensions (Sterr et al., 2023; 2024b).

5.4.4 Computational Speedup

	Sampling Total	Sampling Per orientation (mean)	Training
CPU Hours	24415	788	0.08
Wall-clock time (h)	305	9.8	0.08

Table 5.1: CPU hours and wall-clock time for the training of one FDMN and the sampling of effective viscosities $\bar{\mathbb{V}}^s$ using FFT-based homogenization. Table adapted from Sterr et al. (2024a, Table 2).

	FFT (h)	DMN (ms)	Speedup
Min	2.08	600	11785
Mean	2.61	630	14828
Max	3.07	650	17225

Table 5.2: Speedups and wall-clock times for the evaluation of a single load case using FFT-based homogenization compared to an FDMN. Table adapted from Sterr et al. (2024a, Table 3).

For sampling the linear homogenization functions of the 31 considered fiber orientation states $\underline{\lambda} \in S_{\mathsf{T}}$, we used a workstation with two AMD EPYC 7552 48-Core processors and 1024 GB DRAM. We relied on a single thread per FFT-based computation and ran 80 computations in parallel. In total, the computations took 24415 CPU hours and a wall-clock time of 305 hours, see Table 5.1. Averaging over all 31 considered orientations $\underline{\lambda}$, this leads to 788 CPU Hours and $9.8\mathrm{h}$ wall-clock time per orientation. For the training and the online evaluation of the FDMNs, as well as the non-linear FFT-based computations, we used a workstation with two AMD EPYC 9534 64-Core Processors and 1024 GB DRAM, and ran all computations on a single thread. The wall-clock time to evaluate all six load cases $\tilde{\boldsymbol{D}}_i$, $i = 1, ..., 6$, and thirteen shear rates $\dot{\gamma} \in S_{\dot{\gamma}}$ in series for a single fiber orientation state $\underline{\lambda}$ is listed in Table 5.2. The wall-clock times for the FFT-based computations range from $2.08\mathrm{h}$ to $3.07\mathrm{h}$ with the mean wall-clock time over all considered orientation states $\underline{\lambda}$ being $2.61\mathrm{h}$. In contrast, the online evaluation of the FDMNs takes between $600\mathrm{ms}$ and $630\mathrm{ms}$, with a mean of $650\mathrm{ms}$. Consequently, the speedup factors range between 11785 and 17225 with a mean of 14828. This considerable speedup is achieved by investing computational resources into the sampling of the linear homogenization functions of the microstructures. It is straightforward to judge whether this investment is sensible for the considered setup. For one microstructure the generation of training data and the training of a single FDMN takes $9.88\mathrm{h}$ wall-clock time on average, while the non-linear FFT-based computations take $2.61\mathrm{h}$ wall-clock time on average. Therefore, assuming the non-linear computations run on one thread as in the presented setup, it would take four non-linear computation to offset the initial investment into an FDMN on average. Given that component scale simulations routinely require thousands or millions of microscale computations (Gajek et al., 2021; 2022), the sampling and training effort is offset easily in engineering problems.

5.4.5 Comparison with machine learning aided analytical models

In this section, we compare the FDMN based approach to predicting the effective behavior of fiber suspensions with another machine learning approach suggested by Sterr et al. (2024b). The authors presented four different analytical constitutive equations for the effective viscosity of shear-thinning fiber suspensions, and identified the model parameters using supervised machine learning. The model parameters were learned from simulation data obtained with FFT-based computational techniques for the same material as considered in this chapter: rigid fibers suspended in a Cross-type matrix material with parameters as shown in Table 4.1. However, the FDMN approach and the analytical approach follow very different paradigms. The FDMNs are trained to approximate the non-linear homogenization function of the microstructure by learning the respective *linear* homogenization function without prior knowledge of the actual constitutive equations. In contrast, the parameters of the analytical models were learned from the *non-linear* stress response of the suspension, and the analytical models incorporate knowledge about the expected material behavior. Even though the two approaches follow different strategies, they achieve comparable prediction accuracy. For the load cases $\bar{\boldsymbol{D}}_{\dot{\gamma}}$ and fiber orientation states $\underline{\lambda}$ considered in this chapter, the largest validation error of the FDMNs is 4.31% and occurs for the fiber orientation state $\underline{\lambda} = (0.8055, 0.1389)^{\mathsf{T}}$. For the same load cases $\bar{\boldsymbol{D}}_{\dot{\gamma}}$ and the same set of fiber orientation states $\underline{\lambda}$, three of the four analytical models by Sterr et al. (2024b) achieve a maximum prediction error of 5.00%, which occurs for the fiber orientation state $\underline{\lambda} = (0.8334, 0.0833)^{\mathsf{T}}$. The fourth model did not compare favorably with the other three, because the built-in assumptions of stress-strain rate superposition and orientation averaging did not hold well for the considered suspension (Sterr et al., 2024b). Consequently, the FDMNs achieved a slightly higher prediction accuracy for the type of fiber

suspension considered in this thesis. Also, within the constraints of a first order approximation, FDMNs generalize to different constitutive equations while the presented analytical models do not, reducing the required modelling effort for FDMNs. However, the FDMNs utilized in this thesis use 1150 free parameters, whereas the analytical models use between 11 and 49 parameters.

In terms of computational cost, generating the training data and training an FDMN for a single microstructure took $9.88\mathrm{h}$ wall-clock time on average, see Table 5.1. The parameters of the analytical models for a single microstructure were identified based on six non-linear FFT-based simulations, which took $2.61\mathrm{h}$ wall-clock time on average. This leads to an average total wall-clock time of $15.70\mathrm{h}$ if all required simulations are run in series on one thread, and $0.04\,\mathrm{h}$ are allocated to identify the model parameters. However, with the considered setup, the non-linear FFT-based simulations could be run in parallel, such that the analytical model parameters can be obtained more quickly than an FDMN. In summary, FDMNs offer a higher degree of accuracy and flexibility regarding the considered constitutive equations, but require more computational resources and a larger amount of parameters. Furthermore, FDMNs are inherently thermodynamically consistent (Gajek et al., 2020, §3.1), and inherit stress-strain rate monotonicity from their phases (Gajek et al., 2020, App. C). In contrast, both thermodynamic consistency and stress-strain rate monotonicity must be ensured manually in constitutive models.

5.5 Conclusions

In this chapter, we extended the direct DMN architecture to the Flexible DMN (FDMN) architecture for the treatment of fiber suspensions with infinite material contrast and shear-thinning matrix behavior. To do so, we derived linear homogenization functions for two-phase layered

emulsions that are governed by Stokes flow and consist of linearly viscous phases. More specifically, we utilized results by Kabel et al. (2016b) and Milton (2002) on the homogenization of laminates to derive closed form analytical expressions for the effective properties of such layered emulsions. Because rank-one layered materials are ill-suited as DMN building blocks in case of infinite material contrast, we investigated the effective properties of coated layered materials (CLMs). We leveraged the linear homogenization functions of rank-one layered materials and investigated under which conditions the effective behavior of CLMs is non-singular if the core material is rigid. The conditions depend on the physical constraints of the employed materials, and involve the rank of the CLM and the relative orientation of the layering directions. In the relevant case for incompressible fiber suspensions, a CLM consists of an incompressible coating material and a rigid core material. Then, the effective viscosity of a rank-3 CLM is non-singular if the three layering directions are mutually non-orthogonal and mutually non-collinear.

Using the derived homogenization functions for layered materials and CLMs, we extended the (direct) DMN architecture to the FDMN architecture by replacing the lowest layer of rank-one laminates in a (direct) DMN with non-singular CLMs, and the other rank-one laminates with rank-one layered materials capable of treating fluids. For the offline training of an FDMN, we presented a strategy where the relative angles of the CLM layering directions are fixed to reduce the amount of free parameters and guarantee non-singular CLMs. Furthermore, we modified the online evaluation strategy of direct DMNs to account for incompressible phases. We leveraged the FDMN architecture to predict the non-linear effective behavior of fiber suspensions with a Cross-type matrix material. Compared to direct numerical simulations with FFT-based computational techniques, the FDMNs achieved validation errors below 4.31% for a variety of 31 fiber orientation states, six different load cases, and a wide range of shear rates relevant to engineering processes.

If the time required to generate the training data and train the FDMNs is not considered, the FDMNs achieved an average speed up factor of 14828 as compared to FFT-based simulations. Additionally, FDMNs achieve higher accuracy than another machine learning based approach by Sterr et al. (2024b) for the same composite material. However, this competitive accuracy improvement comes at the cost of an increased computational effort to obtain the training data for the FDMNs.

Chapter 6

Summary, conclusions, and outlook

In this thesis, we combined high fidelity computational techniques with machine learning to investigate and model the viscous behavior of non-Newtonian fiber suspensions. Firstly, we developed an FFT-based approach for the computational homogenization of suspensions of rigid fibers in non-Newtonian media. We employed the developed FFT-based approach to investigate the anisotropic shear-thinning behavior of a transversely isotropic fiber suspension with a polyamide 6 (PA6) matrix material for a broad range of engineering flow scenarios. Secondly, we extended the scope of investigation into the anisotropic shear-thinning behavior of fiber suspensions to a total of 109 fiber orientation states, and thus generated a rich data set for use with machine learning techniques. We encoded the viscous fiber suspension behavior in four analytical models, and learned the model parameters from the generated data set using a supervised machine learning strategy. Finally, we developed a thermodynamically consistent Deep Material Network (DMN) architecture for the treatment of suspensions of rigid fibers in non-Newtonian media. To do so, we derived linear homogenization functions for rank-one two-phase layered emulsions with finite material contrast. To account for infinite material contrast, we derived closed form expressions for the effective viscosity of coated layered materials with incompressible phases. Before we give an outlook on possible

future research, we summarize the key aspects and findings of each chapter in the following.

Chapter 3:

- Because we consider rigid suspended fibers, the variational problem (3.18) is, constitutively, not well-defined. We showed that this issue can be addressed by leveraging the Legendre–Fenchel transform and changing to the dual formulation (3.24). Using a staggered grid to treat incompressible fluids, as well as composite voxels with a dual mixing rule, we demonstrated that the dual problem (3.24) may be solved efficiently using FFT-based techniques and a Newton-CG approach. This allows the study of rigid fibers suspended in a non-Newtonian matrix material, which was not possible previously.
- Using a limited number of computational experiments, the effective viscosity of fiber suspensions may be estimated and visualized by an interpolation based matrix equation and a direction dependent elongational viscosity.
- For a particular transversely isotropic orientation state and a shear-thinning PA6 matrix material, the degree of anisotropy of the effective suspension viscosity changes strongly depending on the shear rate and loading direction. This effect is more pronounced for higher fiber volume fractions.

Chapter 4:

- For a fixed fiber volume fraction, the anisotropy of the effective viscosity and its shear rate dependence vary strongly with the fiber orientation state. We found that stronger variations occur for more strongly oriented fiber orientation states, and observed the strongest variation for the unidirectional state.
- By leveraging the flexibility of automatic differentiation and gradient based learning, we established three models of varying complexity for the effective suspension viscosity. For 109 different fiber orientation

states, three models achieved errors below 5.15%. Another model based on the Mori-Tanaka formalism did not compare favorably.

- We demonstrated that the anisotropic shear-thinning behavior of the considered suspensions can be encoded to engineering accuracy using a generalized distance, which depends on an orientation state specific orthotropic tensor and the strain rate tensor.

Chapter 5:

- By leveraging results for linear elastic laminates, we derived closed form expressions for the effective viscosity of layered emulsions with linearly viscous phases. This paved the way for the development of DMNs for the treatment of fiber suspensions.
- For incompressible phases, we derived necessary and sufficient conditions for the rank and the layering directions of a coated layered material, such that its effective properties are non-singular, even if the core phase is rigid. In particular, the rank of the coated layered material must be greater than two, and the layering directions must be mutually non-orthogonal and mutually non-collinear.
- We presented the Flexible Deep Material Network (FDMN) architecture as an extension of the direct DMN Framework. In an FDMN, the lowest homogenization layer consists of coated layered materials instead of rank-one layered materials as in a typical direct DMN. This allows the practical treatment of infinite material contrast, which was highly difficult previously. Similar to a direct DMN, the remaining layers of an FDMN consist of rank-one layered materials.
- For 31 fiber orientation states, we demonstrated that FDMNs achieve a competitive prediction accuracy for the viscous behavior of rigid fibers suspended in a shear-thinning PA6 matrix. We observed a maximum error of 4.31%, which lies below the prediction error of the models presented in chapter 4.
- Compared to the models presented in chapter 4, FDMNs were trained on *linear* homogenization data, and do not incorporate knowledge

of the expected material behavior of the suspensions. Additionally, the FDMNs in this thesis were trained on smaller data sets than in previous DMN based studies. These considerations underline the remarkable prediction capabilities of FDMNs for non-linear material behavior.

With our work, we contributed to the numerical study and modeling of fiber suspensions with non-Newtonian matrix materials. Our main contributions are the development of an FFT-based computational homogenization approach, the identification of closed form effective viscosity models, and the development of the FDMN architecture. Overall, the applicability and the scale of our modeling approaches are mainly restricted by the computational cost to generate training data using FFT-based methods. This underscores the necessity for further research into efficient FFT-based techniques as well as other efficient computational methods. In particular, reduced computational requirements would allow the consideration of larger systems with higher fiber aspect ratios, or the consideration of additional complex physics. Using the computationally generated data, the closed form models and the FDMN architecture presented in this thesis enable efficient two-scale molding simulations. This could be leveraged for a variety of engineering processes simulations in composite manufacturing, such as injection and compression molding. Because fibers may break during processing, it would be of great interest to combine the closed form models and the FDMN architecture with synthetic microstructures (Mehta and Schneider, 2022) and molding simulations (Phelps et al., 2013) that incorporate fiber length distributions.

Furthermore, the developed FDMN framework could be applied and extended to problems involving more than two phases and more than one singular phase. This includes material systems such as fiber suspensions containing gaseous phases (Shuler et al., 1994; Cui and Grace, 2007), materials containing voids (Mehdikhani et al., 2019; Sika et al., 2020), or

solids containing liquid inclusions (Style et al., 2015; Wang and Henann, 2016). Especially in combination with fiber orientation interpolation techniques (Gajek et al., 2021; Huang et al., 2022; Dey et al., 2024) the presented FDMNs could enable novel types of multiscale simulations.

Appendix A

Coated layered materials with singular core

A.1 Singularity condition for coated layered materials with singular core

In the particular cases that the core material m_1 of a CLM is rigid or represents a void, the dual or the primal material properties $\mathbb{K}_1$ or $\mathbb{M}_1$ approach zero, respectively. Thus, more generally, we let the material tensor $\mathbb{A}_1$ approach zero, and rewrite equation (5.44) as

$$\lim_{\mathbb{A}_1 \to \mathbf{0}} \bar{\mathbb{A}} = \mathbb{A}_2 \left(\mathbb{I} + (1 - f_2) \left(-\mathbb{I} + f_2 \sum_{r=1}^{R} c_r \mathbb{\Gamma}_{\mathbb{A}_2}(\boldsymbol{n}_r) \mathbb{A}_2 \right)^{-1} \right). \quad \text{(A.1)}$$

In the following, we study under which conditions the effective material properties $\bar{\mathbb{A}}$ of a rank-R CLM are singular. The effective material properties $\bar{\mathbb{A}}$ are singular precisely if there exists an effective tensor $\bar{\boldsymbol{g}} \in \{\mathsf{Sym}(3), \mathsf{Sym}_0(3)\}$, such that

$$\bar{\mathbb{A}}[\bar{\boldsymbol{g}}] = \mathbf{0}. \quad \text{(A.2)}$$

Using the definition (A.1), equation (A.2) may be equivalently rewritten in the form

$$\left(\sum_{r=1}^{R} c_r \mathbb{\Gamma}_{\mathbb{A}_2}(\boldsymbol{n}_r)\mathbb{A}_2\right)[\bar{\boldsymbol{g}}] = \bar{\boldsymbol{g}}. \tag{A.3}$$

Equation (A.3) is satisfied precisely if $\bar{\boldsymbol{g}}$ lies in the intersection of all subspaces $\mathcal{E}_r^{\mathsf{A}}$, such that

$$\bar{\boldsymbol{g}} \in \bigcap_{r=1}^{R} \mathcal{E}_r^{\mathsf{A}}, \tag{A.4}$$

or, equivalently,

$$\mathbb{\Gamma}_{\mathbb{I}}(\boldsymbol{n}_r)[\bar{\boldsymbol{g}}] = \bar{\boldsymbol{g}}, \quad \forall r \in \{1, ..., R\}. \tag{A.5}$$

We prove this as follows. First, if $\bar{\boldsymbol{g}}$ lies in the section of all subspaces such that (A.4) is satisfied, it follows from equation (A.5) and the definition of the operator $\mathbb{\Gamma}_{\mathbb{A}_2}(\boldsymbol{n}_r)$ (5.43) that

$$\begin{aligned}\left(\sum_{r=1}^{R} c_r \mathbb{\Gamma}_{\mathbb{A}_2}(\boldsymbol{n}_r)\mathbb{A}_2\right)[\bar{\boldsymbol{g}}] &= \left(\sum_{r=1}^{R} c_r \mathbb{\Gamma}_{\mathbb{A}_2}(\boldsymbol{n}_r)\mathbb{A}_2\mathbb{\Gamma}_{\mathbb{I}}(\boldsymbol{n}_r)[\bar{\boldsymbol{g}}]\right) \\ &= \sum_{r=1}^{R} c_r \bar{\boldsymbol{g}} = \bar{\boldsymbol{g}},\end{aligned} \tag{A.6}$$

and hence equation (A.3) is satisfied. Second we wish to prove that the converse is also true, i.e., if equation (A.3) is satisfied, equation (A.4) is satisfied as well. Let $\mathbb{T}_{\mathbb{A}_2}$ denote a convex combination of the projectors $\mathbb{\Gamma}_{\mathbb{A}_2}(\boldsymbol{n}_r)\mathbb{A}_2$, i.e.,

$$\mathbb{T}_{\mathbb{A}_2} = \left(\sum_{r=1}^{R} c_r \mathbb{\Gamma}_{\mathbb{A}_2}(\boldsymbol{n}_r)\mathbb{A}_2\right), \tag{A.7}$$

with

$$c_r > 0 \quad \text{and} \quad \sum_{r=1}^{R} c_r = 1. \tag{A.8}$$

Then, fixed points of the operator $\mathbb{T}_{\mathbb{A}_2}$ lie in the set (Reich, 1983, Lemma 1.4)

$$\mathcal{E} = \bigcap_{r=1}^{R} \mathcal{E}_r^{\mathsf{A}}. \tag{A.9}$$

Therefore, any eigenvector of the operator $\mathbb{T}_{\mathbb{A}_2}$ corresponding to the eigenvalue one must lie in the intersection of the subspaces $\mathcal{E}_r^{\mathsf{A}}$, which we denote with $\mathcal{E}$. In particular, if equation (A.3) is satisfied, the element $\bar{\boldsymbol{g}}$ lies in $\mathcal{E}$, i.e.,

$$\mathbb{T}_{\mathbb{A}_2}[\bar{\boldsymbol{g}}] = \bar{\boldsymbol{g}}, \quad \Longrightarrow \quad \bar{\boldsymbol{g}} \in \mathcal{E} \tag{A.10}$$

and equation (A.4) is satisfied as well.

With the result (A.10) at hand, we observe that a necessary and sufficient condition for the regularity of a rank-R CLM is that the space $\mathcal{E}$ is trivial, i.e.,

$$\mathcal{E} = \{\mathbf{0}\}. \tag{A.11}$$

We refer to equation (A.11) as *non-singularity condition* in the following. In the context of linear elastic and linearly viscous materials, we derived the non-singularity condition (A.11) for the spaces $\mathcal{E}_r^{\mathsf{A}}$, such that

$$\mathcal{E}_r^{\mathsf{A}} \subset \mathsf{Sym}(3), \quad \forall r \in \{1, ..., R\} \quad \text{or} \quad \mathcal{E}_r^{\mathsf{A}} \subset \mathsf{Sym}_0(3), \quad \forall r \in \{1, ..., R\}. \tag{A.12}$$

However, the presented proof extends to other problems that can be formulated in the form of equation (A.1), such as thermoelastic or piecoelectricity problems (Milton, 2002, Â§9). With the goal of using CLMs as building blocks in a DMN architecture, we are interested in whether there are particular choices of the layering directions $\boldsymbol{n}_r$ and the rank R of the CLM for which the effective properties of a CLM are always non-singular, i.e., the non-singularity condition (A.11) is satisfied. For incompressible suspensions of rigid fibers, we study this question for CLMs with a rigid core material m_1 and an incompressible coating material m_2.

A.2 Coated layered materials with incompressible coating and rigid core

For applications involving rigid inclusions in incompressible media, we consider CLMs with an incompressible coating material m_2 and a rigid core material m_1. Therefore, the spaces $\mathcal{E}_r^{\mathsf{A}} \subset \mathsf{Sym}_0(3)$ have the form

$$\begin{aligned}\mathcal{E}_r^{\mathsf{A}} = \{\boldsymbol{B} \in \mathsf{Sym}_0(3) \quad | \quad & \boldsymbol{B} \cdot (\boldsymbol{n}_r \otimes_{\mathsf{s}} \boldsymbol{a}) = 0, \\ & \forall \boldsymbol{a} \in \mathbb{R}^3 \quad \text{with} \quad \boldsymbol{a} \cdot \boldsymbol{n}_r = 0\},\end{aligned} \tag{A.13}$$

with the dimensions of the spaces $\mathcal{E}_r^{\mathsf{A}}$ and $\mathsf{Sym}_0(3)$ given by

$$\dim(\mathcal{E}_r^{\mathsf{A}}) = 3, \quad \text{and} \quad \dim(\mathsf{Sym}_0(3)) = 5. \tag{A.14}$$

Because the dimension $\dim(\mathcal{E}_1^{\mathsf{A}} + \mathcal{E}_2^{\mathsf{A}})$ is bounded by the dimension of the space $\mathsf{Sym}_0(3)$, such that

$$\dim(\mathcal{E}_1^{\mathsf{A}} + \mathcal{E}_2^{\mathsf{A}}) \leq 5, \tag{A.15}$$

it follows from the dimension of the intersection of the two spaces $\mathcal{E}_1^{\mathsf{A}}$ and $\mathcal{E}_2^{\mathsf{A}}$

$$\dim(\mathcal{E}_1^{\mathsf{A}} \cap \mathcal{E}_2^{\mathsf{A}}) = \dim(\mathcal{E}_1^{\mathsf{A}}) + \dim(\mathcal{E}_2^{\mathsf{A}}) - \dim(\mathcal{E}_1^{\mathsf{A}} + \mathcal{E}_2^{\mathsf{A}}), \tag{A.16}$$

that

$$\dim(\mathcal{E}_1^{\mathsf{A}} \cap \mathcal{E}_2^{\mathsf{A}}) \geq 3 + 3 - 5 = 1. \tag{A.17}$$

In other words, the intersection of the spaces $\mathcal{E}_1^{\mathsf{A}}$ and $\mathcal{E}_2^{\mathsf{A}}$ is at least one dimensional. Consequently, two layering directions are not sufficient to satisfy the condition (A.11) Besides the required number of layerings, we are also interested in whether there are restrictions on the angles between the layering directions. Suppose that one layering direction is

orthogonal to the other two. We discuss the case that the direction $\boldsymbol{n}_3$ is orthogonal to the normals $\boldsymbol{n}_1$ and $\boldsymbol{n}_2$. The other cases work similarly via permuting the indices. Then it holds that

$$\boldsymbol{n}_3 \cdot \boldsymbol{n}_1 = 0, \quad \text{and} \quad \boldsymbol{n}_3 \cdot \boldsymbol{n}_2 = 0, \tag{A.18}$$

and the intersection $\mathcal{E}_1^{\mathsf{A}} \cap \mathcal{E}_2^{\mathsf{A}} \cap \mathcal{E}_3^{\mathsf{A}}$ does not only contain the zero element $\mathbf{0}$. Hence, the condition (A.11) is violated. To show this, we consider the alternative description of the spaces $\mathcal{E}_r^{\mathsf{A}}$

$$\mathcal{E}_r^{\mathsf{A}} = \{\boldsymbol{B} \in \mathsf{Sym}_0(3) \quad | \quad \boldsymbol{B}\boldsymbol{n}_r = \alpha \boldsymbol{n}_r \quad \text{for some} \quad \alpha \in \mathbb{R}\} \tag{A.19}$$

which is equivalent to equation (A.13) and characterizes the space $\mathcal{E}_r^{\mathsf{A}}$ via all tensors $\boldsymbol{B} \in \mathcal{E}_r^{\mathsf{A}}$ that have the layering direction $\boldsymbol{n}_r$ as an eigenvector. Then the tensor

$$\boldsymbol{B} = \boldsymbol{n}_1 \otimes \boldsymbol{n}_1 + \boldsymbol{m}_2 \otimes \boldsymbol{m}_2 - 2\boldsymbol{n}_3 \otimes \boldsymbol{n}_3, \tag{A.20}$$

where the layering direction $\boldsymbol{m}_2$ is constructed by orthogonalization, such that

$$\boldsymbol{m}_2 = \boldsymbol{n}_2 - (\boldsymbol{n}_1 \cdot \boldsymbol{n}_2)\boldsymbol{n}_1, \tag{A.21}$$

is an element of the intersection $\mathcal{E}_1^{\mathsf{A}} \cap \mathcal{E}_2^{\mathsf{A}} \cap \mathcal{E}_3^{\mathsf{A}}$. This is true because it holds that

$$\mathrm{tr}(\boldsymbol{B}) = 0, \quad \boldsymbol{B}\boldsymbol{n}_1 = \boldsymbol{n}_1, \quad \boldsymbol{B}\boldsymbol{n}_2 = \boldsymbol{n}_2, \quad \boldsymbol{B}\boldsymbol{n}_3 = \boldsymbol{n}_3, \tag{A.22}$$

and therefore condition (A.11) is violated. In other words, the effective properties $\bar{\mathbb{A}}$ of a rank-3 CLM with incompressible coating and rigid core, where one layering direction $\boldsymbol{n}_3$ is orthogonal to the other two layering directions $\boldsymbol{n}_1$ and $\boldsymbol{n}_2$, is always singular. Particularly, if all three layering directions are mutually orthogonal, the effective properties $\bar{\mathbb{A}}$ of a rank-3 CLM are singular.

In contrast, let the three layering directions be mutually non-orthogonal and mutually non-collinear, i.e.,

$$0 < |\boldsymbol{n}_1 \cdot \boldsymbol{n}_2| < 1, \quad 0 < |\boldsymbol{n}_1 \cdot \boldsymbol{n}_3| < 1, \quad 0 < |\boldsymbol{n}_2 \cdot \boldsymbol{n}_3| < 1. \tag{A.23}$$

We consider an element $\boldsymbol{B}$ in the intersection $\mathcal{E}_1^{\mathsf{A}} \cap \mathcal{E}_2^{\mathsf{A}} \cap \mathcal{E}_3^{\mathsf{A}}$ and wish to show that the tensor $\boldsymbol{B}$ vanishes, such that the non-singularity condition (A.11) is satisfied. Because the tensor $\boldsymbol{B}$ is symmetric, its eigenvectors corresponding to distinct eigenvalues are orthogonal. Thus, if the eigenvalues were distinct, the layering directions would need to be orthogonal. However, this contradicts our assumption (A.23). Therefore, the tensor $\boldsymbol{B}$ has a single eigenvalue α with the corresponding eigenspace $\mathbb{R}^3$, i.e., the tensor $\boldsymbol{B}$ attains the form

$$\boldsymbol{B} = \alpha \boldsymbol{I}, \quad \alpha \in \mathbb{R}. \tag{A.24}$$

Additionally, because the trace of the tensor $\boldsymbol{B}$ vanishes, i.e., $\operatorname{tr}(\boldsymbol{B}) = 0$, it follows that the eigenvalue α is zero. Consequently, the tensor $\boldsymbol{B}$ must vanish, the non-singularity condition (A.11) is satisfied, and the effective properties $\bar{\mathbb{A}}$ of a rank-3 CLM with an incompressible coating material m_2 and a rigid core material m_1 are non-singular, if the three layering directions are mutually non-orthogonal and non-collinear.

Bibliography

Advani, S. G., Tucker III, C. L., 1987. The use of tensors to describe and predict fiber orientation in short fiber composites. Journal of Rheology 31 (8), 751–784.

Armijo, L., 1966. Minimization of functions having Lipschitz continuous first partial derivatives. Pacific Journal of Mathematics 16 (1), 1–3.

Ashwin, N. R., Cao, Z., Muralidhar, N., Tafti, D., Karpatne, A., 2022. Deep learning methods for predicting fluid forces in dense particle suspensions. Powder Technology 401, 117303.

Ashwin, N. R., Tafti, D., Muralidhar, N., Cao, Z., 2024. Physics informed deep learning for flow and force predictions in dense ellipsoidal particle suspensions. Powder Technology 439, 119684.

Balboa Usabiaga, F., Kallemov, B., Delmotte, B., Bhalla, A., Griffith, B., Donev, A., 2017. Hydrodynamics of suspensions of passive and active rigid particles: a rigid multiblob approach. Communications in Applied Mathematics and Computational Science 11 (2), 217–296.

Barzilai, J., Borwein, J. M., 1988. Two-point step size gradient methods. IMA Journal of Numerical Analysis 8 (1), 141–148.

BASF, 2020. Ultramid®B3K Polyamide 6 material data. https://www.campusplastics.com/campus/de/datasheet/Ultramid%C2%AE+B3K/BASF/20/3a22f000, accessed: 2020-09-26.

Batchelor, G., 1970. The stress system in a suspension of force-free particles. Journal of Fluid Mechanics 41 (3), 545–570.

Batchelor, G., 1971. The stress generated in a non-dilute suspension of elongated particles by pure straining motion. Journal of Fluid Mechanics 46 (4), 813–829.

Bauer, J. K., Böhlke, T., 2022. Variety of fiber orientation tensors. Mathematics and Mechanics of Solids 27 (7), 1185–1211.

Bauer, J. K., Schneider, M., Böhlke, T., 2023. On the phase space of fourth-order fiber-orientation tensors. Journal of Elasticity 153 (2), 161–184.

Bertóti, R., 2021. Modeling the Flow-induced Anisotropic Effective Viscosity of Fiber Suspensions by Mean-field and Full-field Homogenization. Doctoral thesis, KIT Scientific Publishing, Karlsruhe, Germany.

Bertóti, R., Böhlke, T., 2017. Flow-induced anisotropic viscosity in short FRPs. Mechanics of Advanced Materials and Modern Processes 3 (1), 1–12.

Bertóti, R., Wicht, D., Hrymak, A., Schneider, M., Böhlke, T., 2021. A computational investigation of the effective viscosity of short-fiber reinforced thermoplastics by an FFT-based method. European Journal of Mechanics-B/Fluids 90, 99–113.

Bertram, A., 2012. Elasticity and Plasticity of Large Deformations. Springer, Berlin, Heidelberg, Germany.

Bhattacharya, K., Suquet, P., 2005. A model problem concerning recoverable strains of shape-memory polycrystals. Proceedings of the Royal Society A: Mathematical, Physical and Engineering Sciences 461 (2061), 2797–2816.

Binding, D., 1991. Capillary and contraction flow of long-(glass) fibre filled polypropylene. Composites Manufacturing 2 (3-4), 243–252.

Böhlke, T., 2004. The Voigt bound of the stress potential of isotropic viscoplastic FCC polycrystals. Archives of Mechanics 56 (6), 425–445.

Böhlke, T., Bertram, A., 2003. The Reuss bound of the strain rate potential of viscoplastic FCC polycrystals. Technische Mechanik-European Journal of Engineering Mechanics 23 (2-4), 184–194.

Böhlke, T., Brüggemann, C., 2001. Graphical representation of the generalized Hooke's law. Technische Mechanik 21 (2), 145–158.

Böhlke, T., Henning, F., Hrymak, A. N., Kärger, L., Weidenmann, K., Wood, J. T., 2019. Continuous–Discontinuous Fiber-Reinforced Polymers: An Integrated Engineering Approach. Carl Hanser Verlag GmbH Co KG, Munich, Germany.

Boodaghidizaji, M., Khan, M., Ardekani, A. M., 2022. Multi-fidelity modeling to predict the rheological properties of a suspension of fibers using neural networks and Gaussian processes. Physics of Fluids 34 (5).

Botín-Sanabria, D. M., Mihaita, A.-S., Peimbert-García, R. E., Ramírez-Moreno, M. A., Ramírez-Mendoza, R. A., Lozoya-Santos, J. d. J., 2022. Digital twin technology challenges and applications: A comprehensive review. Remote Sensing 14 (6), 1335.

Brunn, P., 1977. The slow motion of a rigid particle in a second-order fluid. Journal of Fluid Mechanics 82 (3), 529–547.

Brunn, P., 1980. The motion of rigid particles in viscoelastic fluids. Journal of Non-Newtonian Fluid Mechanics 7 (4), 271–288.

Castro, J., Tomlinson, G., 1990. Predicting molding forces in SMC compression molding. Polymer Engineering & Science 30 (24), 1568–1573.

Chambolle, A., Pock, T., 2016. An introduction to continuous optimization for imaging. Acta Numerica 25, 161–319.

Chen, X., Liu, S., Sun, R., Hong, M., 2018. On the convergence of a class of ADAM-type algorithms for non-convex optimization. arXiv:1808.02941 .

Coffin, D., Pipes, R. B., 1991. Constitutive relationships for aligned discontinuous fibre composites. Composites Manufacturing 2 (3-4), 141–146.

Cross, M. M., 1965. Rheology of non-Newtonian fluids: a new flow equation for pseudoplastic systems. Journal of Colloid Science 20 (5), 417–437.

Cross, M. M., 1970. Kinetic interpretation of non-Newtonian flow. Journal of Colloid and Interface Science 33 (1), 30–35.

Cui, H., Grace, J. R., 2007. Flow of pulp fibre suspension and slurries: A review. International Journal of Multiphase Flow 33 (9), 921–934.

Darken, C., Chang, J., Moody, J., et al., 1992. Learning rate schedules for faster stochastic gradient search. Neural Networks for Signal Processing 2, 3–12.

Darken, C., Moody, J., 1990. Note on learning rate schedules for stochastic optimization. Advances in Neural Information Processing Systems 3, 832–838.

Dembo, R. S., Eisenstat, S. C., Steihaug, T., 1982. Inexact Newton methods. SIAM Journal on Numerical Analysis 19 (2), 400–408.

Dey, A. P., Welschinger, F., Schneider, M., Gajek, S., Böhlke, T., 2022. Training deep material networks to reproduce creep loading of short fiber-reinforced thermoplastics with an inelastically-informed strategy. Archive of Applied Mechanics 92 (9), 2733–2755.

Dey, A. P., Welschinger, F., Schneider, M., Gajek, S., Böhlke, T., 2023. Rapid inverse calibration of a multiscale model for the viscoplastic and creep behavior of short fiber-reinforced thermoplastics based on deep material networks. International Journal of Plasticity 160, 103484.

Dey, A. P., Welschinger, F., Schneider, M., Köbler, J., Böhlke, T., 2024. On the effectiveness of deep material networks for the multi-scale virtual characterization of short fiber-reinforced thermoplastics under highly nonlinear load cases. Archive of Applied Mechanics 94, 1177–1202.

Dinh, S. M., Armstrong, R. C., 1984. A rheological equation of state for semiconcentrated fiber suspensions. Journal of Rheology 28 (3), 207–227.

Domurath, J., Ausias, G., Férec, J., Saphiannikova, M., 2020. Numerical investigation of dilute suspensions of rigid rods in power-law fluids. Journal of Non-Newtonian Fluid Mechanics 280, 104280.

Domurath, J., Saphiannikova, M., Férec, J., Ausias, G., Heinrich, G., 2015. Stress and strain amplification in a dilute suspension of spherical particles based on a Bird–Carreau model. Journal of Non-Newtonian Fluid Mechanics 221, 95–102.

Duchi, J., Hazan, E., Singer, Y., 2011. Adaptive subgradient methods for online learning and stochastic optimization. Journal of Machine Learning Research 12 (7), 2121–2159.

Edelen, D. G., 1973. On the existence of symmetry relations and dissipation potentials. Archive for Rational Mechanics and Analysis 51, 218–227.

Einstein, A., 1905. Eine neue Bestimmung der Moleküldimensionen. Doctoral thesis, ETH Zürich, Zürich, Switzerland.

Ericksen, J., 1959. Anisotropic fluids. Archive for Rational Mechanics and Analysis 4 (1), 231–237.

Ericksen, J., 1960. Transversely isotropic fluids. Kolloid-Zeitschrift 173 (2), 117–122.

Eschbach, A. R., Dec. 21 1993. Dynamic shear rheometer and method. US Patent 5,271,266.

Favaloro, A. J., Tseng, H.-C., Pipes, R. B., 2018. A new anisotropic viscous constitutive model for composites molding simulation. Composites Part A: Applied Science and Manufacturing 115, 112–122.

Férec, J., Bertevas, E., Khoo, B. C., Ausias, G., Phan-Thien, N., 2016. The effect of shear-thinning behaviour on rod orientation in filled fluids. Journal of Fluid Mechanics 798, 350–370.

Férec, J., Bertevas, E., Khoo, B. C., Ausias, G., Phan-Thien, N., 2017. A rheological constitutive model for semiconcentrated rod suspensions in Bingham fluids. Physics of Fluids 29 (7), 073103.

Feyel, F., 2003. A multilevel finite element method (FE2) to describe the response of highly non-linear structures using generalized continua. Computer Methods in Applied Mechanics and Engineering 192 (28-30), 3233–3244.

Fokker, A. D., 1914. Die mittlere Energie rotierender elektrischer Dipole im Strahlungsfeld. Annalen der Physik 348 (5), 810–820.

Friesenbichler, W., Duretek, I., Rajganesh, J., Kumar, S. R., 2011. Measuring the pressure dependent viscosity at high shear rates using a new rheological injection mould. Polimery 56 (1), 58–62.

Gajek, S., Schneider, M., Böhlke, T., 2020. On the micromechanics of deep material networks. Journal of the Mechanics and Physics of Solids 142, 103984.

Gajek, S., Schneider, M., Böhlke, T., 2021. An FE–DMN method for the multiscale analysis of short fiber reinforced plastic components. Computer Methods in Applied Mechanics and Engineering 384, 113952.

Gajek, S., Schneider, M., Böhlke, T., 2022. An FE-DMN method for the multiscale analysis of thermomechanical composites. Computational Mechanics 69 (5), 1087–1113.

Goddard, J., 1976a. The stress field of slender particles oriented by a non-Newtonian extensional flow. Journal of Fluid Mechanics 78 (1), 177–206.

Goddard, J., 1978. Tensile behavior of power-Law fluids containing oriented slender fibers. Journal of Rheology 22 (6), 615–622.

Goddard, J. D., 1976b. Tensile stress contribution of flow-oriented slender particles in non-Newtonian fluids. Journal of Non-Newtonian Fluid Mechanics 1, 1–17.

Goldstein, A. A., 1965. On steepest descent. Journal of the Society for Industrial and Applied Mathematics, Series A: Control 3 (1), 147–151.

Goodship, V., 2017. ARBURG Practical Guide to Injection Moulding. Smithers Rapra, Shawbury, United Kingdom.

Görthofer, J., Meyer, N., Pallicity, T. D., Schöttl, L., Trauth, A., Schemmann, M., Hohberg, M., Pinter, P., Elsner, P., Henning, F., et al., 2019. Virtual process chain of sheet molding compound: Development, validation and perspectives. Composites Part B: Engineering 169, 133–147.

Harlow, F. H., Welch, J. E., 1965. Numerical calculation of time-dependent viscous incompressible flow of fluid with free surface. The Physics of Fluids 8 (12), 2182–2189.

Haupt, P., 2002. Continuum mechanics and theory of materials. Springer, Berlin, Heidelberg, Germany.

He, Q.-C., Curnier, A., 1995. A more fundamental approach to damaged elastic stress-strain relations. International Journal of Solids and Structures 32 (10), 1433–1457.

Henning, F., Kärger, L., Dörr, D., Schirmaier, F. J., Seuffert, J., Bernath, A., 2019. Fast processing and continuous simulation of automotive structural composite components. Composites Science and Technology 171, 261–279.

Hill, R., 1963. Elastic properties of reinforced solids: some theoretical principles. Journal of the Mechanics and Physics of Solids 11 (5), 357–372.

Huang, T., Liu, Z., Wu, C., Chen, W., 2022. Microstructure-guided deep material network for rapid nonlinear material modeling and uncertainty quantification. Computer Methods in Applied Mechanics and Engineering 398, 115197.

Kabanikhin, S. I., 2008. Definitions and examples of inverse and ill-posed problems. Journal of Inverse and Ill-posed Problems 16, 317–357.

Kabel, M., Böhlke, T., Schneider, M., 2014. Efficient fixed point and Newton–Krylov solvers for FFT-based homogenization of elasticity at large deformations. Computational Mechanics 54 (6), 1497–1514.

Kabel, M., Fink, A., Schneider, M., 2017. The composite voxel technique for inelastic problems. Computer Methods in Applied Mechanics and Engineering 322, 396–418.

Kabel, M., Fliegener, S., Schneider, M., 2016a. Mixed boundary conditions for FFT-based homogenization at finite strains. Computational Mechanics 57 (2), 193–210.

Kabel, M., Ospald, F., Schneider, M., 2016b. A model order reduction method for computational homogenization at finite strains on regular grids using hyperelastic laminates to approximate interfaces. Computer Methods in Applied Mechanics and Engineering 309, 476–496.

Kaloni, P., Stastna, V., 1983. Steady-shear rheological behavior of the suspension of spherical particles in a second-order fluid. Polymer Engineering and Science 23 (8), 465–470.

Kanatani, K., 1984. Distribution of directional data and fabric tensors. International Journal of Engineering Science 22 (2), 149–164.

Kanit, T., Forest, S., Galliet, I., Mounoury, V., Jeulin, D., 2003. Determination of the size of the representative volume element for random composites: statistical and numerical approach. International Journal of Solids and Structures 40 (13-14), 3647–3679.

Karl, T., Böhlke, T., 2022. Unified mean-field modeling of viscous short-fiber suspensions and solid short-fiber reinforced composites. Archive of Applied Mechanics 92 (12), 3695–3727.

Karl, T., Gatti, D., Böhlke, T., Frohnapfel, B., 2021. Coupled simulation of flow-induced viscous and elastic anisotropy of short-fiber reinforced composites. Acta Mechanica 232 (6), 2249–2268.

Kennedy, P., Zheng, R., 2013. Flow Analysis of Injection Molds. Carl Hanser Verlag GmbH Co KG, Munich, Germany.

Khan, M., More, R. V., Ardekani, A. M., 2023. A constitutive model for sheared dense fiber suspensions. Physics of Fluids 35 (1), 013337.

Kingma, D. P., Ba, J., 2014. Adam: A method for stochastic optimization. arXiv:1412.6980 .

Köbler, J., Schneider, M., Ospald, F., Andrä, H., Müller, R., 2018. Fiber orientation interpolation for the multiscale analysis of short fiber reinforced composite parts. Computational Mechanics 61, 729–750.

Koch, D. L., 1995. A model for orientational diffusion in fiber suspensions. Physics of Fluids 7 (8), 2086–2088.

Kochmann, J., Wulfinghoff, S., Reese, S., Mianroodi, J. R., Svendsen, B., 2016. Two-scale FE–FFT-and phase-field-based computational modeling of bulk microstructural evolution and macroscopic material behavior. Computer Methods in Applied Mechanics and Engineering 305, 89–110.

Krawietz, A., 2013. Materialtheorie: Mathematische Beschreibung des phänomenologischen thermomechanischen Verhaltens. Springer, Berlin, Heidelberg, Germany.

Krishnan, J. M., Deshpande, A. P., Kumar, P. S., 2010. Rheology of Complex Fluids. Springer, Berlin, Heidelberg, Germany.

Kube, C. M., 2016. Elastic anisotropy of crystals. AIP advances 6 (9), 095209.

Landau, L. D., Lifshitz, E. M., 2013. Fluid Mechanics. Vol. 6. Elsevier, Amsterdam, Netherlands.

Leal, L., 1975. The slow motion of slender rod-like particles in a second-order fluid. Journal of Fluid Mechanics 69 (2), 305–337.

Li, T., 2024. Micromechanics-informed parametric deep material network for physics behavior prediction of heterogeneous materials with a varying morphology. Computer Methods in Applied Mechanics and Engineering 419, 116687.

Liu, D. C., Nocedal, J., 1989. On the limited memory BFGS method for large scale optimization. Mathematical Programming 45 (1), 503–528.

Liu, I.-S., 2002. Continuum Mechanics. Vol. 5. Springer, Berlin, Heidelberg, Germany.

Liu, L., Jiang, H., He, P., Chen, W., Liu, X., Gao, J., Han, J., 2019a. On the variance of the adaptive learning rate and beyond. arXiv:1908.03265 .

Liu, Z., 2020. Deep material network with cohesive layers: Multi-stage training and interfacial failure analysis. Computer Methods in Applied Mechanics and Engineering 363, 112913.

Liu, Z., 2021. Cell division in deep material networks applied to multiscale strain localization modeling. Computer Methods in Applied Mechanics and Engineering 384, 113914.

Liu, Z., Wu, C., 2019. Exploring the 3D architectures of deep material network in data-driven multiscale mechanics. Journal of the Mechanics and Physics of Solids 127, 20–46.

Liu, Z., Wu, C., Koishi, M., 2019b. A deep material network for multiscale topology learning and accelerated nonlinear modeling of heterogeneous materials. Computer Methods in Applied Mechanics and Engineering 345, 1138–1168.

Liu, Z., Wu, C., Koishi, M., 2019c. Transfer learning of deep material network for seamless structure–property predictions. Computational Mechanics 64 (2), 451–465.

Lucarini, S., Upadhyay, M. V., Segurado, J., 2021. FFT based approaches in micromechanics: fundamentals, methods and applications. Modelling and Simulation in Materials Science and Engineering 30 (2), 023002.

Mahalanobis, P. C., 1936. On the generalised distance in statistics. In: Proceedings of the National Institute of Sciences of India. Vol. 2.

Mandel, J., 1966. Contribution théorique à l'étude de l'écrouissage et des lois de l'écoulement plastique. In: Applied Mechanics: Proceedings of the Eleventh International Congress of Applied Mechanics Munich (Germany) 1964. Springer, Berlin, Heidelberg, Germany.

Marin, O., Gustavsson, K., Tornberg, A.-K., 2012. A highly accurate boundary treatment for confined Stokes flow. Computers & Fluids 66, 215–230.

Mehdikhani, M., Gorbatikh, L., Verpoest, I., Lomov, S. V., 2019. Voids in fiber-reinforced polymer composites: A review on their formation, characteristics, and effects on mechanical performance. Journal of Composite Materials 53 (12), 1579–1669.

Mehta, A., Schneider, M., 2022. A sequential addition and migration method for generating microstructures of short fibers with prescribed length distribution. Computational Mechanics 70 (4), 829–851.

Meyer, N., Gajek, S., Görthofer, J., Hrymak, A., Kärger, L., Henning, F., Schneider, M., Böhlke, T., 2023. A probabilistic virtual process chain to quantify process-induced uncertainties in Sheet Molding Compounds. Composites Part B: Engineering 249, 110380.

Mezhoud, S., Monchiet, V., Bornert, M., Grande, D., 2020. Computation of macroscopic permeability of doubly porous media with FFT based numerical homogenization method. European Journal of Mechanics-B/Fluids 83, 141–155.

Milton, G. W., 2002. The Theory of Composites. Cambridge University Press, Cambridge, United Kingdom.

Mobuchon, C., Carreau, P. J., Heuzey, M.-C., Sepehr, M., Ausias, G., 2005. Shear and extensional properties of short glass fiber reinforced polypropylene. Polymer Composites 26 (3), 247–264.

Montgomery-Smith, S., He, W., Jack, D. A., Smith, D. E., 2011. Exact tensor closures for the three-dimensional Jeffery's equation. Journal of Fluid Mechanics 680, 321–335.

Morro, A., Giorgi, C., 2023. Mathematical Modelling of Continuum Physics. Springer, Berlin, Heidelberg, Germany.

Mortazavian, S., Fatemi, A., 2015. Effects of fiber orientation and anisotropy on tensile strength and elastic modulus of short fiber reinforced polymer composites. Composites Part B: Engineering 72, 116–129.

Moulinec, H., Suquet, P., 1994. A fast numerical method for computing the linear and nonlinear mechanical properties of composites. Comptes Rendus de l'Académie des sciences. Série II. Mécanique, physique, chimie, astronomie , hal–03019226.

Moulinec, H., Suquet, P., 1998. A numerical method for computing the overall response of nonlinear composites with complex microstructure. Computer Methods in Applied Mechanics and Engineering 157 (1-2), 69–94.

Neumaier, A., 1998. Solving ill-conditioned and singular linear systems: A tutorial on regularization. SIAM Review 40 (3), 636–666.

Nguyen, V. D., Noels, L., 2022a. Interaction-based material network: A general framework for (porous) microstructured materials. Computer Methods in Applied Mechanics and Engineering 389, 114300.

Nguyen, V. D., Noels, L., 2022b. Micromechanics-based material networks revisited from the interaction viewpoint; robust and efficient implementation for multi-phase composites. European Journal of Mechanics-A/Solids 91, 104384.

Owen, A. B., 1998. Scrambling Sobol'and Niederreiter–Xing Points. Journal of Complexity 14 (4), 466–489.

Park, C., Lee, W., Yoo, Y., Kim, E., 2001. A study on fiber orientation in the compression molding of fiber reinforced polymer composite material. Journal of Materials Processing Technology 111 (1-3), 233–239.

Paszke, A., Gross, S., Massa, F., Lerer, A., Bradbury, J., Chanan, G., Killeen, T., Lin, Z., Gimelshein, N., Antiga, L., Desmaison, A., Kopf, A., Yang, E., DeVito, Z., Raison, M., Tejani, A., Chilamkurthy, S., Steiner, B., Fang, L., Bai, J., Chintala, S., 2019. PyTorch: An imperative style, high-performance deep learning library. In: Advances in Neural Information Processing Systems 32. Curran Associates, Inc., pp. 8024–8035.
URL http://papers.neurips.cc/paper/9015-pytorch-an-imperative-style-high-performance-deep-learning-library.pdf

Petrie, C. J., 1999. The rheology of fibre suspensions. Journal of Non-Newtonian Fluid Mechanics 87 (2-3), 369–402.

Phelps, J. H., Abd El-Rahman, A. I., Kunc, V., Tucker, C. L., 2013. A model for fiber length attrition in injection-molded long-fiber composites. Composites Part A: Applied Science and Manufacturing 51, 11–21.

Pipes, R. B., 1992. Anisotropic viscosities of an oriented fiber composite with a power-law matrix. Journal of Composite Materials 26 (10), 1536–1552.

Pipes, R. B., Coffin, D. W., Shuler, S. F., Šimáček, P., 1994. Non-Newtonian constitutive relationships for hyperconcentrated fiber suspensions. Journal of Composite Materials 28 (4), 343–351.

Pipes, R. B., Hearle, J., Beaussart, A., Sastry, A., Okine, R., 1991. A constitutive relation for the viscous flow of an oriented fiber assembly. Journal of Composite Materials 25 (9), 1204–1217.

Polyak, B. T., 1964. Some methods of speeding up the convergence of iteration methods. USSR Computational Mathematics and Mathematical Physics 4 (5), 1–17.

Poslinski, A., Ryan, M., Gupta, R., Seshadri, S., Frechette, F., 1988. Rheological behavior of filled polymeric systems I. Yield stress and shear-thinning effects. Journal of Rheology 32 (7), 703–735.

Qureshi, J., 2022. A review of fibre reinforced polymer structures. Fibers 10 (3), 27.

Rahnama, M., Koch, D. L., Shaqfeh, E. S., 1995. The effect of hydrodynamic interactions on the orientation distribution in a fiber suspension subject to simple shear flow. Physics of Fluids 7 (3), 487–506.

Ranganathan, S. I., Ostoja-Starzewski, M., 2008. Universal elastic anisotropy index. Physical Review Letters 101 (5), 055504.

Reich, S., 1983. A limit theorem for projections. Linear and Multilinear Algebra 13 (3), 281–290.

Renard, J., Marmonier, M., 1987. Etude de l'initiation de l'endommagement dans la matrice d'un matériau composite par une méthode d'homogénéisation. La Recherche aérospatiale (6), 43–51.

Ronneberger, O., Fischer, P., Brox, T., 2015. U-net: Convolutional networks for biomedical image segmentation. In: Medical image computing and computer-assisted intervention–MICCAI 2015: 18th international conference, Munich, Germany, October 5-9, 2015, proceedings, part III 18. Springer.

Ruder, S., 2016. An overview of gradient descent optimization algorithms. arXiv:1609.04747 .

Schelleis, C., Hrymak, A., Henning, F., 2023. Optimizing processing parameters for glass fiber reinforced polycarbonate LFT-D composites. Society for the Advancement of Material and Process Engineering Europe Conference .

Schneider, M., 2016. On the effective viscosity of a periodic suspension–analysis of primal and dual formulations for Newtonian and non-Newtonian solvents. Mathematical Methods in the Applied Sciences 39 (12), 3309–3327.

Schneider, M., 2017. The sequential addition and migration method to generate representative volume elements for the homogenization of short fiber reinforced plastics. Computational Mechanics 59 (2), 247–263.

Schneider, M., 2020a. A dynamical view of nonlinear conjugate gradient methods with applications to FFT-based computational micromechanics. Computational Mechanics 66 (1), 239–257.

Schneider, M., 2020b. Lippmann-Schwinger solvers for the computational homogenization of materials with pores. International Journal for Numerical Methods in Engineering 121 (22), 5017–5041.

Schneider, M., 2021. A review of nonlinear FFT-based computational homogenization methods. Acta Mechanica 232 (6), 2051–2100.

Schneider, M., Wicht, D., 2023. Superconvergence of the effective Cauchy stress in computational homogenization of inelastic materials. International Journal for Numerical Methods in Engineering 124 (4), 959–978.

Segurado, J., Lebensohn, R. A., LLorca, J., 2018. Computational homogenization of polycrystals. Advances in Applied Mechanics 51, 1–114.

Sepehr, M., Carreau, P. J., Moan, M., Ausias, G., 2004. Rheological properties of short fiber model suspensions. Journal of Rheology 48 (5), 1023–1048.

Shaqfeh, E. S., Fredrickson, G. H., 1990. The hydrodynamic stress in a suspension of rods. Physics of Fluids A: Fluid Dynamics 2 (1), 7–24.

Shin, D., Alberdi, R., Lebensohn, R. A., Dingreville, R., 2024. A deep material network approach for predicting the thermomechanical response of composites. Composites Part B: Engineering 272, 111177.

Shuler, S. F., Binding, D. M., Byron Pipes, R., 1994. Rheological behavior of two-and three-phase fiber suspensions. Polymer Composites 15 (6), 427–435.

Sika, R., Rogalewicz, M., Popielarski, P., Czarnecka-Komorowska, D., Przestacki, D., Gawdzińska, K., Szymański, P., 2020. Decision support system in the field of defects assessment in the metal matrix composites castings. Materials 13 (16), 3552.

Šilhavý, M., 1997. The Mechanics and Thermodynamics of Continuous Media. Springer, Berlin, Heidelberg, Germany.

Smith, L. N., Topin, N., 2019. Super-convergence: Very fast training of neural networks using large learning rates. In: Artificial Intelligence and Machine Learning for Multi-Domain Operations Applications. Vol. 11006. SPIE.

Sobol, I. M., 1967. On the distribution of points in a cube and the approximate evaluation of integrals. USSR Computational Mathematics and Mathematical Physics 7 (4), 86–112.

Sorić, J., Wriggers, P., Allix, O., 2018. Multiscale Modeling of Heterogeneous Structures. Springer, Berlin, Heidelberg, Germany.

Souloumiac, B., Vincent, M., 1998. Steady shear viscosity of short fibre suspensions in thermoplastics. Rheologica Acta 37 (3), 289–298.

Spahn, J., Andrä, H., Kabel, M., Müller, R., 2014. A multiscale approach for modeling progressive damage of composite materials using fast Fourier transforms. Computer Methods in Applied Mechanics and Engineering 268, 871–883.

Spurk, J., Aksel, N., 2007. Fluid Mechanics. Springer, Berlin, Heidelberg, Germany.

Steinmann, P., 2015. Geometrical Foundations of Continuum Mechanics. Vol. 2. Springer, Berlin, Heidelberg, Germany.

Sterr, B., Gajek, S., Hrymak, A., Schneider, M., Böhlke, T., 2024a. Deep material networks for fiber suspensions with infinite material contrast. arXiv:2406.11662 .

Sterr, B., Hrymak, A., Schneider, M., Böhlke, T., 2024b. Machine learning assisted discovery of effective viscous material laws for shear-thinning fiber suspensions. Computational Mechanics , 1–19.

Sterr, B., Wicht, D., Hrymak, A., Schneider, M., Böhlke, T., 2023. Homogenizing the viscosity of shear-thinning fiber suspensions with an FFT-based computational method. Journal of Non-Newtonian Fluid Mechanics 321, 105101.

Style, R. W., Wettlaufer, J. S., Dufresne, E. R., 2015. Surface tension and the mechanics of liquid inclusions in compliant solids. Soft Matter 11 (4), 672–679.

Sun, S., Cao, Z., Zhu, H., Zhao, J., 2019. A survey of optimization methods from a machine learning perspective. IEEE transactions on cybernetics 50 (8), 3668–3681.

Sundararajakumar, R., Koch, D. L., 1997. Structure and properties of sheared fiber suspensions with mechanical contacts. Journal of Non-Newtonian Fluid Mechanics 73 (3), 205–239.

Suquet, P., 1985. Local and global aspects in the mathematical theory of plasticity. Plasticity Today , 279–309.

Suquet, P., 1987. Elements of homogenization for inelastic solid mechanics. In: Homogenization techniques for composite media Ch. 4. Springer, Berlin, Heidelberg, Germany.

Sutherland, W., 1905. A dynamical theory of diffusion for non-electrolytes and the molecular mass of albumin. The London, Edinburgh, and Dublin Philosophical Magazine and Journal of Science 9 (54), 781–785.

Švec, O., Skoček, J., Stang, H., Geiker, M. R., Roussel, N., 2012. Free surface flow of a suspension of rigid particles in a non-Newtonian fluid: A lattice Boltzmann approach. Journal of Non-Newtonian Fluid Mechanics 179, 32–42.

Swolfs, Y., 2017. Perspective for fibre-hybrid composites in wind energy applications. Materials 10 (11), 1281.

Tieleman, T., Hinton, G., et al., 2012. Lecture 6.5-rmsprop: Divide the gradient by a running average of its recent magnitude. COURSERA: Neural networks for machine learning 4 (2), 26–31.

Traxl, R., Pichler, C., Lackner, R., 2020. Micromechanics-based assessment of the effective viscosity of suspensions of generalized-Newtonian fluids embedding noncolloidal angular/spheroidal pores and particles. Journal of Rheology 64 (4), 899–913.

Tseng, H.-C., 2021. A constitutive equation for fiber suspensions in viscoelastic media. Physics of Fluids 33 (7), 071702.

Tseng, H.-C., Chang, R.-Y., Hsu, C.-H., 2018. Predictions of fiber concentration in injection molding simulation of fiber-reinforced composites. Journal of Thermoplastic Composite Materials 31 (11), 1529–1544.

Tu, F., Tong, J., Wang, M., Chen, Z., Qi, S., 2022. An FFT-based Galerkin method for the effective permeability of porous material. International Journal for Numerical Methods in Engineering 123 (20), 4893–4915.

Tucker III, C. L., 1991. Flow regimes for fiber suspensions in narrow gaps. Journal of Non-Newtonian Fluid Mechanics 39 (3), 239–268.

Valero, J. R. L., 2020. Plastics Injection Molding: Scientific Molding, Recommendations, and Best Practices. Carl Hanser Verlag GmbH Co KG, Munich, Germany.

Vincent, M., Giroud, T., Clarke, A., Eberhardt, C., 2005. Description and modeling of fiber orientation in injection molding of fiber reinforced thermoplastics. Polymer 46 (17), 6719–6725.

Wang, Y., Henann, D. L., 2016. Finite-element modeling of soft solids with liquid inclusions. Extreme Mechanics Letters 9, 147–157.

Wazeer, A., Das, A., Abeykoon, C., Sinha, A., Karmakar, A., 2023. Composites for electric vehicles and automotive sector: A review. Green Energy and Intelligent Transportation 2 (1), 100043.

Wicht, D., 2022. Efficient Fast Fourier Transform-based Solvers for Computing the Thermomechanical Behavior of Applied Materials. Doctoral thesis, KIT Scientific Publishing, Karlsruhe, Germany.

Wicht, D., Schneider, M., Böhlke, T., 2020a. An efficient solution scheme for small-strain crystal-elasto-viscoplasticity in a dual framework. Computer Methods in Applied Mechanics and Engineering 358, 112611.

Wicht, D., Schneider, M., Böhlke, T., 2020b. An efficient solution scheme for small-strain crystal-elasto-viscoplasticity in a dual framework. Computer Methods in Applied Mechanics and Engineering 358, 112611.

Williams, M. L., Landel, R. F., Ferry, J. D., 1955. The temperature dependence of relaxation mechanisms in amorphous polymers and other glass-forming liquids. Journal of the American Chemical Society 77 (14), 3701–3707.

Williams, S., Philipse, A., 2003. Random packings of spheres and spherocylinders simulated by mechanical contraction. Physical Review E 67 (5), 051301.

Willis, J. R., 1977. Bounds and self-consistent estimates for the overall properties of anisotropic composites. Journal of the Mechanics and Physics of Solids 25 (3), 185–202.

Willot, F., 2015. Fourier-based schemes for computing the mechanical response of composites with accurate local fields. Comptes Rendus Mécanique 343 (3), 232–245.

Wittemann, F., Maertens, R., Kärger, L., Henning, F., 2019. Injection molding simulation of short fiber reinforced thermosets with anisotropic and non-Newtonian flow behavior. Composites Part A: Applied Science and Manufacturing 124, 105476.

Wu, L., Adam, L., Noels, L., 2021. Micro-mechanics and data-driven based reduced order models for multi-scale analyses of woven composites. Composite Structures 270, 114058.

Zeiler, M. D., 2012. Adadelta: an adaptive learning rate method. arXiv:1212.5701 .

Zener, C. M., Siegel, S., 1949. Elasticity and anelasticity of metals. The Journal of Physical Chemistry 53 (9), 1468–1468.

Schriftenreihe Kontinuumsmechanik im Maschinenbau
Karlsruher Institut für Technologie (KIT)
(ISSN 2192-693X)

Band 1 Felix Fritzen
Microstructural modeling and computational homogenization of the physically linear and nonlinear constitutive behavior of micro-heterogeneous materials.
ISBN 978-3-86644-699-1

Band 2 Rumena Tsotsova
Texturbasierte Modellierung anisotroper Fließpotentiale.
ISBN 978-3-86644-764-6

Band 3 Johannes Wippler
Micromechanical finite element simulations of crack propagation in silicon nitride.
ISBN 978-3-86644-818-6

Band 4 Katja Jöchen
Homogenization of the linear and non-linear mechanical behavior of polycrystals.
ISBN 978-3-86644-971-8

Band 5 Stephan Wulfinghoff
Numerically Efficient Gradient Crystal Plasticity with a Grain Boundary Yield Criterion and Dislocation-based Work-Hardening.
ISBN 978-3-7315-0245-6

Band 6 Viktor Müller
Micromechanical modeling of short-fiber reinforced composites.
ISBN 978-3-7315-0454-2

Die Bände sind unter www.ksp.kit.edu als PDF frei verfügbar oder als Druckausgabe bestellbar.

Band 7 Florian Rieger
Work-hardening of dual-phase steel.
ISBN 978-3-7315-0513-6

Band 8 Vedran Glavas
Micromechanical Modeling and Simulation of Forming Processes.
ISBN 978-3-7315-0602-7

Band 9 Eric Bayerschen
Single-crystal gradient plasticity with an accumulated plastic slip: Theory and applications.
ISBN 978-3-7315-0606-5

Band 10 Bartholomäus Brylka
Charakterisierung und Modellierung der Steifigkeit von langfaserverstärktem Polypropylen.
ISBN 978-3-7315-0680-5

Band 11 Rudolf Neumann
Two-Scale Thermomechanical Simulation of Hot Stamping.
ISBN 978-3-7315-0714-7

Band 12 Mauricio Lobos Fernández
Homogenization and materials design of mechanical properties of textured materials based on zeroth-, first- and second-order bounds of linear behavior.
ISBN 978-3-7315-0770-3

Band 13 Malte Schemmann
Biaxial Characterization and Mean-field Based Damage Modeling of Sheet Molding Compound Composites.
ISBN 978-3-7315-0818-2

Band 14 Jürgen Albiez
Finite element simulation of dislocation based plasticity and diffusion in multiphase materials at high temperature.
ISBN 978-3-7315-0918-9

Band 15 Maria Loredana Kehrer
Thermomechanical Mean-Field Modeling and Experimental Characterization of Long Fiber-Reinforced Sheet Molding Compound Composites.
ISBN 978-3-7315-0924-0

Band 16 Peter Hölz
A dynamic and statistical analysis of the temperature- and fatigue behavior of a race power unit – The effect of different thermodynamic states.
ISBN 978-3-7315-0988-2

Band 17 Andreas Prahs
A Gradient Crystal Plasticity Theory Based on an Extended Energy Balance.
ISBN 978-3-7315-1025-3

Band 18 Johannes Ruck
Modeling martensitic phase transformation in dual phase steels based on a sharp interface theory.
ISBN 978-3-7315-1072-7

Band 19 Hannes Erdle
Modeling of Dislocation - Grain Boundary Interactions in Gradient Crystal Plasticity Theories.
ISBN 978-3-7315-1196-0

Band 20 Johannes Görthofer
Microstructure generation and micromechanical modeling of sheet molding compound composites.
ISBN 978-3-7315-1205-9

Band 21 Daniel Wicht
Efficient fast Fourier transform-based solvers for computing the thermomechanical behavior of applied materials.
ISBN 978-3-7315-1220-2

Band 22 Juliane Lang
Thermomechanical Modeling and Experimental Characterization of Sheet Molding Compound Composites.
ISBN 978-3-7315-1232-5

Die Bände sind unter www.ksp.kit.edu als PDF frei verfügbar oder als Druckausgabe bestellbar.

Band 23 Julian Karl Bauer
Fiber Orientation Tensors and Mean Field Homogenization: Application to Sheet Molding Compound.
ISBN 978-3-7315-1262-2

Band 24 Sebastian Gajek
Deep material networks for efficient scale-bridging in thermomechanical simulations of solids.
ISBN 978-3-7315-1278-3

Band 25 Jannick Kuhn
Microstructure modeling and crystal plasticity parameter identification for predicting the cyclic mechanical behavior of polycrystalline metals.
ISBN 978-3-7315-1272-1

Band 26 Felix Ernesti
A computational multi-scale approach for brittle materials.
ISBN 978-3-7315-1285-1

Band 27 Patrick Arthur Hessman
On multi-scale modeling of fatigue in short glass fiber reinforced thermoplastics.
ISBN 978-3-7315-1398-8

Band 28 Benedikt Sterr
Machine learning aided multiscale mechanics of fiber suspensions.
ISBN 978-3-7315-11421-3

We combine computational homogenization techniques with machine learning to study and model the anisotropic viscous behavior of fiber suspensions with non-Newtonian solvents. To do so, we extend an existing Fast Fourier Transform (FFT) based method for the homogenization of suspensions with Newtonian solvents to suspensions with non-Newtonian solvents. In particular, we solve a dual formulation of the variational cell problem using FFTs and a Newton-CG approach. We combine the extended FFT-based method with machine learning to identify models for the effective viscosity of fiber suspensions with a shear-thinning PA6 matrix material. For a variety of flow scenarios and fiber orientations, we compute the suspension behavior, and present suitable analytical models for the effective viscosity. We then identify the model parameters using a supervised machine learning strategy.
Furthermore, we introduce a novel Deep Material Network (DMN) architecture for the treatment of fiber suspensions with non-Newtonian solvents. We utilize two-phase layered emulsions as DMN building blocks, and repeatedly layer them in a specific manner to treat infinite material contrast. By doing so, we extend the direct DMN framework to the Flexible DMN (FDMN) architecture. We employ FDMNs to predict the effective viscous response of fiber suspensions with a shear-thinning PA6 matrix material. Finally, we compare the analytical models with the FDMNs.

ISSN 2192-693X
ISBN 978-3-7315-1421-3

Gedruckt auf FSC-zertifiziertem Papier